PhD THESIS

COHERENCE IN MOLECULAR PHOTOIONIZATION

by **DAVID AYUSO MOLINERO**

supervisors
FERNANDO MARTÍN &
ALICIA PALACIOS

UNIVERSIDAD AUTÓNOMA DE MADRID
2015

Contents

Acknowledgements

I would like to express my gratitude to the people that have made this work possible:

- To Alicia, for her constant help and support
- To Fernando, for his support and for giving me the opportunity to join this amazing group
- To Piero, for his clear explanations and his constant help
- To my office mates, for making me enjoy every day of work
- To the people in the department
- And to my family and friends, and to Steven, for supporting me

Abstract

We present a theoretical study of light-induced phenomena in gas-phase molecules. We explore the physical phenomena arising in two distinct contexts: using synchrotron radiation and ultrashort laser pulses. This theoretical work has been done in close collaboration with Piero Decleva, from Università di Trieste.

We first present a study of inner-shell photoionization of diatomic (CO) and small polyatomic (CF_4, BF_3) molecules at high photoelectron energies performed in collaboration with the experimental the groups of Edwin Kukk (Turku University), Catalin Miron (Soleil Synchrotron), Kiyosi Ueda (SPring8 Synchrotron) and Thomas Darrah Thomas (Oregon State University). The combination of state-of-the-art Density Functional Theory (DFT)-like calculations capable to describe photoionization accounting for the nuclear degrees of freedom together with high-resolution third-generation synchrotron facilities has enabled the investigation of non-Franck-Condon effects observable in vibrationally resolved photoionization measurements. We demonstrate that the nuclear response to intramolecular electron diffraction is observable and can be used to obtain structural information. As a proof-of-principle, by using the DFT calculations as an analysis tool to fit the experimental data, we have accurately determined the equilibrium distance of the CO molecule and the bond contraction that takes place upon C 1s ionization. This is a surplus of photoelectron spectroscopy with respect to more conventional spectroscopic techniques, which usually can only provide structural information of neutral molecular species. Furthermore, we have explored the different phenomenon arising when an electron is emitted from a delocalized orbital: multicenter emission. The results on molecular fluorine coming from our numerical simulations are in good qualitative agreement with those provided by the simple formula proposed by Cohen and Fano in the sixties.

We have employed the same DFT-based methodology together with time-dependent first-order perturbation theory and a reduced density matrix formalism to report the first demonstration of purely electron dynamics in a biological molecule: the amino acid phenylalanine, in collaboration with the experimental groups of Mauro Nisoli (Politecnico di Milano), Luca Poletto (IFN-CNR, Padova) and Jason Greenwood (Queen's University, Belfast). The use of attosecond pulses in combination with novel detection techniques has enabled the capture of purely electron motion at its intrinsic time scale. Because of their wide energy bandwidth, attosecond pulses are ideal sources to generate coherent

superpositions of states, triggering an ultrafast electronic response that can be later tracked with attosecond resolution. Our theoretical study enabled to interpret the experimental findings in terms of charge migration, thus confirming the first observation of purely electron dynamics in a biomolecule. The work presented here has been extended to treat the amino acids glycine and tryptophan, which has allowed the investigation of radical substitution effects in the charge migration mechanism.

Resumen

Presentamos un estudio teórico de procesos inducidos por luz en moléculas en fase gaseosa, donde investigamos procesos físicos que surgen en dos contextos diferentes: utilizando radiación sincrotrón y púlsos láser ultracortos. Este trabajo teórico ha sido realizado en estrecha colaboración con Piero Decleva, de la Università di Trieste.

En primer lugar, presentamos un estudio de fotoionización de capa interna en moléculas diatómicas (CO) y poliatómicas (CF_4, BF_3) a altas energías de fotoelectrón, en colaboración con los grupos experimentales de Edwin Kukk (Turku University), Catalin Miron (Soleil Synchrotron), Kiyosi Ueda (SPring8 Synchrotron) y Thomas Darrah Thomas (Oregon State University). La combinación de cálculos avanzados basados en la Teoría del Funcional de la Densidad (DFT, del inglés "Density Functional Theory") capaces de describir procesos de fotoionización teniendo en cuenta los grados de libertad nucleares, junto con el uso de instalaciones sincrotrón de tercera generación de alta precisión, ha permitido la investigación de desviaciones de Franck-Condon, observables en espectros de fotoionización resueltos vibracionalmente. Demostramos que la respuesta nuclear a la difracción electrónica es observable y puede ser utilizada para obtener información estructural. Como prueba de concepto, utilizando cálculos DFT como herramienta de análisis para ajustar los datos experimentales, hemos determinado con precisión la distancia de equilibrio de la molécula de CO y la contracción de enlace que tiene lugar tras arrancar un electrón del orbital 1s del átomo de carbono. Esto representa una ventaja de la espectroscopía fotoelectrónica con respecto a técnicas espectroscópicas más convencionales, que generalmente pueden proporcionar información estructural de la especie neutra. Además, hemos analizado un fenómeno distinto que tiene lugar cuando se emite un electrón desde un orbital deslocalizado: emisión multicéntrica. Los resultados obtenidos en la molécula de flúor mediante simulaciones numéricas están de acuerdo, de forma cualitativa, con los proporcionados por la simple fórmula propuesta por Cohen y Fano en los aos sesenta.

Hemos empleado la misma metodología basada en DFT junto con teoría de perturbaciones a primer orden y un formalismo de matriz de densidad reducida para reportar la primera demostración experimental de dinámica electrónica en una molécula biológica: el amino ácido fenilalanina, en colaboración con los grupos experimentales de Mauro Nisoli (Politecnico di Milano), Luca Poletto (IFN-CNR, Padova) y Jason Greenwood (Queen's University, Belfast).

El uso de pulsos de atosegundos, en combinación con novedosas técnicas de detección, ha permitido la captura de dinámica puramente electrónica en su escala de tiempo natural. Debido a sus anchos espectros energéticos, los pulsos de atosegundos son ideales para generar superposiciones coherentes de estados, induciendo una respuesta electrónica ultrarrápida que puede ser visualizada con resolución de atosegundos. Nuestro estudio teórico ha permitido interpretar los hallazgos experimentales en términos de migración de carga, confirmando la primera observación de dinámica puramente electrónica en una biomolécula. El trabajo presentado aquí ha sido se ha extendido al estudio de los amino ácidos glicina y triptófano, lo cual ha permitido la investigación de procesos debidos a la sustitución del radical en el mecanismo de la migración de carga.

Introduction

Chemical reactions occur as a result of bond breaking and formation, a dynamical process that is initiated by changes in the electronic structure of a molecule and followed by the subsequent nuclear rearrangement. The study of the dynamics associated to the nuclear motion belongs to the realm of femtochemistry, a well-established field that for more than twenty years has been able to capture and even control the nuclear motion in chemical reactions and intramolecular processes [1, 2]. The field obtained an important recognition in 1999, when Ahmed Zewail was awarded the Nobel prize in chemistry "for his studies of the transition states of chemical reactions using femtosecond spectroscopy" [3]. One of the most common techniques to investigate the dynamics of a chemical reaction is the well-known pump-probe spectroscopy. In this approach, a short pulse of light (pump) is used to induce a process in a molecular target and, after some time, the dynamical response of the system is monitored with a second pulse (probe). By performing measurements with different time delays between the two pulses, it is possible to take "snapshots" of a chemical reaction. Of course, the durations of the light pulses employed need to be (at least) of the same order of magnitude (or shorter) than the dynamics to observe. This is the reason why purely electron motion, occurring in the attosecond time domain, has remained hidden from direct experimental observation until very recently, when pulses with durations as short as a few tens of attoseconds became available.

Attosecond science

The first attosecond pulse [4] and the first train of attosecond pulses [5] were generated in 2001 using high-harmonic generation (HHG). HHG is a non-linear process occurring when an atomic or molecular gas is irradiated with an intense femtosecond laser, usually a Ti:sapphire laser, with a central wavelength of 800 nm. The target will then emit XUV light with frequencies that are high odd multiples of the driving field [6, 7]. An interpretation of this phenomenon was given in 1993 [8] by Paul Corkum by means of a three-step model: due to the distortion of the Coulomb potential by the strong IR field, the electron is ionized by tunneling through the electric barrier (see fig. 1). Then (second step), the electron is accelerated by the laser field and driven back towards the parent ion. In the last step, the recombination, all the energy that the electron has absorbed from the field is released as an energetic XUV or X-ray photon [8].

Since the first step (tunnel ionization) is a non-linear process that requires the absorption of several photons, it is more likely to occur at the maxima of the laser field, where the tunneling picture is valid. Thus, electrons are released in ultrashort intervals, leading to the formation attosecond laser pulses [9].

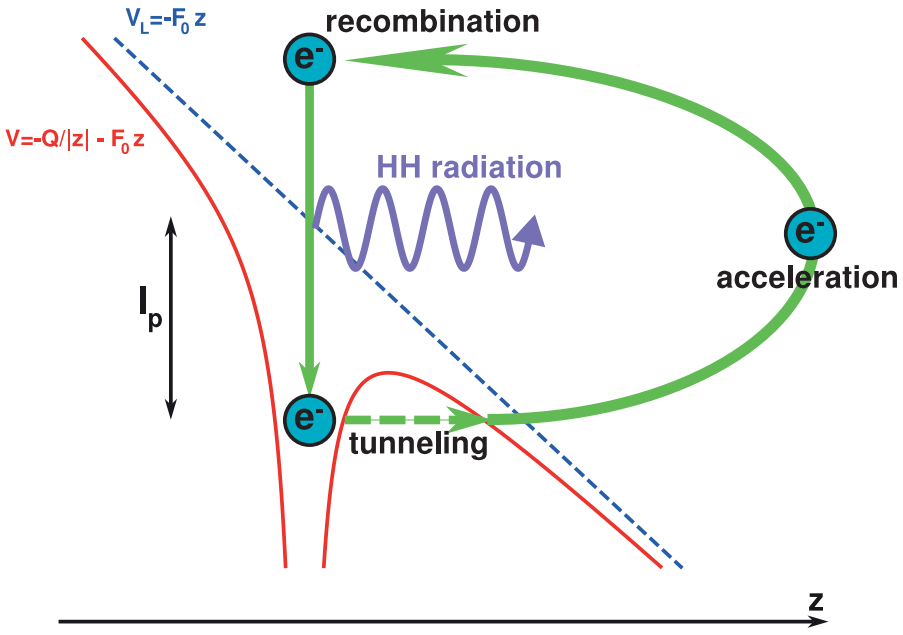

Figure 1: Schematic representation of the three-step model [8] for HHG: (1) tunnel ionization, (2) acceleration by the driving field and (3) recombination with the parent ion. Image courtesy of Maria Richter.

According to the three-step model, an attosecond pulse can be generated twice every cycle of the driving femtosecond pulse. Therefore, HHG will tend to form attosecond pulse trains (APTs) rather than single attosecond pulses (SAPs). A lot of work has been directed towards the generation of SAPs [10]. The first SAP was produced in 2001 by the group of Ferenc Krausz by using the selection of cutoff harmonics generated with a 7 fs IR pulse. Because of the short duration of the IR field, the highest harmonics were produced only during one half-cycle, thus generating a SAP. SAPs can be characterized using the of principle of the attosecond streak camera [11]. According to this principle, the momentum of the photoelectrons emitted by the SAP are modified in a extent that depends on the relative time delay between the two pulses. The first fully-characterized SAP was generated in 2006 in the group of Mauro Nisoli [12], with a duration of 130 as and a central frequency of 35 eV. Two years later, the 100 as barrier was broken, reaching down to 80 as with a 80 eV pulse [13]. To date, the shortest XUV pulse ever generated is 67 as-long and has a central energy of 90 eV [14].

These impressive achievements have enabled the real-time observation and control of electron motion in atoms, molecules and condensed phases [15, 10, ?, 16]. The observation of the femtosecond Auger decay in krypton was the first application of isolated attosecond pulses in 2002 [17]. This demonstration was then followed by other important experimental results in the field of ultrafast atomic physics, such as the real-time observation of electron tunneling [18] and the measurement of temporal delays of the order of a few tens of attoseconds in the photoemission of electrons from different atomic orbitals of neon [19] and argon [20]. The unprecedented time resolution offered by attosecond pulses has also allowed quantum mechanical electron motion and its degree of coherence to be measured in atoms by using attosecond transient absorption spectroscopy [21]. Attosecond techniques have been applied in the field of ultrafast solid-state physics, with the measurement of delays in electron photoemission from crystalline solids [22] and the investigation of the ultrafast field-induced insulator-to-conductor state transition in a dielectric [23].

In the past few years, attosecond pulses have also been used to measure ultrafast electronic processes in simple molecules [24]. Although the study of complex molecules is challenging, a formative measurement of the amino acid phenylalanine has shown that ionization by a short APT leads to dynamics on a temporal scale of a few tens of femtoseconds. This has been interpreted as the possible signature of ultrafast electron transfer inside the molecule [25]. The application of attosecond techniques to molecules offers the possibility of investigating primary relaxation processes, which involve electronic and nuclear degrees of freedom and their coupling. In the case of large molecules (e.g., biologically relevant molecules), prompt ionization by attosecond pulses may produce ultrafast charge migration along the molecular skeleton, which can precede nuclear rearrangement. This behavior has been predicted in theoretical calculations by various authors [26, 27, 28, 29, 30], whose work was stimulated by pioneering experiments performed by Weinkauf, Schlag, and co-workers on fragmentation of peptide chains [31, 32]. This electron dynamics, evolving on an attosecond or few-femtosecond temporal scale, can determine the subsequent relaxation pathways of the molecule [24]. The process is induced by sudden generation of an electronic wave packet, which moves across the molecular chain and induces a site selective reactivity, which is related to charge localization in a particular site of the molecule [26]. Although picosecond and femtosecond pulses are suitable for the investigation of nuclear dynamics, the study of electronic dynamics with these pulses has been made possible by slowing down the dynamics through the use of Rydberg electron wave packets [33]. However, in order to study the electron wave-packet dynamics in the outer-valence molecular orbitals relevant to most chemical and biological systems, attosecond pulses are required.

Despite the impressive progress made in the last decades, attosecond pulses generated via HHG have two main limitations: their relatively low intensities, which can make some attosecond pump-probe experiments quite challenging, and the limited range of photon energies in which they can be produced. These limitations have been overcome in the recently operating XUV/X-ray

free-electron laser (FEL) facilities, which can produce bright attosecond pulses using synchrotron light.

Synchrotron light

Synchrotron radiation is emitted when charged particles moving at velocities close to the speed of light are forced to change direction by a magnetic field, as dictated by the fundamental laws of electrodynamics [34]. The first observation of artificial synchrotron light occurred at the General Electric Research Laboratory in New York in 1947 [35], opening a new era of accelerator-based light sources. Ever since, synchrotron light sources have progress dramatically, rapidly evolving through up to four different generations [36].

Synchrotron radiation spans a wide energy range, from infrared light up to the highest-energy X-rays. It is characterized by high brightness, being orders of magnitude brighter than that produced in conventional light sources. Synchrotron light is also highly polarized (linearly, circularly or elliptically), tunable, collimated (consisting of almost parallel rays) and concentrated over a small area. These properties make synchrotron radiation one of the most important and universal research tools, with a steadily increasing number of applications.

The so-called first-generation light sources were high-energy physics facilities were synchrotron radiation was generated as a byproduct. The interest for the use of synchrotron light increased over the years, motivating a series of pioneering advances. The most important one was the development of storage rings [37], the basis for all of today's synchrotrons. A storage ring is a type of circular accelerator in which the beam of particles can circulate at a fixed energy during long periods of time (hours), providing more stable beam conditions and reducing the radiation hazard. In 1975, the Synchrotron Radiation Source (SRS) at the Daresbury Laboratory in the UK, the first synchrotron exclusively designed to the production of light, began to be constructed [38, 39]. It became operational in 1981 [40], the same year than the BESSY synchrotron [41], in Berlin, giving birth to the second-generation light sources. Over the years, some facilities originally developed to high-energy physics, gradually evolved towards a second-generation status by means of upgrades and by dedicating more operating time to light production. The HASYLAB (Hamburger Synchrotronstrahlungslabor) at DESY and the Stanford Synchrotron Radiation Laboratory at the SLAC National Accelerator Laboratory and are some examples. Spectroscopists and crystallographers could benefit from the brightness of the X-ray beams produced these facilities, which enabled to perform high-resolution experiments, and new experimental techniques were born, such as the well-known extended x-ray absorption fine-structure spectroscopy (EXAFS) [42, 43] for the measurement of local atomic structure.

The development of special magnet structures, the so-called insertion devices [44], gave rise to the third-generation light sources. Insertion devices are arrays of magnets with alternating polarity that, placed into the straight sections of the storage ring, generate very bright beams and allow to shift the light spectrum

towards higher photon energies. These devices were quickly incorporated into existing the synchrotron facilities. Third-generation facilities, designed with insertion devices in place from the beginning, saw the light in the 90s. The first of them was the European Synchrotron Radiation Facility (ESRF), located in Grenoble, France, which started operating in 1994 [45, 46].

To date there are more than 50 dedicated light sources in the world, serving many areas of science ranging from chemistry, biology, physics, material science, medicine to industrial applications. The BESSY II in Berlin, the ELETTRA in Trieste, the National Synchrotron Light Source in the USA, the Spring-8 in Japan or SOLEIL in France are just a few examples. All of them present similar configurations, with a storage ring having many ports connected to the beamlines, small stations where the experiments are carried out. The different beamlines, however, can be more different depending on the kinds of experiments they are used for.

Free-electron lasers (FELs), the fourth-generation light sources, were born at the beginning of this century, opening a new era of time-resolved experiments. Instead of using storage rings, FELs accelerate beams of electrons in long (several kilometers) linear accelerators, generating ultrashort and ultrabright coherent light pulses. The underlying principle behind FELs is the self-amplified spontaneous emission (SASE). As in the third-generation light sources, FELs make use of insertion devices to generate synchrotron light. The synchrotron radiation generated inside of them interacts with the oscillating electrons, making them drift into microbunches, which are separated by a distance equal to one radiation wavelength. Through this interaction, the electrons start to emit coherent light. The emitted radiation can reinforce itself, leading to high beam intensities and laser-like properties.

The fist FEL to become operational was the Tesla Test Facility (TTF) at DESY, in Hamburg, in 2005, operating in the XUV range, allowing pioneering experiments on Coulomb explosion of rare gas clusters [47]. FLASH succeeded TTF in 2005, becoming the first soft X-ray FEL [48], where the first experiments on coherent diffractive imaging were perform, allowing the imaging of structures with sub-100 nm resolution [49, 50, 51] by using the of the so-called diffraction-before-destruction [52] approach. In 2009, the Linac Coherent Light Source (LCLS) in Stanford became the first hard X-ray FEL, leading to major improvements the resolution that could be achieved in coherent diffractive imaging experiments. The use of femtosecond pulses of 1.8 keV photons produced at LCLS allowed to retrieve the structure of nanocrystals with a spatial resolution o 8 Angstrom [53]. This number was soon improved by the use 9.4 keV hard X-ray photons, leading to a spatial resolution of only 2.1 Angstrom [54]. The FERMI FEL, at the Elettra Sincrotrone in Trieste, came into operation in 2010 [55]. The next year, the SACLA hard X-ray FEL, embedded in the Spring-8 accelerator and synchrotron complex in Japan became operational [56]. In addition, several hard X-ray FELs are planned all over the world, including the the SwissFEL and the European XFEL in Hamburg, both currently under construction and expected to start operating in 2016 and 2017, respectively.

Theoretical methods

Advances in synchrotron- and HHG-based light sources have opened the door for structural determination in single isolated molecules, as well as for imaging and even controlling electron and nuclear dynamics, with exciting applications in physics, chemistry and biology. In this context, theoretical calculations have become crucial to guide and to understand these new generation of experiments. The development of high-resolution third-generation synchrotron light sources, capable of producing ultra-bright radiation, has enabled the application of traditional photoelectron X-ray diffraction techniques to small molecules in the gas phase. Theory has allowed to understand the diffraction patterns arising in the photoelectron spectra by combining state-of-the-art calculations with the use of simple models, that can help to understand the most relevant features. Moreover, theoretical work has guided and motivated a large number of attosecond experiments, such as the recent observation of ultrafast charge migration in a biomolecule [57]. The first theoretical prediction of charge migration in complex systems came from L. S. Cederbaum and J. Zobeley more than 15 years ago [27], demonstrating that electron correlation can drive purely electron dynamics in the sub-femtosecond time scale, faster than the onset of the nuclear motion. Charge migration has become a hot topic, attracting the interest of a number of researchers and giving rise to exciting theoretical predictions in molecules of biological interest [58, 59, 57, 60] as large as chains of amino acids [26]. In all these works, the initial wave packet is generated by removing an electron from a given molecular orbital, generating a hole in the electronic structure. Since the ionized state is not a stationary state of the ionic Hamiltonian but a combination of stationary states, the hole moves though the molecular skeleton, with a velocity that is dictated by the energy spacing between the interfering states. These theoretical findings motivated the experimental observations in [57] as well as the design of nobel experiments using FELs [61]. More recently, theoretical approaches accounting for the interaction with a realistic attosecond pulse have been developed [62, 63, 64]. The evaluation of electronic wave packets in the continuum becomes arduous, especially in the case of large molecules. The role of the nuclear dynamics in charge migration has been recently analyzed [65, 66, 67] using semi-classical approaches. A full quantum description of the coupled nuclear and electron dynamics is challenging, even for the case small molecules. A few works on photoionization of diatomic molecules have considered both electronic and nuclear degrees of freedom, but neglecting the dependence of the electronic structure on the internuclear distance [68, 69]. In this context, the multi-configurational time-dependent Hartree-Fock (MCTDHF) method [70, 71, 72, 73, 74, 75, 76, 77] has been proved to be a powerful tool. DFT-based methods can also very useful because of their good compromise between accuracy and computational effort. The static-exchange DFT method and a more elaborate time-dependent version have been extended to include the nuclear motion at the Born-Oppenheimer level in diatomic molecules [78, 79, 80, 81, 82] or for the symmetric stretching mode in molecules with a small number of atoms [83, 84, 85, 86, 87, 88], finding very good agreement

with recent experimental results obtained with synchrotron radiation. The inclusion of more vibrational degrees of freedom while using a reliable description of electron correlation remains a challenge.

Outline

The aim of this work is to investigate light-induced phenomena in simple isolated systems, with especial emphasis in the theoretical description of processes that can be traced and manipulated using ultrafast laser pulses. In particular, we have focused on the investigation of (1) photoionization of small molecules using methods that account for both nuclear and electronic degrees of freedom, and (2) ultrafast electron dynamics in larger molecules initiated by attosecond XUV pulses. All the work presented in this PhD thesis has been done in collaboration with Piero Decleva, from Università di Trieste.

The theoretical methods employed in this work are described in chapters 1−3. Chapter 1 includes general concepts on treat light-matter interaction. How to apply them these concepts to the special case of molecules interacting with synchrotron radiation and attosecond pulses is presented in chapters 2 and 3. In this work we have employed the static-exchange DFT method, developed by Mauro Stener, Piero Decleva and collaborators, to evaluate bound and continuum electronic stationary states. The nuclear motion has been accounted for at the Born-Oppenheimer in the case of diatomic and small polyatomic molecules. This has allowed for the computation of vibrational excitations upon ionization and the investigation of non-Franck-Condon effects.

We have investigated the interferences arising in the photoionization of small molecules (BF_3, CF_4, CO and F_2) at high photoelectron energies by analyzing the role of the nuclear motion. In collaboration with the experimental groups of Edwin Kukk (Turku University), Catalin Miron (Soleil Synchrotron), Kiyosi Ueda (SPring8 Synchrotron) and Thomas Darrah Thomas (Oregon State University), we have found evidence of intramolecular scattering occurring in the inner-shell photoionization of CO, CF_4 and BF_3 imprinted the collective vibrational excitation that accompanies 1s ionization from the C (CO, CF_4) or the B (BF_3) atom at high photoelectron energies. The ratios between vibrationally resolved photoionization cross sections (ν-ratios) show pronounced oscillations as a function of the photon energy which are the fingerprint of electron diffraction by the surrounding atomic centers and therefore carry information of the molecular target as well as of the ionization process. As a proof of principle, we illustrated how structural information can be retrieved from the oscillations in the v-ratios by determining the internuclear distances of the CO molecule and of the core-hole species generated upon C 1s ionization. A different scenario occurs when the electron is emitted not from a well confined region in the molecule but from a delocalized orbital. In these situations, double (triple...) slit-like interferences are expected to arise. We have investigated this phenomenon in the F_2 molecule, where due to symmetry the orbitals are delocalized between the two atomic centers. By analyzing the role of the nuclear motion upon photoabsorption, we found experimentally measurable evidence of double slit-like

interferences in the angle-integrated photoelectron spectra. These results are presented in chapter 4 and in appendices $1-5$.

Ultrashort light pulses can create coherent superpositions of electronic states, triggering electron motion at a speed that is determined by the energy spacing of the interfering states. We have investigated the ultrafast electronic response of large biological systems to attosecond XUV pulses, in collaboration with the experimental groups of Mauro Nisoli (Politecnico di Milano), Luca Poletto (IFN-CNR, Padova) and Jason Greenwood (Queen's University, Belfast). Our study, presented shown in chapter 5 and in appendices 6 and 7, includes the amino acids glycine, phenylalanine and tryptophan, with the aim of understanding the influence of the different radicals in the ultrafast dynamics. For each molecule, we have evaluated the electronic wave packet generated by an attosecond XUV pulse by means of the static-exchange DFT method and first-order time-dependent perturbation theory. The Fourier analysis of the hole density over different portions of the molecule reveals ultrafast beatings that are in very good agreement with the oscillations found in a XUV/NIR pump-probe experiment where the yield of different fragments is measured as a function of the pump-probe time delay.

Theory

Chapter 1

Light-matter interaction

The aim of this chapter is to introduce general concepts on light-matter interaction and to present theoretical approaches that can describe the behavior of atomic and molecular systems in an electromagnetic field. We focus on the interaction with "weak" radiation, which can be accurately described using perturbative approaches. The general concepts presented here will be applied to treat particular problems in chapters 2 and 3.

1.1 Time-dependent Schrödinger equation

The evolution of an atomic or a molecular system is fully determined by the time-dependent Schrödinger equation (TDSE) [89]:

$$i\hbar\frac{\partial}{\partial t}\Phi(t) = \hat{H}(t)\Phi(t) \tag{1.1}$$

where $\Phi(t)$ is the corresponding wave function and $\hat{H}(t)$ is the Hamiltonian operator. For the sake of simplicity, nor spatial or spin coordinates are explicitly indicated. The formal solution of the TDSE is:

$$\Phi(t) = U(t_0, t)\Phi(t) \tag{1.2}$$

where $U(t_0, t) = e^{-\frac{i}{\hbar}\int_{t_0}^{t}\hat{H}(\tau)d\tau}$ is so called the evolution operator, which propagates the wave function from an initial time t_0 to t. Equations 1.1 and 1.2 are general and, in principle, applicable to any system. Our goal is to investigate the behavior of matter upon interaction with bright light, concretely, ultrashort laser pulses and synchrotron radiation. These are usually intense enough so that one can describe the flux of photons as a continuum variable, i.e., by means of Maxwell equations [89, 34]. Furthermore, in these contexts magnetic interactions are usually weaker and light can be modeled as an oscillating electric field. Neglecting spin orbit couplings, mass polarization and relativistic effects, the

Hamiltonian operator of a set of N charged particles may be written as:

$$\hat{H}(t) = \underbrace{\sum_{i=1}^{N}\left[\frac{\hat{\mathbf{p}}_\mathbf{i}^2}{2m_i} + \sum_{j=1}^{N}\frac{q_i q_j}{|\mathbf{r_i}-\mathbf{r_j}|^2}\right]}_{H_0} + \underbrace{\sum_{i=1}^{N} q_i \mathbf{r}_i \mathbf{E}(t)}_{\hat{V}(t)} \tag{1.3}$$

where $\mathbf{r}_i$, $\mathbf{p}_i$, m_i and q_i are position, momentum, mass and charge of the i-th particle, respectively, and $\mathbf{E}(t)$ is the electric field of the electromagnetic wave in the dipole approximation [89, 34], which neglects the spatial dependence of the field across size of the system. This is usually a good approach for long and medium wavelength fields and for small atomic systems as long as the wavelength is significantly larger than the dimensions of the system. For our purposes, it is convenient to split $\hat{H}$ into two parts (see eq. 1.3): the field-free Hamiltonian, $\hat{H}_0$, and a term accounting for the interaction with the radiation, $\hat{V}(t)$.

Spectral methods

Even though eq. 1.1 has not an exact analytical solution in most cases, it can be solved approximately. For instance, one can define an initial wave function at $t = 0$ in a grid of points and then propagate numerically. However, these methods are typically expensive since one has to use a dense grid in order to get accurate results. In quantum chemistry it is more efficient to use a spectral method, in which the wave function is expanded onto a complete basis set of functions. Of course, the efficiency here depends on the adequate choice of the basis set for the particular problem. It is usually a good approach to use the eigenstates of the field-free Hamiltonian, which are the solutions of the the eigenvalue problem:

$$\hat{H}_0\phi_n = E_n\phi_n \tag{1.4}$$

where ϕ_n are the eigenfunctions of H_0, which form a complete basis set, and E_n are the corresponding eigenvalues. The total wave function can be expanded as

$$\Phi(t) = \sum_n c_n(t)\phi_n \tag{1.5}$$

where the time dependence is contained in the spectral coefficients $c_n(t)$, which satisfy

$$c_n(t) = \langle\phi_n|\Phi(t)\rangle \tag{1.6}$$

due to the orthogonality of the basis. Inserting the spectral expansion of the wave function (eq. 1.5) into the TDSE (eq. 1.1), we obtain

$$i\hbar\frac{\partial}{\partial t}\sum_k c_k|\phi_k\rangle = \sum_n c_n[E_n + \hat{V}(t)]\phi_n \tag{1.7}$$

where we have made use of eq. 1.4. By left-side projecting onto $\langle\phi_k|$ and applying the orthogonality relation $\langle\phi_m|\phi_n\rangle = \delta_{mn}$, eq. 1.7 reads

$$i\hbar\frac{d}{dt}c_n(t) = c_n E_n + \sum_k c_k\langle\phi_n|\hat{V}(t)|\phi_k\rangle \tag{1.8}$$

We have obtained a set of coupled equations that describe the time-evolution of the spectral coefficients. A more compact version of eq. 1.8 can be obtained by performing the change of variables

$$c_n(t) = \tilde{c}_n(t)e^{-iE_n t/\hbar} \tag{1.9}$$

where $\tilde{c}_n(t)$ are the coefficients in the interaction picture [89], which are equivalent to those in the Schrödinger picture $c_n(t)$ except for the corresponding stationary phases. Inserting eq. 1.9 into eq. 1.8 and multiplying by $e^{-iE_n t/\hbar}$, we obtain

$$i\hbar\frac{d}{dt}\tilde{c}_n(t) = \sum_k \tilde{c}_k(t)e^{i\omega_{nk}t}\langle\phi_n|\hat{V}(t)|\phi_k\rangle \tag{1.10}$$

Where we have introduced the Bohr angular frequency $\omega_{nk} = \frac{En-E_m}{\hbar}$. This set of coupled equations is completely general and rigorously equivalent to eq. 1.1. The coupling between different states arises from the existence of the external potential $\hat{V}(t)$, which relates the evolution of $\tilde{c}_n(t)$ to that of all the other coefficients. In general, eq. 1.10 can be solved numerically by breaking the time domain into small steps $\{t_1, t_2, ...\}$ and the set $\{\tilde{c}_n(t_j)\}_n$ is obtained from $\{\tilde{c}_n(t_{j-1})\}_n$ through iterative procedures [90, **?**, 91]. However, this approach might become computationally expensive in some situations. If the external potential $\hat{V}(t)$ is weak, the time-evolution of the wave function can be evaluated more efficiently making use of perturbation theory, as we explain in the next section.

1.2 Time-dependent perturbation theory

Perturbation theory provides a useful approach to solve the TDSE when the field applied to the system is weak and therefore $\hat{V}(t)$ can be treated as a perturbation. Under this assumption, the set of coefficients $\tilde{c}_n(t)$ hardly vary in time and their zero-th order solution is given by their initial values:

$$\tilde{c}_n^{(0)}(t) \simeq \tilde{c}_n(0) \tag{1.11}$$

Solutions of higher order ($r > 0$) can be evaluated using the recurrence relation:

$$i\hbar\frac{d}{dt}\tilde{c}_n^{(r)}(t) = \sum_k \tilde{c}_k^{(r-1)}(t)e^{i\omega_{nk}t}\langle\phi_n|\hat{V}(t)|\phi_k\rangle \tag{1.12}$$

which enables to obtain the r-th order solution from the $(r-1)$-th order one. We are interested in situations in which non linear processes are negligible and can

thus be accurately described using **first-order perturbation theory**, which approximates the exact wave function to its first-order solution. If the system is assumed to be in the ground state at $t = 0$, that is, $\tilde{c}_n(0) = \delta_{0n}$, the zero-th order solution is $\tilde{c}_n^{(0)}(t) = \delta_{0n}$. Inserting this into the right side of eq. 1.12, we can evaluate the first order solution:

$$i\hbar \frac{d}{dt}\tilde{c}_n^{(1)}(t) \simeq e^{i\omega_{n0}t}\langle\phi_n|\hat{V}(t)|\phi_0\rangle \tag{1.13}$$

By integrating in time and making use of the initial condition $\tilde{c}_n(0) = \delta_{0n}$ we obtain:

$$\tilde{c}_n^{(1)}(t) \simeq \delta_{0n} - \frac{i}{\hbar}\int_0^t e^{i\omega_{n0}\tau}\langle\phi_n|\hat{V}(\tau)|\phi_0\rangle d\tau \tag{1.14}$$

In our particular case $\hat{V}(t) = \boldsymbol{\mu}\mathbf{E}(t)$, where $\mu = \sum_n q_n \mathbf{r}_n$ is the dipole moment operator. Using eq. 1.9 we can retrieve the coefficients in the Schrödinger picture. For $n \neq 0$, we have

$$\boxed{c_n^{(1)}(t) = -\frac{i}{\hbar}\langle\phi_n|\boldsymbol{\mu}_{\boldsymbol{\varepsilon}}|\phi_0\rangle e^{-iE_n t/\hbar}\int_0^t e^{i\omega_{n0}\tau}E(\tau)d\tau} \tag{1.15}$$

where $\boldsymbol{\mu}_{\boldsymbol{\varepsilon}} = \hat{\boldsymbol{\varepsilon}}\boldsymbol{\mu}$ is the component of the dipole operator along $\hat{\boldsymbol{\varepsilon}}$, the polarization direction of the field. Eq. 1.15 can provide accurate values of the time-dependent coefficients upon interaction with an ultrashort laser pulse provided only linear effects come into play. The corresponding transition probabilities are given by the square of the amplitudes

$$P_{n\leftarrow 0}(t) = |c_n(t)|^2 = |\tilde{c}_n(t)|^2 \tag{1.16}$$

where one can use $c_n(t)$ or $\tilde{c}_n(t)$ since they are equal except for a stationary phase.

1.2.0.1 The special case of a sinusoidal perturbation

Let us consider the case of monochromatic light in the dipole approximation, i.e.,

$$\mathbf{E}(t) = E_0 \sin(\omega t)\hat{\boldsymbol{\varepsilon}} = \frac{E_0}{2}\left[e^{i\omega t} - e^{-i\omega t}\right]\hat{\boldsymbol{\varepsilon}} \tag{1.17}$$

where ω is the frequency of the radiation. This is a reasonable approach to model an experiment with synchrotron radiation, where the photon energy is well defined [36]. Inserting eq. 1.17 into eq. 1.15, we obtain:

$$\tilde{c}_n^{(1)}(t) = -\frac{iE_0}{2\hbar}\langle\phi_n|\boldsymbol{\mu}_{\boldsymbol{\varepsilon}}|\phi_0\rangle\int_0^t\left[e^{i(\omega_{n0}+\omega)\tau} - e^{i(\omega_{n0}-\omega)\tau}\right]d\tau \tag{1.18}$$

$$= -\frac{iE_0}{2\hbar}\langle\phi_n|\boldsymbol{\mu}_{\boldsymbol{\varepsilon}}|\phi_0\rangle\left[\frac{1-e^{i(\omega_{n0}+\omega)t}}{\omega_{n0}+\omega} - \frac{1-e^{i(\omega_{n0}-\omega)t}}{\omega_{n0}-\omega}\right] \tag{1.19}$$

By making use of eq. 1.16 we can evaluate the transition probability:

$$P_{n\leftarrow 0}(t) = |\tilde{c}_n|^2(t) = \frac{E_0^2}{4\hbar^2}|\langle\phi_n|\boldsymbol{\mu}_{\boldsymbol{\varepsilon}}|\phi_0\rangle|^2\left|\frac{1-e^{i(\omega_{n0}+\omega)t}}{\omega_{n0}+\omega} - \frac{1-e^{i(\omega_{n0}-\omega)t}}{\omega_{n0}-\omega}\right|^2 \tag{1.20}$$

For a fixed value of t, the transition probability is a function of ω having two pronounced maxima for $\omega = \omega_{0n}$ and $\omega = -\omega_{0n}$ due to the two terms inside the bracket. The first term, which maximizes for $\omega = -\omega_{0n}$, accounts for transitions from the initial to lower energy states occurring through induced photoemission. Here we seek to describe excitations that take place upon photoabsorption from the ground state. These are accounted for in the second term, which maximizes for $\omega = \omega_{0n}$. Removing the induced photoemission term in eq. 1.20 and making use of the identity $e^{i\alpha} - 1 = 2ie^{i\alpha/2}\sin(\alpha/2)$, we obtain:

$$P_{n\leftarrow 0}(t) = \frac{E_0^2}{\hbar^2}|\langle\phi_n|\boldsymbol{\mu}_{\boldsymbol{\varepsilon}}|\phi_0\rangle|^2\frac{\sin^2\left([\omega_{n0}-\omega]t/2\right)}{(\omega_{n0}-\omega)^2} \tag{1.21}$$

Here we are interested in finding the transition probability upon a long-time interaction. In the limit $t \to \infty$, the function $\frac{\sin^2(\alpha t/2)}{\alpha^2}$ can be approximated by $\frac{\pi t}{2}\delta(\alpha)$. Then, in the long-time limit, we have:

$$P_{n\leftarrow 0}(t) = \frac{\pi E_0^2 t}{2\hbar^2}|\langle\phi_n|\boldsymbol{\mu}_{\boldsymbol{\varepsilon}}|\phi_0\rangle|^2\delta(\omega_{n0}-\omega) \tag{1.22}$$

Note that this limit corresponds to the case of perfectly monochromatic light, where the photon energy is well defined and given by $\hbar\omega$. Therefore, a transition from the ground to an excited state n will only occur if $\omega = \omega_{0n}$. The transition rate, i.e., the transition probability per unit of time is obtained by integrating over a range of frequencies (ω_1, ω_2) containing ω_{n0} and derivating with respect to time:

$$\Gamma_{n\leftarrow 0} = \frac{d}{dt}\int_{\omega_1}^{\omega_2} P_{n\leftarrow 0}(t)d\omega = \frac{\pi E_0^2}{2\hbar^2}|\langle\phi_n|\boldsymbol{\mu}_{\boldsymbol{\varepsilon}}|\phi_0\rangle|^2 \tag{1.23}$$

1.3 Photoionization cross section

The cross section is defined as the hypothetical surface of effective interaction between a flux of particles and their targets. In the particular case of photoionization, it refers to the probability of an electron to be emitted from the target upon interaction with the field. For a transition from the ground Φ_0 a to a final Φ_n state, the cross section is given by [89]:

$$\sigma = \frac{\Gamma_{n\leftarrow 0}}{F} \tag{1.24}$$

where F is the flux of photons per unit of area and time, which is related to the amplitude of the electric E_0 according to

$$F = \frac{E_0^2 c}{8\pi\hbar\omega} \tag{1.25}$$

and c is the speed of light. Inserting 1.23 and 1.25 into 1.24, we obtain the photoionization cross section for a given orientation of the system with respect to the field:

$$\boxed{\sigma_{\boldsymbol{\varepsilon}} = \frac{4\pi^2\omega}{\hbar c}|\langle\phi_n|\boldsymbol{\mu}_{\boldsymbol{\varepsilon}}|\phi_0\rangle|^2} \tag{1.26}$$

As can be seen in eq. 1.26, the cross section does not depend on the parameters of the field. For this reason, it is a very useful quantity to compare results obtained under different experimental conditions.

1.3.0.2 Randomly oriented targets

In the case of randomly oriented molecules, the total cross section can be retrieved by averaging incoherently over three orthogonal directions of $\boldsymbol{\varepsilon}$, let us call them $\mathbf{x}$, $\mathbf{y}$ and $\mathbf{z}$:

$$\sigma = \frac{\sigma_{\mathbf{x}} + \sigma_{\mathbf{y}} + \sigma_{\mathbf{z}}}{3} \tag{1.27}$$

Eq. 1.27 allows to reproduce experimental results in which targets without spherical symmetry are are not aligned with the field.

Chapter 2

Molecular structure

In this chapter we show how to apply the general concepts introduced in chapter 1 to describe the interaction of molecules with electromagnetic radiation. In particular, we are interested in processes involving ionization. The main difference between atomic and molecular photoionization is that in the atomic case the angular momentum of the emitted electron is a good quantum number. Due to the lack of spherical symmetry, this is no longer true in the case of a molecule, where the description of the electronic continuum requires solving a multichannel problem [92]. Besides, there are extra degrees of freedom because the nuclei move. Here we present approaches to describe these situations, introducing reasonable approximations that can simplify the full problem, which, as the number of degrees of freedom increases, becomes intractable.

2.1 The molecular Hamiltonian

The Hamiltonian operator representing the energy of the electrons and the nuclei in a molecule, the field-free molecular Hamiltonian, may be written as [93]:

$$\hat{H} = \hat{T}_e + \hat{T}_N + \hat{V}_{ee} + \hat{V}_{eN} + \hat{V}_{NN} \tag{2.1}$$

where:

- $T_e = \frac{1}{2}\sum_{i=1}^{N}\frac{1}{m_e}\nabla_i^2$ is the kinetic energy of the N electrons,
- $\hat{T}_N = \frac{1}{2}\sum_{i=1}^{M}\frac{1}{M_\alpha}\nabla_\alpha^2$ is the kinetic energy of the M nuclei,
- $\hat{V}_{ee} = \sum_{i=1}^{N}\sum_{j>i}^{N}\frac{e^2}{|\mathbf{r}_i - \mathbf{r}_j|}$ is the electrostatic repulsion between electrons,
- $\hat{V}_{eN} = -\sum_{i=1}^{N}\sum_{\alpha=1}^{M}\frac{Z_\alpha e^2}{|r_i - \mathbf{R}_\alpha|}$ is the attraction between electrons and nuclei,
- $\hat{V}_{NN} = \sum_{\alpha=1}^{M}\sum_{\beta>\alpha}^{M}\frac{Z_\alpha Z_\beta e^2}{|\mathbf{R}_\alpha - \mathbf{R}_\beta|}$ is the repulsion energy term between nuclei,

$\mathbf{r}_i$ and $\mathbf{R}_\alpha$ stand for the coordinates of the electron i and nuclei α, respectively, m_e and e are the mass and the charge of the positron, and M_α and Z_α are the mass and the atomic number of the nuclei α. In order to find the eigenstates of H, which constitute the set of stationary solutions of the molecular system, we can take advantage of the fact that since nuclei are more massive than the light electrons, their motion is slower, as we explain as follows.

2.1.1 The Born-Oppenheimer approximation

Since the electromagnetic forces acting on electrons and nuclei have similar intensity, one might assume their momenta to be of the same magnitude. Then, as the nuclei are significantly heavier, they must accordingly have much smaller velocities. Based on this idea, Max Born and J. Robert Oppenheimer proposed a way to decouple electron and nuclear dynamics by splitting the total wave function into two parts [94]. Within the Born-Oppenheimer approximation, the stationary states of the full-system can written as product of an electronic stationary state $\Psi_n(\bar{\mathbf{x}}, \bar{\mathbf{R}})$, depending on both the electronic and the nuclear coordinates, and a nuclear stationary state $\chi_{n\nu}(\bar{\mathbf{R}})$, which only depends on the nuclear degrees of freedom:

$$\Phi_{n\nu}(\bar{\mathbf{x}}, \bar{\mathbf{R}}) = \Psi_n(\bar{\mathbf{x}}, \bar{\mathbf{R}})\chi_{n\nu}(\bar{\mathbf{R}}) \tag{2.2}$$

where n and ν are indexes (in general, sets of indexes) over the electronic and nuclear stationary states, which label the $\Phi_{n\nu}$ vibronic stationary state state, $\bar{\mathbf{x}} = (\mathbf{x}_1, ..., \mathbf{x}_N)$ is a vector containing the spin and spatial coordinates of all electrons and $\bar{\mathbf{R}} = (\mathbf{R}_1, ..., \mathbf{R}_M)$ contains all nuclear spatial coordinates (nuclear spin coordinates have been dropped). Electronic stationary states satisfy the electronic time-independent Schrödinger equation:

$$\Big[\underbrace{\hat{T}_e + \hat{V}_{ee} + \hat{V}_{eN} + \hat{V}_{NN}}_{\hat{H}_e}\Big]\Psi_n(\bar{\mathbf{x}}, \bar{\mathbf{R}}) = E_n(\bar{\mathbf{R}})\Psi_n(\bar{\mathbf{x}}, \bar{\mathbf{R}}) \tag{2.3}$$

where H_e is the electronic Hamiltonian and $E_n(\bar{\mathbf{R}})$ is the energy of the electronic state n, which depends on the nuclear coordinates $\tilde{\mathbf{R}}$. Eq. 2.3 can be solved parametrically in a grid of nuclear geometries and, by doing so, one obtains the potential energy surfaces $E_n(\bar{\mathbf{R}})$ in which the nuclei move. Then, for each electronic state n, the nuclear stationary states $\chi_{n\nu}$ can be obtained by solving nuclear time-independent Schrödinger equation:

$$\Big[\underbrace{T_N + E_n(\bar{\mathbf{R}})}_{\hat{H}_N}\Big]\chi_{n\nu}(\bar{\mathbf{R}}) = E_{n\nu}\chi_{n\nu}(\bar{\mathbf{R}}) \tag{2.4}$$

where $E_{n\nu}$ is energy of the vibronic state given by the quantum numbers n and ν. The BO approximation assumes that $\Phi_{n\nu}(\bar{\mathbf{x}}, \bar{\mathbf{R}})$ varies very smoothly with $\bar{\mathbf{R}}$ and therefore the electrons rearrange instantaneously as the nuclei move. This assumption is valid as long as the energy spacing between electronic states, i.e., $E_n(\bar{\mathbf{R}}) - E_{n-1}(\bar{\mathbf{R}})$ is sufficiently large and, in a photoionization process, as long as the photoelectron is not emitted very slowly, that is, with very low kinetic energy. The Born-Oppenheimer approximation provides a powerful tool for the accurate evaluation of vibronic stationary states of diatomic and small polyatomic molecules, and also of larger systems in which reduced-dimensionality models are applicable.

2.1.1.1 The fixed-nuclei approximation

Purely electronic processes may occur in a time-scale which is short enough so that they can be described without taking into account the nuclear degrees of freedom at all. In these situations, the system can be characterized in terms of an electronic wave function in which the nuclei remain frozen at their equilibrium positions. The so called fixed-nuclei approximation has been widely employed, for instance, for the evaluation of total photoionization cross sections (see, for instance [95, 96, 97]), providing results in which are in good agreement with full-calculations and with experimental data, or for the investigation of charge migration in large biological systems [27, 58, 26, 59, 62, 98], where including the nuclear degrees of freedom may become challenging.

2.2 Evaluation of electronic states

The electronic eigenvalue problem given in eq. 2.3 is a differential equation depending on the coordinates of all the electrons which, in general, does not have an exact analytical solution. The Hartree−Fock (HF) method can provide a first approximation to the "exact" ground state solution in terms of a Slater determinant constructed from HF molecular orbitals, which are obtained within the mean field approximation through a self consistent field procedure. However, HF solutions are usually rather poor since the mean field approximation cannot properly describe electron correlation effects [93]. Post HF methods manage this problem by expanding the total wave function as a linear combination

of Slater determinants (electronic configurations), being able to yield accurate solutions for the ground and for excited states of few electron systems. Yet, the number of configurations one might need to include in the expansion to reach the desired accuracy can make these methods extremely costly. In this sense, density functional theory (DFT) provides a useful alternative to the conventional *ab initio* methods, providing an excellent compromise between accuracy and computational effort for medium and large size systems [99].

2.2.1 Density functional theory

Density functional theory (DFT) is widely used in physics, chemistry and materials science to investigate the ground state electronic structure of atoms, molecules, and condensed phases. According to DFT, the energy (or any other observable) of a many-electron system in the ground state can be determined by using functionals which solely depend on the electron density. The most essential concepts of the method are given here; for a deeper insight, see, for instance [99], [100] or [101].

DFT is supported on the theorems proposed by Pierre Hohenberg and Walter Kohn in 1964 [102], namely:

1. "Any observable of a stationary non-degenerate ground state can be calculated, exactly in theory, from the electron density of the ground state".
2. "The electron density of a non-degenerate ground state can be calculate, exactly in theory, determining the density that minimizes the energy of the ground state".

The use of the electron density $\rho(\mathbf{r})$ instead of the wave function $\Psi(\mathbf{x}_1, ..., \mathbf{x}_N)$ is the foundantion of DFT. Both entities are related through the equation:

$$\rho(\mathbf{r}) = N \int \dots \int |\Psi(\mathbf{x}, \mathbf{x}_2 \dots d\mathbf{x}_N)|^2 ds d\mathbf{x}_2 \dots d\mathbf{x}_N \tag{2.5}$$

where $\mathbf{x}_i = \mathbf{r}_i s_i$ gathers the spatial $\mathbf{r}_i$ and spin s_i coordinates of the $i-$th electron [1]. In 1965, Walter Kohn and Lu Jeu Sham provided a systematical approach to evaluate the ground state electron density of a many-body system by introducing the so-called Kohn-Sham equation [103].

The Kohn-Sham equation

The Kohn-Sham equation is the time-independent Schrödinger equation of a fictitious system of non-interacting particles that generates the same density as a given system of interacting particles. It can be written as:

$$\Big[-\frac{\hbar^2}{2m_e}\nabla^2 + V_{\text{eff}}(\mathbf{r}) \Big] \phi_i(\mathbf{x}) = \epsilon_i \phi_i(\mathbf{x}) \tag{2.6}$$

[1] The parametrical dependence on the nuclear coordinates has been dropped for the shake of simplicity.

where ϕ_i are the so called Kohn-Sham orbitals, ϵ_i are the corresponding energies and V_{eff} the fictitious effective potential in which the non-interacting particles move:

$$V_{\text{eff}}(\mathbf{r}) = -\sum_{\alpha=1}^{M} \frac{e^2 Z_\alpha}{|\mathbf{r} - \mathbf{R}_\alpha|} + V_H[\rho(\mathbf{r})] + V_{XC}[\rho(\mathbf{r})] \tag{2.7}$$

where V_H is the Hartree (Coulomb) potential

$$V_H[\rho(\mathbf{r}_i)] = e^2 \int \frac{\rho(\mathbf{r}')}{|\mathbf{r} - \mathbf{r}'|} d\mathbf{r}' \tag{2.8}$$

and V_{XC} is the exchange-correlation potential

$$V_{XC}[\rho(\mathbf{r})] = \frac{\delta E_{XC}}{\delta \rho} \tag{2.9}$$

E_{XC} is the exchange-correlation energy. If the exact forms of E_{XC} and V_{XC} where known, the Kohn-Sham strategy would provide the exact ground state energy. Unfortunately, this is not the case and the exchange-correlation energy (potential) needs to be approximated through empirical formulations. The central goal of modern DFT is finding better approximations to these two quantities. As the particles of the Kohn-Sham system are non-interacting fermions, the ground state wave function can be written as a Slater determinant of the lowest energy solutions of eq. 2.6:

$$\Psi(\mathbf{x}_1, \mathbf{x}_2, ..., \mathbf{x}_n) = \frac{1}{\sqrt{N!}} \begin{vmatrix} \phi_1(\mathbf{x}_1) & \phi_2(\mathbf{x}_1) & \cdots & \phi_N(\mathbf{x}_1) \\ \phi_1(\mathbf{x}_2) & \phi_2(\mathbf{x}_2) & \cdots & \phi_N(\mathbf{x}_2) \\ \vdots & \vdots & \ddots & \vdots \\ \phi_1(\mathbf{x}_N) & \phi_2(\mathbf{x}_N) & \cdots & \phi_N(\mathbf{x}_N) \end{vmatrix} \tag{2.10}$$

By using eq. 2.5, we can evaluate the ground state electron density:

$$\rho_0(\mathbf{r}) = 2 \sum_{i=1}^{N} |\psi_i(\mathbf{r})|^2 \tag{2.11}$$

where $\psi_i(\mathbf{r})$ is the spatial part of the spin orbital $\phi_i(\mathbf{x})$, that is, $\phi_i(\mathbf{x}) = \psi_i(\mathbf{r})\alpha(s)$ or $\phi_i(\mathbf{x}) = \psi_i(\mathbf{r})\beta(s)$. As the Kohn-Sham Hamiltonian depends on the Kohn-Sham orbitals (solutions of the eigenvalue problem) through the electron density, those are numerically found by using a self-consistent field procedure until convergency is reached.

2.2.2 Static-exchange DFT

Standard DFT methods can accurately represent the electronic ground state many-electron systems. Here we are mainly interested in describing processes that involve photoionization. To do so, one also needs to describe the electronic continuum. In this work we have employed the static-exchange DFT

method [104, 105, 106, 107, 108], developed by Piero Decleva and collaborators, to evaluate transitions to continuum states. The method makes use of the Kohn-Sham DFT formalism to describe bound states and of the Galerkin approach to evaluate photoelectron wave functions in the field of the corresponding Kohn-Sham density. Over the last decades, it has been shown to provide accurate results for the total cross sections of small molecules as well as for medium and large size systems within the fixed nuclei approximation [105, 109, 110, 111, 112, 113]. More recently, it has been used to evaluate of vibrationally resolved cross sections by including the nuclear motion at the Born-Oppenheimer level [78, 83, 79, 80, 81, 82, 84, 85, 86, 87, 88], providing results which are in good agreement with experimental data. In this section we explain the most relevant characteristics of the method. A detailed review of the method is given in [107].

2.2.2.1 Electronic states within the static-exchange approximation

The method makes use of single Slater determinants to define bound and excited (continuum) electronic states, ensuring that the Pauli exclusion principle is fulfilled. The ground state wave function may be written as:

$$\Psi_0(\mathbf{x}_1, \mathbf{x}_2, ..., \mathbf{x}_n) = \left|\phi_1 \;\; \phi_2 \dots \phi_N\right| \tag{2.12}$$

where, for a closed-shell system:

$$\phi_n(\mathbf{x}) = \begin{cases} \psi_{(n+1)/2}(\mathbf{r})\alpha(s) & \text{if } n \text{ is odd} \\ \\ \psi_{n/2}(\mathbf{r})\beta(s) & \text{if } n \text{ is even} \end{cases}$$

Continuum states are defined by promoting one electron from a bound spin orbital ϕ_α to a continuum orbital $\phi_{\varepsilon lh}$ with kinetic energy ε and angular quantum numbers l and h, as we explain in section 2.2.2.2, and can be written as:

$$\Psi_{\alpha\varepsilon lh}(\mathbf{x}_1, \mathbf{x}_2, ..., \mathbf{x}_n) = \left|\phi_1 \;\; \phi_2 \dots \phi_{\alpha-1} \;\; \phi_{\varepsilon lh} \;\; \phi_{\alpha+1} \dots \phi_N\right| \tag{2.13}$$

Bound and continuum orbitals are expanded in a multicentric basis set of B-splines, as we explain as follows.

2.2.2.2 Multicentric B-spline basis set

Traditional basis sets make use of Gaussian or Slater type orbital functions, which provide fast convergence for the lowest bound states with a reduced number of basis functions [93]. However, these expansions are not adequate for the description of the rapidly oscillating continuum states, since numerical linear dependences rapidly come up as the basis set is increased due to the large overlap between functions with different centers. In this context, B-spline functions are very flexible and due to its local nature they can describe accurately both bound and continuum orbitals without running intro numerical dependencies

[107]. The present method evaluates bound and continuum orbitals in a multicentric basis set of B-splines and symmetry adapted [114] linear combinations of real spherical harmonics with origin over different positions in the molecule:

- A large one-center expansion (OCE) over the center of mass provides an accurate description of the long-range behavior of the continuum states.
- Small expansions, called off-centers (OC), located over the non-equivalent nuclei, complement the OCE. They improve dramatically the convergence of the calculation, allowing to reduce the angular expansion in the OCE, since they can effectively describe the Kato cusps [115] at the nuclear positions.

In the case of symmetric molecules, a large amount of computational effort can be saved by making use of using point group symmetry and dividing the 3-dimensional space into equivalent regions (see fig. 2.2.2.2 for a schematic representation of in the BF_3 molecule). The basis set elements may be written as:

$$\xi^p_{nlh\lambda\mu} = \sum_{q\in\Lambda_p} \frac{1}{r_q} B^\kappa_n(r_q) \underbrace{\sum_m b^q_{mlh\lambda\mu} Y_{lm}(\theta_q,\varphi_q)}_{X^p_{lh\lambda\mu}(\theta_q,\varphi_q)} \tag{2.14}$$

where Λ_p represents a shell of equivalent centers ($p = 0$ refers to the OCE), q runs over the centers in the shell, n is an index over the B-spline functions B^κ_n, whose order is $\kappa = 10$, $\lambda\mu$ are the indexes of the irreducible representation (see [108]), h runs over the linearly independent angular functions, which are constructed as linear combinations of real spherical harmonics associated to a fixed angular quantum number l, and the coefficients $b^q_{mlh\lambda\mu}$ are determined by symmetry [114], defining the so called symmetry adapted spherical harmonics $X^p_{lh\lambda\mu}$.

In each center q, the B-spline expansion reaches a maximum value $R^p_{\max}$, can be different for non-equivalent centers (different value of p, see eq. 2.14). A large vale of R^0_{max} is required in the OCE in order to provide a good description of the oscillatory behavior of the continuum states. One can control the overlap between the basis elements, avoiding running into linear dependences, by keeping a small expansions over the off-centers ($R^{p>0}_{max} \simeq 1 a.u.$), which are usually enough to account for of the Kato cusps. Angular expansions are truncated so l takes values up to a maximum $l^p_{\max}$, which can also be different for the non-equivalent centers. In general, small values of $l_{\max}$ in the OCs are enough to complement the OCE in the description of the bound states, whereas the a large angular expansion might be required in the OCE for the evaluation of continuum states with high kinetic energy.

Evaluation of bound orbitals

Nowadays there are several electronic structure programs available which can efficiently perform DFT calculations. We have employed the Amsterdam Density Functional (ADF) package [116, 117, 118] to evaluate the electronic density

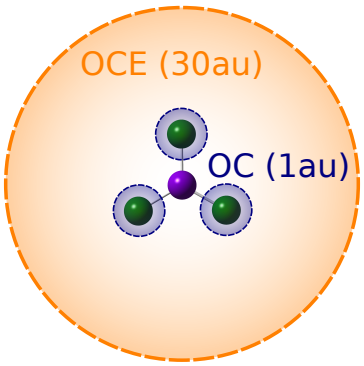

Figure 2.1: Schematic representation of the multicentric expansion in the BF_3 molecule: a large OCE ($R_{0\max} = 30$ a.u.) with origin on the B atom and 3 equivalent OCs ($R_{1\max} = 1$ a.u.) placed on the F atoms. No OC is required on the B atom as it is located at the center of mass, where the OCE has its origin. Since the molecule belongs to the D_{3h} point group, signifficant computational effort is saved by dividing the 3-dimensinal space into 12 equivalent regions.

of the ground state of the molecules we have investigated using double or a triple ζ-polarization plus basis set (taken from the ADF library). Electronic exchange and correlation effects have been accounted for with the VWN [119] local density approximation functional in some cases, or with the LB94 [120], depending on each particular problem. The electron density provided by ADF is projected into a multicentric B-spline basis set like the one described in the previous section. The corresponding Hamiltonian $\mathbf{H}$ and overlap $\mathbf{S}$ matrices are then constructed, and by solving the eigenvalue problem given by the secular equation

$$\mathbf{Hc} = E\mathbf{Sc} \tag{2.15}$$

we obtain the set coefficients $\mathbf{c}$ that define the bound orbitals in the B-spline basis.

Evaluation of continuum orbitals

The continuum spectrum of an operator constitute a family of eigenfunctions depending of the corresponding eigenvalue as a continuum variable. The set of discrete solutions of eq. 2.15 whose energy is higher than the ionization threshold can be interpreted as a representation of the continuum, but with a different (arbitrary) normalization condition: $\varphi(R^0_{\max}) = 0$, and normalized at the same level as the bound states: to a Kronecker delta. Of course, the characteristics of these solutions depend on the numerical expansion and one needs to use a dense basis set and a large value of $R^0_{\max}$ so their asymptotic behavior is propertly represented. In order to compute measurable quantities such as photoionization cross sections, one needs to set the proper normalization of the continuum states: to a Dirac delta, and impose the adequate scattering

boundary conditions of a multichannel problem. Here we have employed the Galerkin [107] approach to evaluate photoelectron states at different energies and the correct boundary conditions have been imposed to the solutions, as we explain in this section.

◦ The Galerkin approach

The present method can yield the continuum wave function at any photoelectron energy using a fixed basis set. The traditional eigenvalue problem (eq. 2.15) does not admit non-trivial solutions ($\mathbf{c} \neq \mathbf{0}$) for an arbitrary value of energy $E = \varepsilon$. However, one can obtain approximate solutions by finding the coefficients that minimize the residual vector ($\mathbf{Hc} - \varepsilon\mathbf{Sc}$), with $\mathbf{c} \neq \mathbf{0}$ by solving the eigenvalue problem:

$$\mathbf{A}(\epsilon)\mathbf{c} = a\mathbf{c} \tag{2.16}$$

where $\mathbf{A}(\epsilon) = \mathbf{H} - \epsilon\mathbf{S}$. The eigenfunctions corresponding to the lowest eigenvalues $a_0, a_1, ...$ can be taken as an approximate solutions with energy ϵ if their eigenvalues are close to zero. It has been observed that, for n partial waves, one can always find a set of n eigenvalues $\{a_i\}_{i=1}^{n}$ whose moduli are sufficiently small and well separated from the others, provided that the basis set is dense and flexible enough. Due to the lack of boundary conditions, $\mathbf{A}(\epsilon)$ is not a Hermitian matrix and therefore its eigenvalues a_i and eigenvectors $\mathbf{c}_i$ are, in general, complex. Nonetheless since $\mathbf{A}(\varepsilon)$ is real they appear in conjugate pairs, i.e., for each pair $(a, \mathbf{c})$ that satisfies 2.16, so does $(a^*, \mathbf{c}^*)$. This later property makes possible to avoid complex representations just by taking $\mathfrak{R}(\mathbf{c})$ and $\mathfrak{I}(\mathbf{c})$ as independent solutions.

The diagonalization of $A(\epsilon)$ provides, for a selected photoelectron energy ϵ, an orthonormal set $\{\varphi_{\epsilon,i}\}_i$ of real stationary solutions. However, these solutions do not satisfy the adequate scattering boundary conditions. Nonetheless, since they form a complete set, we recombine them to obtain linear combinations of them that do.

◦ Renormalization of continuum sates

Photoelectron wave functions describe a particle being ejected out of an atom or a molecule. Therefore, they must be solutions of the scattering Schrödinger equation

$$\hat{H}_{sc}\varphi^{-}(\mathbf{r}) = \varepsilon\varphi^{-}(\mathbf{r}) \tag{2.17}$$

where $\hat{H}_{sc}$ is the scattering Hamiltonian:

$$\hat{H}_{sc} = -\frac{1}{2}\nabla^2 - U_\alpha(\mathbf{r}) \tag{2.18}$$

and $U_\alpha(\mathbf{r})$ is the electrostatic potential generated by the residual ion. At long distances, this potential can be approximated by that of a positive charge, i.e.:

$$\lim_{r\to\infty} U_\alpha(\mathbf{r}) = \frac{1}{r} \tag{2.19}$$

where $r = |\mathbf{r}|$. The scattering Hamiltonian (equation 2.17) does not admit analytical eigenfunctions in the case of complex electrostatic potentials. However, as r increases, it tends to the Coulomb Hamiltonian, $\hat{H}_c$:

$$\lim_{r\to\infty} H_{sc} = H_c = -\frac{1}{2}\nabla^2 - \frac{1}{r} \tag{2.20}$$

which does have analytical solutions: the regular $F_{\varepsilon l}(r)$ and the irregular $G_{\varepsilon l}(r)$ Coulomb functions. At long distances, they can be written as:

$$F_{\varepsilon l}(r) = \sqrt{\frac{2}{\pi k}}\frac{1}{r}\sin\left(kr - l\frac{\pi}{2} - \eta\log 2kr + \sigma_l\right) \tag{2.21}$$

$$G_{\varepsilon l}(r) = \sqrt{\frac{2}{\pi k}}\frac{1}{r}\cos\left(kr - l\frac{\pi}{2} - \eta\log 2kr + \sigma_l\right) \tag{2.22}$$

where k is the momentum and σ_l is the Coulomb phase shift:

$$\sigma_l = \arg\Gamma(l + 1 + i\eta) \tag{2.23}$$

and Γ is the Euler's Gamma function. The asymptotic boundary conditions for the photoelectron scattering wave functions can be written in terms of the Coulomb functions as follows:

$$\varphi^{-}_{\varepsilon lh} = F_{\varepsilon l}(r)X_{lh} + \sum_{l'}\pi K_{ll'}G_{\varepsilon l}(r)X_{l'h} \tag{2.24}$$

where the K-matrix is related to the usual scattering matrix $\mathbf{S}$ [92] as:

$$I - i\pi\mathbf{K} = (I + i\pi\mathbf{K})\mathbf{S} \tag{2.25}$$

Continuum states resulting from the diagonalization of the Galerkin matrix $A(\varepsilon)$, however, satisfy arbitrary boundary conditions of the form:

$$\varphi_{\varepsilon lh} = \sum_{l'} a_{ll'}F_{\varepsilon l'}(r)X_{l'h} + \sum_{l'}\pi K_{ll'}G_{\varepsilon l}(r)X_{l'h} \tag{2.26}$$

where the sets of coefficients $\{a_{ll'}\}$ and $\{b_{ll'}\}$ are obtained by comparing the radial part of the wave functions $\varphi_{\varepsilon l}$ and its first derivative at $r = R_{max}$ with those of the Coulomb functions. They define two matrices $\mathbf{A}$ and $\mathbf{B}$ that can be used to obtain the correct wave functions:

$$\varphi^{-}_{\varepsilon lh} = \mathbf{A}^{-1}\varphi_{\varepsilon lh} \tag{2.27}$$

The resulting wave functions $\varphi^{-}_{\varepsilon lh}$ have the proper K-matrix normalization, with $\pi\mathbf{K} = -\mathbf{A}^{-1}\mathbf{B}$.

2.2.2.3 Dipole-transition matrix elements

Here we indicate how to evaluate the dipole-transition matrix element from the electronic ground state Ψ_0 (eq. 2.12) to a continuum state $\Psi_{\alpha\varepsilon lh}$ (eq. 2.13)

upon interaction with linearly polarized light. Since the residual ion is remain frozen (static-exchange approximation), the problem reduces to the calculation of the coupling between the bound orbital from where the electron is taken ϕ_α and the continuum orbital to where is promoted $\phi_{\varepsilon lh}$, that is,

$$\mu_{\boldsymbol{\epsilon}}^{\alpha\varepsilon lh} = \langle \Psi_{\alpha\varepsilon lh}(\bar{\mathbf{x}}) | \boldsymbol{\mu}_{\boldsymbol{\epsilon}}^{\mathrm{e}}(\bar{\mathbf{r}}) | \Psi_0(\bar{\mathbf{x}}) \rangle = \langle \phi_{\varepsilon lh}(\mathbf{r}) | \boldsymbol{\epsilon}\mathbf{r} | \phi_\alpha(\mathbf{r}) \rangle \tag{2.28}$$

where ϵ is the polarization direction of the electric field. Dipole transition elements can be used to evaluate cross sections, as we indicate as follows.

2.2.2.4 Photoionization cross section within the fixed-nuclei approximation

Making use of equations 1.26 and 2.28 and summing incoherently all photoelectron symmetries (all possible values of l and h), we can evaluate total photoionization cross sections in the framework of the fixed nuclei approximation:

$$\sigma_{\boldsymbol{\epsilon}\alpha}(\varepsilon) = \frac{4\pi^2\omega}{\hbar c} \sum_{lh} \left| \mu_{\boldsymbol{\epsilon}}^{\alpha\varepsilon lh} \right|^2 \tag{2.29}$$

As indicated in section 1.3, for the case of randomly oriented molecules, one needs to compute $\sigma_{\boldsymbol{\epsilon}\alpha}$ for three orthogonal directions of the polarization vector of the field $\boldsymbol{\epsilon}$ and then average the results incoherently.

2.2.3 Time-dependent DFT

The static-exchange DFT method described in the previous section might be inappropriate when the coupling between different photoionization channels is important. In this section we present the alternative time-dependent DFT approach, is more adequate to describe these situations. Since the method makes use of many ingredients from the static-exchange DFT, here we will only explain the concepts that are exclusive from the time-dependent version. For a more complete description, see [109].

The response of the electrostatic potential due to a first order change in the electronic density can be taken into account in a self consistent way, giving rise to a total perturbing potential V_{SCF}, which is the sum of two contributions [121]:

$$V_{SCF}(\mathbf{r}, \omega) = V_{EXT}(\mathbf{r}, \omega) + \delta V(\mathbf{r}, \omega) \tag{2.30}$$

where ω is the frequency of the radiation, V_{EXT} is the potential created by the external field and $\delta V(\mathbf{r}, \omega)$ is the induced potential, which is given by:

$$\delta V(\mathbf{r}, \omega) = \int \frac{\delta(\mathbf{r}, \omega)}{|\mathbf{r} - \mathbf{r}'|} d\mathbf{r}' + \frac{\partial V_{XC}}{\partial n}\Big|_{n=n(\mathbf{r})} \delta n(\mathbf{r}, \omega) \tag{2.31}$$

Where $n(r)$ is the unperturbed electronic density distribution and $\delta(\mathbf{r}, \omega)$ is denotes the deviations from $n(r)$ induced by the applied external field. Equation

2.31 may be rewritten in terms of a kernel K acting on the induced density:

$$\delta V(\mathbf{r},\omega) = \int K(\mathbf{r},\mathbf{r}')\delta n(\mathbf{r}',\omega)d\mathbf{r}' \tag{2.32}$$

In order to solve the linear response equations, we make use of the Modified Sternheimer Approach (MSA) [122]. In the MSA formalism, the KS orbitals perturbed to up to first order $\phi_i^{(1,\pm)}$ are calculated through the inhomogeneous equation:

$$\left(H_{KS} - \epsilon_i \pm \omega\right) = \hat{P}V_{SCF}\phi_i \tag{2.33}$$

Where $\hat{P}$ is a projector operator that orthogonalizes with respect to the occupied states. The induced density can then be obtained as:

$$\delta(\mathbf{r},\omega) = \sum_i n_i(\varphi_i^*\varphi_i^{(1,\pm)} + (\varphi_i\varphi_i^{(1,\mp)*}) \tag{2.34}$$

The linear response equations are solved numerically in a B-splines basis as the one employed in the static-exchange DFT approach and the adequate boundary conditions for the photoelectron wave functions are also imposed. Once V_{SCF} is obtained, the electronic dipole couplings are calculated making use of V_{SCF} instead of the dipole operator.

Although interchannel coupling and singly excited autoionizations effects are included in the present approach, TDDFT cannot describe double or higher excitations. For this reason, the TDDFT approach is expected to be more suitable than the DFT one when describing the correlation due to the coupling between different open ionization channels. It is not guaranteed that it will do so when double excited states are involved. Note, however, that an appropriate description of the electronic continua is achieved, eve using TDDFT, if doubly (triply...) excited states are involved. These states define multiple excitations and they appear as metastable states embedded in the continuum. For an adequate description a full electron-electron correlation should be included.

2.3 Inclusion of the nuclear motion

The nuclear motion may play an important role in the photoionization of molecules because the energy of the incident photon is usually distributed between electrons and nuclei. It is reasonable to see molecular photoionization as a Franck-Condon transition [123, 124, 125, 126], in which as the light electron is emitted quickly, the residual ion is left in a superposition of vibronic states, which leads to (several) vibrational excitations in the parent ion. These are experimentally observable even in inner-shell photoionization, thanks to the advent of the third generation of synchrotron radiation sources and high energy-resolution detection techniques [36]. Of course, in order to describe these situations, the nuclear degrees of freedom must be taken into account. Here we present a method for including the nuclear motion at the Born-Oppenheimer level applicable to diatomic molecules and to small polyatomics in which one vibrational mode is dominant.

2.3.1 The nuclear Hamiltonian

Within the Born-Oppenheimer approximation, the nuclear Hamiltonian (see eq. 2.4) of a **diatomic AB molecule** in a given electronic state n may be written as:

$$\hat{H}_N = -\frac{1}{2M}\nabla^2_{\mathbf{R}_{\rm CM}} \underbrace{-\frac{1}{2\mu}\nabla^2_R + E_n(R)}_{H_{\rm int}} \tag{2.35}$$

where M and μ are the total and the reduced mass of the system, respectively, R is the relative distance between the two nuclei, $\mathbf{R}_{\rm CM}$ is the position of the center of mass and E_n is the corresponding potential energy curve in the Born-Oppenheimer approximation. In this formulation, it is clear that the kinetic energy is composed by a translational motion of the center of mass (first term) and an internal motion (second term). The translational motion is not quatized and just contributes to the total energy by adding a constant energy to the eigenvalues. For this reason, here we will focus on finding the eigenstates of the internal Hamiltonian $H_{\rm int}$ which, in polar coordinates, may be written as:

$$\hat{H}_{\rm int} = -\frac{\hbar}{2\mu}\Big(\frac{\partial^2}{\partial R^2} + \frac{2}{R}\frac{\partial}{\partial R}\Big) + \frac{\hat{L}^2}{2\mu R^2} + E_n(R) \tag{2.36}$$

where $\hat{L}^2$ is the square of the total angular momentum operator. The eigenfunctions of $\hat{H}_{\rm int}$ can be written as a product of a radial part $\chi_{n\nu}(R)$, describing the vibrational motion, and a spherical harmonic $Y_l^m(\theta,\phi)$, that accounts for the molecular rotation. Since the rotational energy is significantly smaller, we can neglect it and describe the nuclear motion in terms of vibrational states $\chi_\nu(R)$, the eigenfunctions of the vibrational Hamiltonian:

$$\hat{H}_{\rm vib}(R) = -\frac{\hbar}{2\mu}\Big(\frac{\partial^2}{\partial R^2} + \frac{2}{R}\frac{\partial}{\partial R}\Big) + E_n(R) \tag{2.37}$$

Vibrational eigenfunctions can be written as:

$$\chi_{n\nu}(R) = \frac{\zeta_{n\nu}(R)}{R} \tag{2.38}$$

which simplifies the eigenvalue problem to:

$$\Big[-\frac{\hbar}{2\mu}\frac{\partial^2}{\partial R^2} + E_n(R)\Big]\zeta_{n\nu}(R) = E_{n\nu}\zeta_{n\nu}(R) \tag{2.39}$$

Vibrational eigenstates are evaluated in a basis set of B-spline functions, as explained in section 2.3.2.

Polytomic molecules. The motion of a set of particles can be decomposed into translation and rotation of the center of mass and vibration of its particles. A $n-$particle system has $3n-5$ vibrational degrees of freedom (vibrational modes) if it is linear and $3n-6$ otherwise [99]. In this work we have investigated

inner shell photoionization of polyatomic AB_n molecules, A being the central atom and B the surrounding atomic centers, symmetrically displaced around A. Recent experimental data [127, 128] clearly indicate that the totally symmetric stretching mode (TSSM) is the most affected by the structural rearrangement that accompanies core ionization. For this reason, we have restricted the motion of the nuclei to this monodimensional coordinate. The dynamics of the surrounding nuclei towards the central atom along the TSSM can be understood in terms of a virtual particle moving in a mono-dimensional well $V(R)$, defined by the n chemical bonds, with a reduced mass[2] $\mu = 3M_B$. Then, equation 2.36, remains valid with $R = |\mathbf{R}_B - \mathbf{R}_A|$, the TSSM coordinate.

2.3.1.1 Potential energy curves

The potential energy curve in which the nuclei move ($E_n(R)$ in eq. 2.36) can be found by solving eq. 2.3 for different values of R. However, the energies provided by the DFT-based method employed to solve eq. 2.3 might not be accurate enough in some situations. In general, *ab initio* multi-reference methods can produce accurate PECs of medium-size systems [93]. In the case of a core-hole species the situation is more complex since one would need to freeze the core in the self-consistent field procedure so inner-valence electrons do not decay, which may result in a poor description of electron correlation. In these situations, the harmonic and the Morse approximations can provide a good alternative for the evaluation of $E_n(R)$.

- **The harmonic oscillator** models an ideal system that when taken away from the equilibrium position R_{eq} experiences a restoring force which is proportional to the extent of the displacement. It allows to write the potential energy as:

$$E(R) = \frac{1}{2} m\omega^2 (R - R_{eq})^2 \tag{2.40}$$

  where m is the mass of the system, ω si the angular frequency and R_{eq} is the equilibrium distance. This simple formula provides an good description of the PEC around the equilibrium geometry, but it cannot describe dissociation since it does not take into account the anharmonicity of the chemical bonds. Consequently, it allows to evaluate low-energy stationary eigenstates with accuracy [84, 86], but it should not be used to describe the high-energy region.

- **The Morse potential** [129] provides a valid description of the PEC in a larger range of internuclear distances in terms of a simple analytical formula that takes into account the anharmonicity of the chemical bonds:

$$V(R) = V(R_e) + D_e \left[1 - e^{\alpha(R - R_{eq})}\right]^2 \tag{2.41}$$

[2] The mass of the central atom (m_A) does not contribute to μ since it remains frozen along the TSSM coordinate.

where R_{eq} is the equilibrium distance, D_e is the dept of the potential energy well and α is a parameter controlling its width. The Morse parameters are related to the usual spectroscopic ones (the oscillator strength, ω_e, and the anharmonicity parameter, $\omega_e x_e$) by the formulas:

$$D_e = \frac{\omega_e^2}{4\omega_e x_e} - \frac{\omega_e x_e}{4} \simeq \frac{\omega_e^2}{4\omega_e x_e} \tag{2.42}$$

$$\alpha = \sqrt{\frac{k_e}{2D_e}} \tag{2.43}$$

Although eq. 2.41 was designed for studying diatomic molecules, it can still provide accurate results for the TSSM of small polyatomics [79, 85, 84, 88].

2.3.2 Evaluation of vibrational eigenstates

Vibrational eigenstates are evaluated by solving the eigenvalue problem given in eq. 2.39 in a basis set of B-splines

$$\zeta(R)_{n\nu} = \sum_{i=1}^{N_{\max}} c_{n\nu i} B_i(R) \tag{2.44}$$

where n and ν are the electronic and vibrational quantum numbers, respectively, and i is an index going over the $N_{\max}$ B-spline functions B_i, which are defined up to a value of $R_{\max}$. The corresponding secular equation in its matrix form, $\mathbf{Hc} = E\mathbf{Sc}$, where $\mathbf{H}$ and $\mathbf{S}$ are the Hamiltonian and the overlap matrices in the B-spline basis set, is the solved using a standard diagonalization procedure. Since B-spline functions are piecewise polynomials, the elements of $\mathbf{H}$ and $\mathbf{S}$ are computed exactly using a Gauss-Legendre integration method.

2.3.2.1 Bound states

The resolution of the secular equation provides an orthonormal set of stationary states. Those whose energy is lower than the molecular dissociation limit constitute the bound part of the spectrum. Of course, the number of bound states and the energy spacing depends on the shape of the potential well (depth and width) and on the reduced mass of the system, but not on the parameters of the B-spline expansion, provided the basis set is good enough.

2.3.2.2 Continuum states

The stationary solutions of the secular equation with energy higher than the dissociation limit constitute a discretized representation of the vibrational continuum with the arbitrary boundary condition $\chi(R_{max}) = 0$. As in the case of the electronic states (section 2.2.2.2), the number of continuum states and their energy spacing depend on the parameters of the numerical expansion and one needs to employ a large value of R_{max} and a dense grid of B-splines so

the asymptotic behavior of the continuum wave functions can be properly described. However, the situation here is more simple since this is a mono-channel scattering problem and the adequate normalization of the true continuum states χ_{E_ν} can be set by multiplying by a factor:

$$\chi_{E_\nu} = \sqrt{\rho(E_\nu)}\chi_\nu \tag{2.45}$$

where is ρ_{E_ν} is the density of states [107], which can be approximated by:

$$\rho(E_\nu) = \left|\frac{\partial E(\nu')}{\partial \nu'}\right|_{\nu'=\nu} \simeq \frac{2}{E_{\nu+1} - E_{\nu-1}} \tag{2.46}$$

2.3.3 Vibrationally resolved cross sections

Let us consider a transition from the ground state $\Phi_{0\nu}(\mathbf{x}, R)$, with $\nu = 0$, to a state $\Phi_{\alpha\varepsilon lh\nu'}(\mathbf{x}, R)$ in which an electron has been emitted from the α molecular orbital with ε kinetic energy and lh symmetry, leaving the residual ion in the $\alpha\nu$ vibronic state. These are Born-Oppenheimer states and can be written as

$$\Phi_{0\nu}(\mathbf{x}, R) = \Psi_0(\mathbf{x}, R)\chi_{0\nu}(R) \tag{2.47}$$

$$\Phi_{\alpha\varepsilon lh\nu'}(\mathbf{x}, R) = \Psi_{\alpha\varepsilon lh}(\mathbf{x}, R)\chi_{\alpha\nu'}(R) \tag{2.48}$$

The corresponding dipole transition matrix element upon interaction with linearly polarized light is given by:

$$\mu_{\boldsymbol{\epsilon}}^{\alpha\varepsilon lh\nu'\leftarrow 0\nu} = \int \langle \Phi_f(\mathbf{x}, R)|\boldsymbol{\mu}_{\boldsymbol{\epsilon}}|\Phi_i(\mathbf{x}, R)\rangle dR \tag{2.49}$$

where $\boldsymbol{\mu}_{\boldsymbol{\epsilon}}$ is the total dipole operator ($\hat{\boldsymbol{\epsilon}}$ is the polarization vector of the field), which is the sum of two contributions:

$$\boldsymbol{\mu}_{\boldsymbol{\epsilon}} = \underbrace{\hat{\boldsymbol{\epsilon}} \sum_n \mathbf{r}_n}_{\boldsymbol{\mu}_{\boldsymbol{\epsilon}}^{\text{elec}}} + \underbrace{\hat{\boldsymbol{\epsilon}} \sum_\alpha Z_\alpha \mathbf{R}_n}_{\boldsymbol{\mu}_{\boldsymbol{\epsilon}}^{\text{nuc}}} \tag{2.50}$$

Inserting eqs. 2.47, 2.48 and 2.50 into eq. 2.49, we have

$$\mu_{\boldsymbol{\epsilon}}^{\alpha\varepsilon lh\nu'\leftarrow 0\nu} = \int \underbrace{\langle \Psi_{\alpha\varepsilon lh}(\mathbf{x}, R)|\boldsymbol{\mu}_{\boldsymbol{\epsilon}}^{\text{elec}}|\Psi_0(\mathbf{x}, R)\rangle}_{\mu_{\boldsymbol{\epsilon}}^{\alpha\varepsilon lh\leftarrow 0}} \chi_{\alpha\nu'}(R)\chi_{0\nu}(R)dR$$
$$+ \int \langle \Psi_{\alpha\varepsilon lh}(\mathbf{x}, R)|\Psi_0(\mathbf{x}, R)\rangle \chi_{\alpha\nu'}(R)\boldsymbol{\mu}_{\boldsymbol{\epsilon}}^{\text{nuc}}\chi_{0\nu}(R)dR$$

where the second term is zero due to the orthogonality of electronic states.

$$\mu_{\boldsymbol{\epsilon}}^{\alpha\varepsilon\nu' lh\leftarrow 0\nu} = \int \mu_{\boldsymbol{\epsilon}}^{\alpha\varepsilon lh\leftarrow 0}\chi_{\alpha\nu'}(R)\chi_{0\nu}(R)dR \tag{2.51}$$

An expression for the photoionization cross section upon interaction with monochromatic light for a given vibronic state is obtained inserting eq. 2.51 into eq. 1.26

and summing incoherently over all photoelectron symmetries (all values of l and h):

$$\sigma_{\boldsymbol{\epsilon}}^{\alpha}(\varepsilon) = \frac{4\pi^2\omega}{\hbar c}\sum_{lh}\left|\int \mu_{\boldsymbol{\epsilon}}^{\alpha\varepsilon lh\leftarrow 0}\chi_{\alpha\nu'}(R)\chi_{0\nu}(R)dR\right|^2 \tag{2.52}$$

where ω is the photon energy, which is related to the photoelectron energy ε through the equation $\varepsilon = \hbar\omega - E_{\alpha}^{\nu\nu'}$, where $E_{\alpha}^{\nu\nu'} = E_{\alpha\nu'} - E_{0\nu}$ is the energy required to produce the ion in the $\alpha\nu'$ vibronic state. For the case of randomly oriented molecules, one can compute $\sigma_{\boldsymbol{\epsilon}}^{\alpha}$ for three orthogonal directions of $\hat{\boldsymbol{\epsilon}}$ and then the results incoherently (eq. 1.27).

Chapter 3

Electron dynamics upon attosecond ionization

The development of attosecond technology has enabled the real-time observation of electron motion in atoms, molecules and solids [10]. Experimentally, it is now possible to generate laser pulses of durations of tens of attoseconds. These durations are of the order of the period of revolution of the first Bohr orbit which is 150 attoseconds, thus opening the way to track and to manipulate electron dynamics at its natural time scale. Due to their wide spectral bandwidth, attosecond pulses create coherent superpositions of electronic states, inducing an ultrafast response in the target. In the case of a molecule, prompt ionization may produce charge migration along the molecular skeleton preceding any nuclear rearrangement [27, 26, 62, 67, 98]. In this chapter we present a method to evaluate the electronic wave packet generated in a molecule upon attosecond ionization and the subsequent charge redistribution, applying some of the concepts that have been previously introduced in chapters 1 and 2.

3.1 Time evolution of the wave function

Attosecond XUV pulses can efficiently ionize molecules from several shells, creating a coherent superpositions of electronic states. In general, the subsequent dynamics can be described in the framework of the fixed nuclei approximation since it usually occurs before the onset of the nuclear motion. Here we have expanded the total wave function into a basis of electronic states that have been computed using the static-exchange DFT method explained in section 2.2.2:

$$\Phi(\mathbf{x}_1, ..., \mathbf{x}_N, t) = c_0(t)\Psi_0(\mathbf{x}_1, ..., \mathbf{x}_N) + \sum_{\alpha lh} \int c_{\alpha\varepsilon lh}(t)\Psi_{\alpha\varepsilon lh}(\mathbf{x}_1, ..., \mathbf{x}_N)d\varepsilon \quad (3.1)$$

where $\Psi_0(\mathbf{x}_1, ..., \mathbf{x}_N)$ is the electronic ground, $\Psi_{\alpha\varepsilon lh}$ represents an continuum state in which an electron has been promoted from the α orbital to a continuum

orbital with kinetic energy ε and angular quantum numbers l and m and the time-dependence of the wave function is included in the spectral coefficients c_0 and $c_{\alpha lh}$ which satisfy the normalization condition:

$$|c_0(t)|^2 + \sum_{\alpha lh} \int |c_{\alpha \varepsilon lh}(t)|^2 d\varepsilon = 1 \tag{3.2}$$

At $t = 0$ the system is assumed to be in the ground state, i.e., $|c_0(0)|^2 = 1$ and $c_{\alpha lh}(\varepsilon, 0) = 0$. If the attosecond pulse is weak, most of the population will remain in the ground state, i.e., $|c_0(t)|^2 \simeq 1$, and the time-dependent coefficients can be evaluated using first-order perturbation theory, as explained in section 1.2. We can thus make use of eq. 1.15 to evaluate the continuum spectral coefficients which, for our particular case, reads:

$$c_{\alpha \varepsilon lh}(t) = -\frac{i}{\hbar} \langle \Psi_{\alpha \varepsilon lh}(\bar{\mathbf{x}}) | \boldsymbol{\mu}_{\boldsymbol{\varepsilon}} | \Psi_0(\bar{\mathbf{x}}) \rangle e^{-\frac{i}{\hbar}(E_\alpha + \varepsilon)t} \int_0^t F(\tau) e^{\frac{i}{\hbar}(E_\alpha + \varepsilon - E_0)\tau} d\tau \tag{3.3}$$

where $\hat{\epsilon}$ is the polarization direction of the electric field E and E_α is the energy of an ion with a hole in the α molecular orbital After the interaction with the pulse ($t > T$), the integral in eq. 3.3 can be substituted by the Fourier transform of the electric field $\mathcal{F}_{\{E\}}$:

$$c_{\alpha \varepsilon lh}(t > T) = -\frac{i}{\hbar} \langle \Psi_{\alpha \varepsilon lh}(\bar{\mathbf{x}}) | \boldsymbol{\mu}_{\boldsymbol{\varepsilon}} | \Psi_0(\bar{\mathbf{x}}) \rangle e^{-\frac{i}{\hbar}(E_\alpha + \varepsilon)t} \mathcal{F}_{\{E\}}\left(\frac{E_\alpha + \varepsilon - E_0}{\hbar} \right) \tag{3.4}$$

where the dependence on time is that of the stationary phases $e^{-\frac{i}{\hbar}(E_\alpha + \varepsilon)t}$ as the wave packet is let evolve freely. The interferences between ionic states which are coherently populated can be imprinted in different observables. In particular, we are interested in the electron density, which can be evaluated using eq. 2.5.

3.2 Electron dynamics in the parent ion

We seek to analyze the evolution of the hole generated in the molecular target upon attosecond ionization. The residual ion is an open system that remains coupled to the emitted electron. Therefore, it can be fully characterized in terms of its reduced density matrix, whose elements can be constructed from the spectral coefficients (eqs. 3.3 and 3.4):

$$\gamma^{(\text{ion})}_{\alpha\alpha'}(t) = \sum_l \int c_{\alpha \varepsilon lh}(t) c^*_{\alpha' \varepsilon lh}(t) d\varepsilon \tag{3.5}$$

The trace of the reduced density matrix contains the population of each ionic state and the off-diagonal terms provide the coherence between pairs of states. In the case of ionization with monochromatic light, all off-diagonal terms would be zero (unless those involving degenerate states) since the parent ion would be in an incoherent superposition of states. This is the situation one would expect

to find, for instance, in a synchrotron radiation experiment where the energy of the incident photons is well defined [36]. Due to their wide spectral bandwidht, attosecond XUV pulses can generate coherent superpositions of electronic states, allowing to investigate ultrafast dynamics with the required time resolution [10].

The reduced density matrix (eq. 3.5) quantity contains all the information about the ionic subsystem and therefore can retrieve any observable depending on its coordinates. In particular, we are interested in the time-dependent electron density, which can be evaluated as:

$$\rho^{(\mathrm{ion})}(\mathbf{r},t) = \rho_0(\mathbf{r}) - \sum_{\substack{\alpha\alpha' \\ \text{same} \\ \text{spin}}} \gamma^{(\mathrm{ion})}_{\alpha\alpha'} \varphi_\alpha(\mathbf{r})\varphi_{\alpha'}(\mathbf{r}) \tag{3.6}$$

where the double sum runs over ionic states from which the electron has been emitted with the same spin, φ_α is the α molecular orbital and ρ_0 is the ground state electron density:

$$\rho_0(\mathbf{r}) = \sum_\alpha \varphi^2_\alpha(\mathbf{r}) \tag{3.7}$$

An interesting observable to evaluate is the density of the hole generated upon ionization, defined by Cederbaum and coworkers [27] as difference between the electron density of the ion and that of the (initial) neutral molecule:

$$Q(\mathbf{r},t) = \rho_0(\mathbf{r}) - \rho^{(\mathrm{ion})}(\mathbf{r},t) = \sum_{\substack{\alpha\alpha' \\ \text{same} \\ \text{spin}}} \gamma^{(\mathrm{ion})}_{\alpha\alpha'}(t) \varphi_\alpha(\mathbf{r})\varphi_{\alpha'}(\mathbf{r}) \tag{3.8}$$

Fluctuations in the hole density might arise along the molecular scheleton if several ionic states are coherently populated, i.e., if there are non-zero elements in the off-diagonals of the reduced density matrix.

Results

Chapter 4

Interferences in molecular photoionization

X-rays can matter from their inner and valence shells, producing short-wavelength electrons that can be diffracted by the surrounding atomic centers. Consequently, scattered photoelectrons convey structural information about the system, which can be extracted by fitting experimental photoelectron spectra to analytical formulas. Based on this principle, the NEXAFS (near-edge X-ray absorption fine structure) and the EXAFS (extended X-ray absorption fine structure) techniques [130, 131] can retrieve structural information of crystals and of bulk amorphous materials [132, 133, 134, 135, 136, 137, 138], where the relatively low intensity of standard X-rays is compensated by the large number of particles in the sample.

However, obtaining structural information of isolated molecules is more difficult because of the low densities of the gas phase. To overcome this difficulty, in addition to the development of the gas-phase EXAFS technique [139, 140, 141], other methods are being explored. One of them takes advantage of the high brightness of the X-ray free electron lasers (XFEL), which can take time-resolved "pictures" through the so-called photoelectron holography [142]. However, its practical applications are still very limited due to the complexity and large dimensions of the recently operating XFEL facilities. A more traditional method consists of measuring molecular-frame photoelectron angular distributions in photoionization with synchrotron radiation [143, 144, 145, 146]. In this direction, recent work on diatomic molecules [147, 78, 79, 80] has shown that even the angle-integrated photoelectron spectra might be a valuable tool for structural determination. Here we present an overview of our most significant results on photoionization of diatomic (CO, F_2) and small polyatomic (BF_3, CF_4) molecules with synchrotron radiation. We show that the interferences arising between different ionization paths may encode structural information that can be extracted by analyzing the role of the nuclear motion. This chapter constitutes only a summary of the work attached in appendices 1-5. This work has

been done in collaboration with Piero Decleva (University of Trieste) and with the experimental groups of Catalin Miron (SOLEIL) Kiyosi Ueda (Spring-8), Edwin Kukk (University of Turku) and Thomas Darrah Tomas (University of Oregon).

4.1 Inner shell photoionization of CO, BF_3 and CF_4: intramolecular scattering

We explore inner-shell photoionization of small molecules, where an electron is ejected from a 1s orbital of a first-row atom. Fig. 4.1 shows the photoelectron spectra of CO, BF_3 and CF_4 taken at photon energies of 425, 518 and 383 eV, respectively, at PLEIADES beamline [148] at SOLEIL Synchrotron. The experimental spectrum of BF_3 and CF_4 (fig. 4.1) shows several vibrational excitation peaks in the the totally-symmetric stretching mode (TSSM), which is the most affected by the electronic rearrangement accompanying core ionization [127, 128]. Potential energy curves of the electronic ground state and of the core-hole species generated upon C 1s and B 1s ionization of CO, CF_4 and BF_3, repectively, are shown in fig. 4.2, as well as the relevant vibrational eigenfunctions. Photoionization of CO and BF_3 leads to a large progression of vibrational levels as a consequence of the favorable Franck-Condon (FC) overlap between the initial and several final-state vibrational wave functions due to the large bond contraction accompanying core-ionization ($\Delta R_{\mathrm{BF}} = -0.110$ a.u. [127]). They have been evaluated using the harmonic (CF_4) Morse (CO, BF_3) and approximations from reliable spectroscopic parameters available in the literature [REFS]. The progression is limited to only two vibrational levels in the spectrum of CF_4 because the potential energy curves of the neutral and the ionic species (fig. 4.2) are very similar in the region close to the equilibrium geometry ($\Delta R_{\mathrm{CF}} = -0.0115$ a.u. [128]). The spectrum of CO shows an intermediate situation: 4 vibrational excitations in the only vibrational mode of the parent ion ($\Delta R_{\mathrm{CO}} = -0.0932$ a.u. [149], see fig. 4.2a).

Fig. 4.3 shows the total (upper panels) and the vibrationally resolved (lower panels) C 1s and B 1s photoionization cross sections of CO, CF_4 and BF_3, respectively, as a function of the photon energy. They have been calculated as explained in section 2.3.3 using the static-exchange DFT method and in the case of BF_3 and CF_4 the nuclear motion has been restricted to the TSSM coordinate. Total cross sections are obtained by summing over all vibrational contributions. In good agreement with the spectra shown in fig. 4.1, we observe a large progression of vibrational excitations upon B 1s ionization of BF_3 reaching up to $\nu' = 8$, $\nu' = 2$ and $\nu' = 3$ being the dominant contributions in the entire energy range. Only the low-lying vibrational eigenstates or the parent ion are excited in C 1s ionization of CO and CF_4, as experimentally found.

In all cases, we can distinguish that the total photoionization cross sections (upper panels in fig. 4.3) exhibit sharp increases near the ionization threshold due to the presence of shape resonances [150, 151, 152]. The origin of these

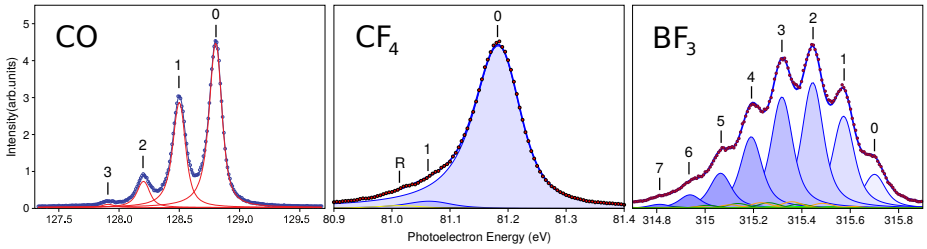

Figure 4.1: Photoelectron spectra of CO (left), BF_3 (center) and CF_4 (right) taken SOLEIL at $h\nu = 425$, 518 and 383 eV, respectively. Experimental results: circles. Thick blue line: fit of the experimental data. Thin blue lines enclosing shaded areas: vibrational progression associated with the symmetric stretching mode. Other thin lines: contribution of other modes resulting from recoil. Peak labels indicate the vibrational quantum number ν in the BF_3^+ symmetric stretching mode.

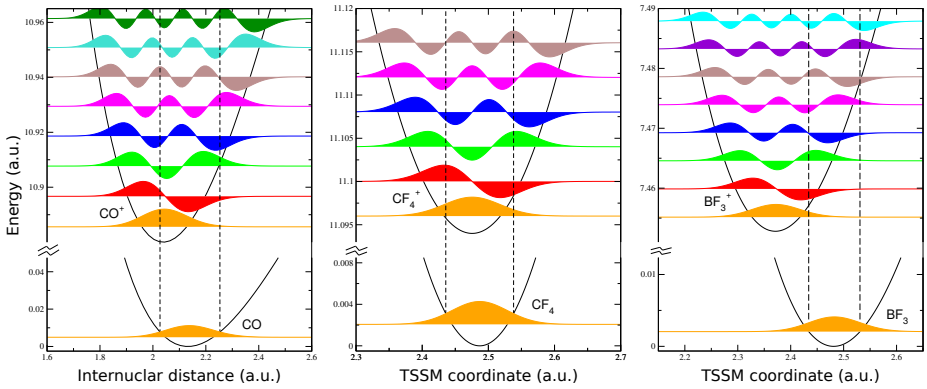

Figure 4.2: Potential energy curves of the electronic ground state of CO (left), BF_3 (center) and CF_4 (right) and of the core-hole species generated upon 1s from C (CO and CF_4) and B (BF_3) along the internuclear distance (CO) and TSSM coordinate (BF_3 and CF_4). They have been constructed using reliable spectroscopic parameters available in the literature [REFS]. The relevant vibrational eigenstates are shown: the ground state of the neutral molecule (orange) and the low-lying states of the core-hole species (different colors), as well as the FC region (dashed black lines).

structures can be understood in terms of a quasi-bound state embedded in the electronic continuum as a consequence to the existence of a small barrier in the molecular potential. More subtle structures arise higher energies due to photoelectron diffraction by the surrounding atomic centers (O in CO, F in BF_3 and CF_4). However, the rapid decrease of the cross sections with the photon energy usually washes out scattering effects in the high-energy region. A better analysis can be performed by taking ratios between vibrationally resolved cross

sections ($\nu-$ratios), since the decay is same for each vibrational component. Experimentally, presenting the cross sections as $\nu-$ratios is advantageous since certain calibration problems that one would face in case of absolute cross section can be avoided.

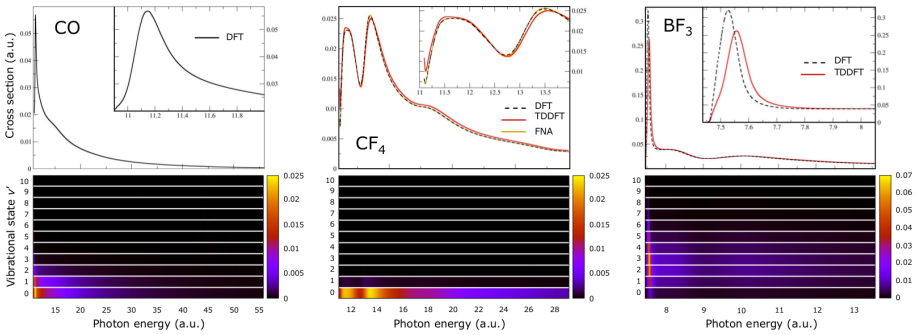

Figure 4.3: Total (upper panels) and vibrationally resolved (lower panels) cross section of CO (left) and, in the TSSM, of B 1s photoionization of BF_3 (center) and of C 1s photoionization of CF_4 (right). The insets in the upper panels show a blow up of the low energy region.

Fig. 4.4 shows the experimental and theoretical $\nu-$ratios a function of the photoelectron momentum. For the three systems, the $\nu-$ratios are taking using the largest contribution as a reference, which is $\nu' = 0$ for CO and CF_4 and $\nu' = 2$ for BF_3. The shape resonances appear now as even sharper structures close to the ionization threshold. At higher energies, the $\nu-$ratios exhibit pronounced oscillations superimposed to a nearly flat background which are a consequence of intramolecular scattering. The periodicity of the oscillations is $2k_eR$, where k_e is the photoelectron momentum and R the distance between emitting and diffracting atoms, as in the well known EXAFS equation [153]. Our interpretation in terms of intramolecular scattering is supported by the good agreement with a first Born model [79] (see appendices 1 and 2).

The agreement between theory and experiment is very good in all cases. The excellent agreement between the results provided by the static-exchange and the time-dependent DFT methods indicates that interchannel coupling does not play an important role in core-ionization and that therefore one can rely on the former to interpret the experimental findings. In the case of BF_3, the overall shape of the $\nu-$ratios is very similar for all $\nu \geq 3$; for $\nu' = 0$ and $\nu' = 1$, the oscillations are essentially identical but appear inverted. The reason is that all vibrational contributions are referred to $\nu' = 2$. If we choose $\nu' = 4$ instead, then the first four $\nu-$ratios would be inverted. The same behavior is observed in CO and CF_4. These results suggest that, for a given molecule, all $\nu-$ratios carry the same structural information. In fact, as discuss in appendices 1 and 2, the information contained in each individual $\nu-$ratio can be gathered into a generalized $\nu-$ratio. In the case of BF_3, where the vibrational progression

reaches up to $\nu' = 7$, the use of a generalized $\nu-$ratio is very useful since it improves dramatically the statistical significance of the experimental data.

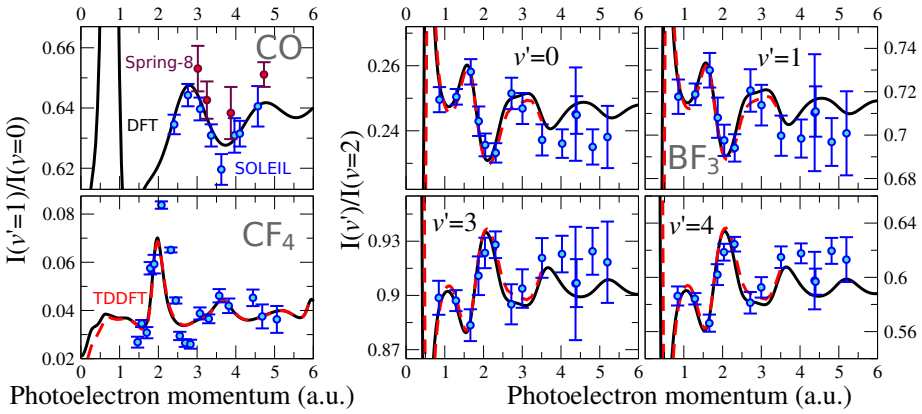

Figure 4.4: Ratios between inner-shell vibrationally resolved photoionization cross sections of CO (upper left), CF_4 (lower left) and BF_3 (right), shown in fig. 4.3 Circles with error bars: experimental data including statistical errors taken at SOLEIL and Spring-8. Black dashed lines: results from the static-exchange DFT calculations. Red full lines: results of the TDDFT calculations (BF_3 and CF_4). Horizontal dashed-dotted lines: ratios predicted by the FC approximation.

Extracting structural information

As the oscillatory patterns found in the $\nu-$ratios are due to intramolecular scattering, they convey structural information about the system. In appendix 4, we present a systematical approach for extracting this information and, as a proof of principle, we apply it to the simultaneous determination of the internuclear distance of CO ($R = R_{CO}$) and the bond contraction ($\Delta R = R_{CO^+} - R_{CO}$) upon C 1s ionization. Fig. 4.5 illustrates of how the $\nu-$ratio $I(\nu' = 1)/I(\nu' = 0)$ changes when R and ΔR are modified independently. As the bond contraction sets the overlap between the initial and the final vibrational wave functions, the $\nu-$ratios are shifted vertically when varying ΔR (fig 4.5a). This effect is very sensitive because the FC overlap is strongly affected by small modifications of ΔR, as can be seen in fig. 4.2. When R is modified (fig. 4.5b), the periodicity of the high-energy oscillations changes because they are due to intramolecular scattering and therefore depend on the distance between the emitting and diffracting centers.

We have performed a χ-square minimization procedure in order to find the values of R and ΔR that provide a theoretical ν-ratio that is in best agreement with the experimental points measured at SOLEIL and Spring-8 synchrotrons (fig. 4.6a). These values are $R = 2.09 \pm 0.03$ a.u and $\Delta R = -0.0945 \pm 0.00014$ a.u. Details of the fitting procedure can be found in appendix 4. The $\nu-$ratios

computed using these values and those taken from the literature [149, **?**, **?**]: $R_{\text{lit}} = 2.1322$ a.u. and $\Delta R_{\text{lit}} = -0.0932$ a.u. are shown in figure 4.6b as well as the experimental points. We note that the literature values lay inside the confidence intervals provided by the method. The χ-square function of the fit is shown in 4.6b as a function of R and ΔR, as well as the and the isocurves that determine the bidimensional confidence regions for different confidence levels. Due to the lack of local minima in the χ-square function, we note that the fitting procedure always converges to the same values, regardless the initial guess.

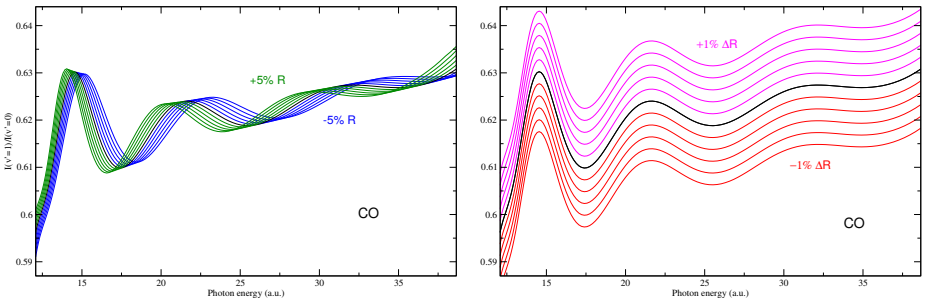

Figure 4.5: Vibrational branching ratio $\nu-$ratio $I(\nu'=1)/I(\nu'=0)$ corresponding to C 1s photoionization of CO, calculated using the bibliographic values of R and ΔR as in fig. 4.4 (both panels: black lines), increasing and decreasing ΔR in steps of 0.2% (left pannel: pink and red lines), and increasing and decreasing R in steps of 1% (right pannel: green and blue lines).

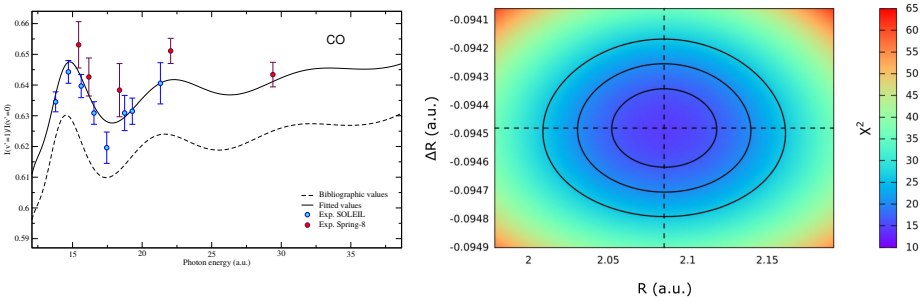

Figure 4.6: a) vibrational branching ratio $\nu' = 1$ versus $\nu' = 0$: experimental values from Spring-8 (red points) and from SOLEIL (blue points), theoretical values using the bibliographic values taken from [149, **?**, **?**] and the ones that minimize χ-square with the experimental points (straight line). b) χ^2 function as a function of R and ΔR. The black lines correspond to the limits of the confidence regions for confidence levels: 68.3% (1σ), 95.4% (2σ) and 99.7% (3σ).

4.2 Photoionization of F_2: multicenter emission

Young's double slit interferences are expected to arise when an electronic wave is coherently emitted from two (several) atomic centers. As found by Cohen and Fano in the sixties [154], these interferences are imprinted in the angle-integrated photoelectron spectra of homonuclear diatomic molecules. Over the last years, this phenomenon has attracted the interest of various authors [155, 147, 156, 157, 78, 83, 80]. We have investigated it in the fluorine molecule by analyzing dissociative and non-dissociative ionization from inner and valence shells. Here we present a brief summary of our work, which is explained in detail in Appendix 5.

Fig. 4.7 shows some $\nu-$ratios corresponding to ionization from the $3\sigma_g$ orbital as a function of the photoelectron momentum. We have chosen $\nu' = 7$ as the common denominator because it constitutes the largest contribution to the total cross section. As in fig. 4.4, the $\nu-$ratios show pronounced oscillations around the FC value as a function of the photoelectron momentum. However, in this case they are not due to photoelectron diffraction but to multicenter emission as the electron is ejected from an orbital which is delocalized between the two fluorine atoms. In order to confirm this assumption, we have extended formula developed by Cohen and Fano in the sixties [154] to account for the vibrational motion, as is [78]. The results of the model are included in fig. 4.7, where we can see that the agreement with the static-exchange theory is very good. As discussed in Appendix 5, the agreement is not so good in the case of $1\pi_g$ and $1\pi_u$ ionization because π orbitals concentrate most of the electron density outside the molecular axis. However, even in those situations, the amplitudes and periodicities of the oscillations predicted by the Cohen-Fano formula are close to the ones provided by the static-exchange DFT theory. Only the phases are not properly described.

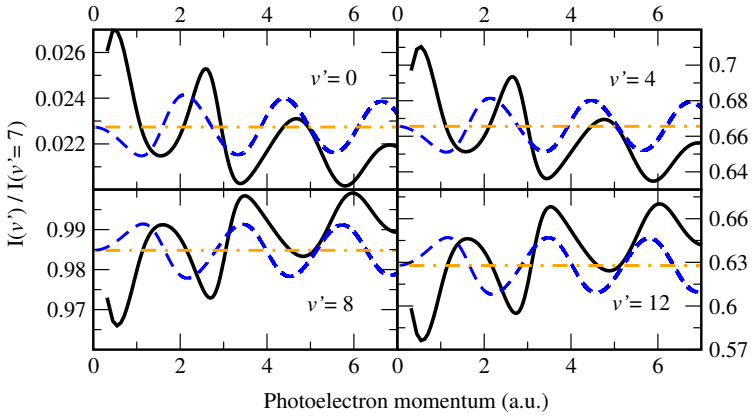

Figure 4.7: Ratios between vibrationally resolved $3\sigma_g$ photoionization cross sections photoionization of F_2. Black line: DFT theory; blue dashed line: Cohen-Fano model; orange dashed line: FC values.

4.3 Conclusions

In summary, we have found measurable evidence of intramolecular scattering and multicenter emission occurring in the photoionization of small molecules at high photoelectron energies. The details of the work presented here can be found in appendices $1-5$. When an electron is emitted from a localized part of a molecule, such as the C 1s (B 1s) orbital in CO or CF_4 (BF_3), effects due to photoelectron diffraction are expected to arise, whereas in the case of ionization from a delocalized orbital, such as those in F_2, one should expect to see Cohen-Fano-like interferences.

Vibrationally resolved photoelectron spectroscopy allows to detect these high-energy interferences in an elegant and consistent way, because (i) the problem of the rapid decrease of the ionization probability with photon energy can be avoided by monitoring the ratios between vibrationally resolved cross sections, and (ii) the effect of the interferences manifest differently in different final vibrational states. The combination of state-of-the-art DFT-like calculations and high-resolution third-generation synchrotron facilities has enabled to explore these non-Franck-Condon effects both theoretically and experimentally, demonstrating that the nuclear response to intramolecular electron diffraction / multicenter emission is observable and can be used to obtain structural information of both, the neutral molecule and the parent ion generated upon ionization.

Chapter 5

Ultrafast electron dynamics in aminoacids

Intramolecular charge transfer is the trigger of important chemical and biological processes, such as photosynthesis [158], cellular respiration [159] or DNA damage [160]. The study of charge transfer within isolated complex molecules was pioneered by Weinkauf and coworkers in the 90s [161, 31, 32]. They were able to track the motion of a positive hole through up to 12 sigma bonds of a tetrapeptide by removing and electron from a chromophore group in the C terminal and analyzing light absorption shifts. However, the time resolution in their experiments was limited by the duration of the pulses they employed, around 200 ns. A decade later [162], by using femtosecond pulses, they were able to measure how long it took for a positive charge to move from the phenyl to the amino group in the PENNA molecule: (80 ± 20) fs. Because of the timescale of the measured dynamics, the suggested that it occurred as a consequence of a transfer between electronic states mediated by the nuclear motion through a conical intersection. Motivated by this pioneering work [161, 31, 32], L. S. Cederbaum and coworkers demonstrated at the end of the 90s that electron correlation can drive ultrafast charge dynamics in a time scale that is faster than the onset of the nuclear motion [27]. This phenomenon has been referenced to as charge migration to distinguish it from charge transfer mediated by nuclear motion and, over the last two decades, it has been widely investigated in a large number of molecules of biological interest [26, 27, 28, 29, 30, 58, 59].

The application of attosecond technology to the study of complex molecules has lead to the experimental demonstration of charge migration in a biomolecule: the amino acid phenylalanine [57, 60]. The $\alpha-$amino acids consist of a central carbon atom (α carbon) linked to an amino ($-NH_2$) group, a carboxyl group ($-COOH$), a hydrogen atom, and a side chain (R), which in the case of phenylalanine is a benzyl group. A two-color pump-probe technique was used in the experiment. Charge dynamics were initiated by isolated XUV sub-300-as pulses, with photon energy in the spectral range between 15 and 35 eV and probed by

4-fs, waveform-controlled visible/near infrared (VIS/NIR, central photon energy of 1.77 eV) pulses (see appendix 6). Ionization induced by the attosecond pulse occurred in a sufficiently short time interval to exclude substantial electron rearrangement during the excitation process. The yield for the production of doubly charged immonium ions was measured as a function of the time delay between the attosecond pump pulse and the VIS/NIR probe pulse. Figure 5.1a shows the results on a 100-fs time scale. The experimental data display a rise time of (10 ± 2) fs and an exponential decay with time constant of (25 ± 2) fs (this longer relaxation time constant is in agreement with earlier experimental results reported in [25]). Figure 5.1b shows a 25-fs-wide zoom of the pump-probe dynamics, obtained by reducing the delay step between pump and probe pulses from 3 to 0.5 fs. An oscillation of the dication yield is clearly visible. For a better visualization, figure 5.1c shows the same yield after subtraction of an exponential fitting curve. The data have been fitted with a sinusoidal function of frequency 0.234 PHz (corresponding to an oscillation period of 4.3 fs), with lower and upper confidence bounds of 0.229 and 0.238 PHz, respectively (see supplementary materials). The ultrafast oscillations in the temporal evolution of the dication yield cannot be related to nuclear dynamics, which usually come into play on a longer temporal scale, ultimately leading to charge localization in a particular molecular fragment. Therefore, these measurements constitute the first experimental observation of purely electron dynamics in a biomolecule.

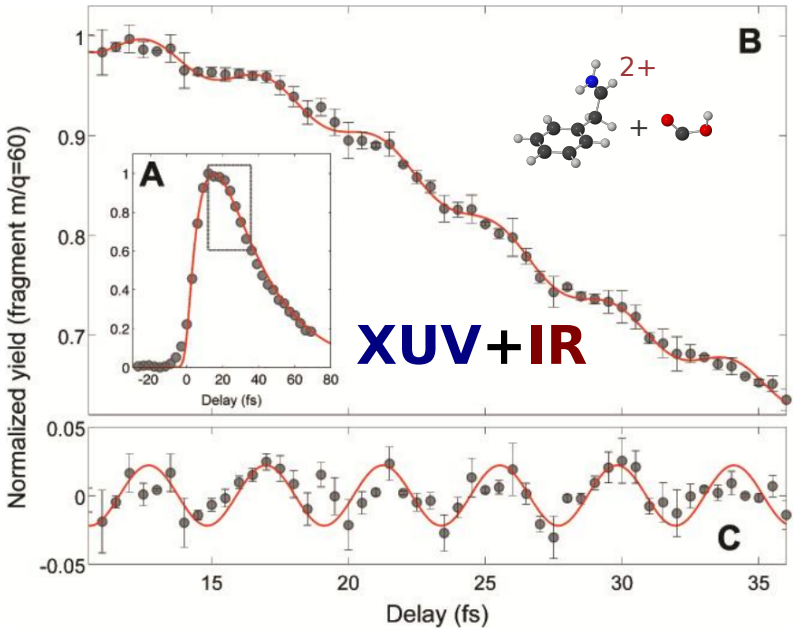

Figure 5.1: Experimental data from the group of Mauro Nisoli. (A) Yield of doubly charged immonium ion (mass/charge = 60) as a function of pump-probe delay, measured with 3-fs temporal steps. The red line is a fitting curve with an exponential rise time of 10 fs and an exponential relaxation time of 25 fs. (B) Yield of doubly charged immonium ion versus pump-probe delay measured with 0.5-fs temporal steps, within the temporal window shown as dotted box in (A). Error bars show the standard error of the results of four measurements. The red line is the fitting curve given by the sum of the fitting curve shown in (A) and a sinusoidal function of frequency 0.234 PHz (4.3-fs period). (C) Difference between the experimental data and the exponential fitting curve displayed in (A). Red curve is a sinusoidal function of frequency 0.234 PHz

In order to confirm that the observed oscillations are not related to any nuclear dynamics, we have calculated the vibrational frequencies and the corresponding periods of phenylalanine using Density Functional Theory (DFT) and the B3LYP functional [163, 164] in a 6−311+g(3df,2p) basis set, implemented in the quantum chemistry package Gaussian09 [165]. The results are given in table 5.3. Our calculations show that the highest vibrational frequency is 0.11 PHz, which corresponds to a period of 9 fs, associated with X-H stretching modes, whereas skeleton vibrations are even slower, so that one can rule out that the observed beatings are due to vibrational motion. In any case, some influence of the nuclear motion cannot be completely excluded, because, for example, stretching of the order of a few picometers of carbon bonds can occur in a few femtoseconds, and this could modify the charge dynamics [166, 65].

We aim to describe the oscillations found in the experiment, explain its origin

and determine the response of other biological molecules. Figure 5.2 shows an energy-level diagram with the electronic states of singly charged phenylalanine (phe^{+}) accessible by the XUV pulse, all the states of doubly-charged phenylalanine (phe^{++}) and those for the system doubly-charged immonium + carboxyl. The energies of the latter two systems have been evaluated within the static-exchange approximation, which is accurate enough to provide a qualitative picture of the full process. As can be seen, one can go from a highly excited state of phe^{+} to the lowest states of the phe^{++} or the dissociated system by absorbing just a few VIS/NIR photons (photon energy around 1.77 eV). Of course, one cannot know how likely this transition will be, but one can unambiguously say that the process only requires absorption of very few VIS/NIR photons. Even if these transitions were unlikely, e.g., due to unfavorable overlap between initial and final orbitals, the transition should be much more likely than others involving many photons even with favorable overlap. Since HOMO orbital of phenylalanine is substantially localized on the amino group, one would expect that ionization by the VIS/NIR pulse is more likely to occur this site and therefore be sensitive to charge localization on the amino group.

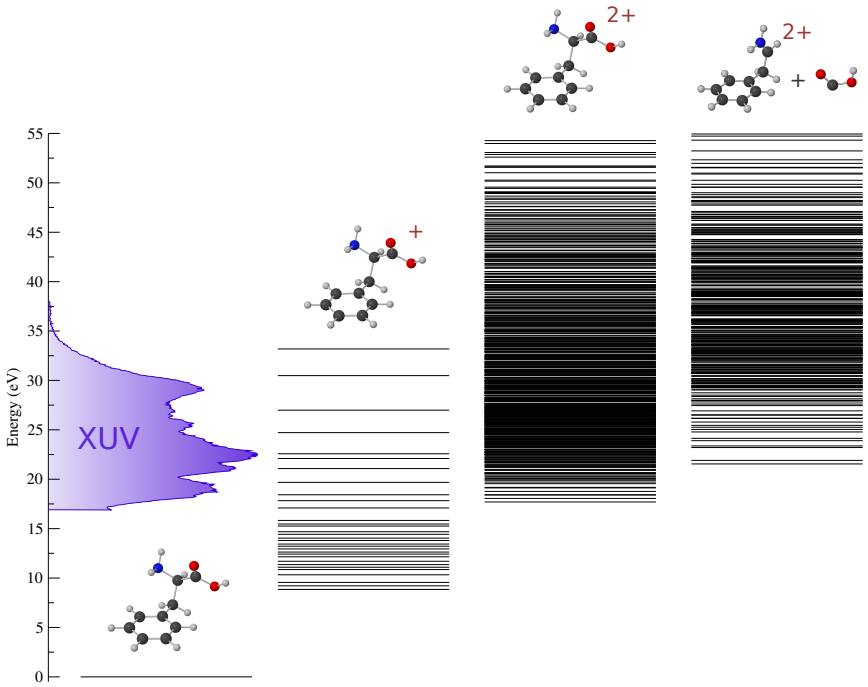

Figure 5.2: Energy level diagram containing all the states of singly charged phenylalanine populated by the XUV pulse, whose energy distribution is included as a shadowed area in the axis bar, all the states of doubly-charged phenylalanine and those for the system doubly-charged immonium + neutral carboxyl.

In order to understand better the origin of the ultrafast oscillations found in the experiment, we have evaluated the electronic wave packet generated upon ionization by an attosecond pulse similar to that used in the experiment and the subsequent evolution of the electron density in phenylalanine. We aim to understand the influence of the different radicals in the amino acids, we have performed a systematical study including glycine and tryptophan. For the evaluation of the ionization amplitudes and the wave packet dynamics make use of the static-exchange DFT method within the formalism of first-order time-dependent perturbation theory, as explained in chapter 3. The geometries of the most the stable conformers [167, 168, 169] are shown in figure 5.4. This chapter is organized as follows: first, we give the details about the evaluation of the electronic stationary states and show the relevant molecular orbitals of the three amino acids (section 5.1) and the corresponding photoionization cross sections (section 5.2); then we show the evolution of the hole generated by an attosecond pulse similar to that used in the experiment (section 5.3), presenting the results of a Fourier analysis over different parts of the molecule, comparing our results with those coming from experimental and previous theoretical work, when available. We conclude by analyzing the effect of molecular conformation and present the results for the evolution of the all-electron system.

Mode	Freq. (PHz)	Period (fs)	Mode	Freq. (PHz)	Period (fs)	Mode	Freq. (PHz)	Period (fs)
1	0.0011	894.84	22	0.0256	39.00	43	0.0410	24.37
2	0.0013	740.75	23	0.0260	38.46	44	0.0413	24.21
3	0.0020	499.23	24	0.0266	37.66	45	0.0421	23.77
4	0.0031	319.91	25	0.0276	36.17	46	0.0446	22.43
5	0.0057	174.18	26	0.0283	35.27	47	0.0446	22.42
6	0.0069	145.31	27	0.0299	33.46	48	0.0459	21.79
7	0.0074	134.46	28	0.0300	33.32	49	0.0486	20.57
8	0.0088	113.87	29	0.0302	33.08	50	0.0493	20.30
9	0.0114	88.00	30	0.0304	32.89	51	0.0500	19.99
10	0.0123	81.60	31	0.0315	31.72	52	0.0544	18.40
11	0.0125	79.76	32	0.0331	30.18	53	0.0907	11.03
12	0.0146	68.41	33	0.0335	29.82	54	0.0916	10.92
13	0.0148	67.63	34	0.0342	29.22	55	0.0929	10.77
14	0.0170	58.95	35	0.0353	28.33	56	0.0946	10.57
15	0.0181	55.17	36	0.0355	28.17	57	0.0947	10.56
16	0.0191	52.48	37	0.0362	27.63	58	0.0950	10.52
17	0.0193	51.71	38	0.0365	27.37	59	0.0952	10.50
18	0.0214	46.68	39	0.0373	26.82	60	0.0956	10.47
19	0.0220	45.45	40	0.0388	25.80	61	0.1050	9.53
20	0.0232	43.13	41	0.0399	25.07	62	0.1070	9.34
21	0.0234	42.75	42	0.0403	24.83	63	0.1125	8.89

Figure 5.3: Vibrational frequencies of phenylalanine. Frequency (PHz) and corresponding periods (fs) of vibrational modes of phenylalanine.

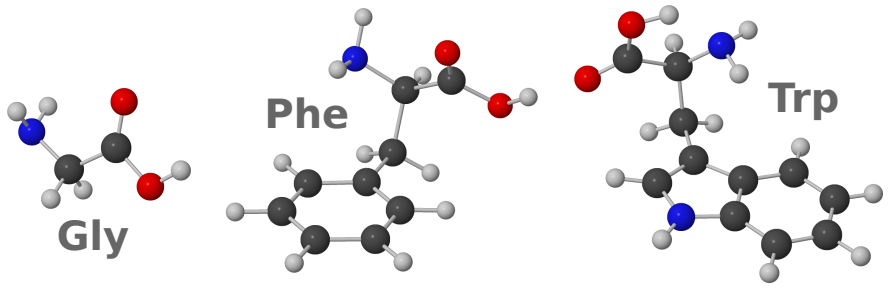

Figure 5.4: Geometry of the most abundant conformers of glycine [167], phenylalanine [168]and tryptophan [169] at 430 K, the temperature of the pump-probe experiment in fig. 5.1.

5.1 Evaluation of electronic states

We employ Slater determinants to represent electronic stationary states, as explained in section 2.2. The corresponding bound (Kohn-Sham) and continuum orbitals have been evaluated in a basis set of B-splines and spherical harmonics. In particular, we used a large one-center expansion (OCE) of 120 B-spline functions enclosed in a sphere of 30 a.u. with origin in the center of mass, using spherical harmonics up to $l = 20$ (see eq. 2.14). The OCE was complemented with small off centers, one on each atom, with sizes varying from 0.2 to 1.6 a.u., larger for the heavier nuclei. The angular expansion in each off-center was limited up to $l = 2$. The LB94 [120] functional was employed to account for electronic exchange and correlation effects. An initial guess for the electronic density of the three amino acids was generated with the Amsterdam Density Functional (ADF) package [116, 117, 118] using a double ζ-polarization plus (DZP) basis set in the case of glycine and a triple ζ-polarization plus (TZP) [99] for phenylalanine and tryptophan. Since it is well known that the LB94 functional overestimates the molecular orbital eigenvalues, the first ionization potential of glycine was calculated by means of the outer-valence Green's function (OVGF) [170] method implemented in Gaussian09 [165], which can provide accurate values of the ionization potentials of the outer-valence shells. Then, the DFT/LB94 eigenvalues were shifted according to the energy difference between the first IP provided by the OVGF and the DFT/LB94 calculations. In order to obtain reliable values of the ionization energies of phenylalanine and tryptophan, we have employed the VWN [119] local density approximation functional within the Slater transition state procedure [171] using ADF with a TZP basis set. The molecular geometries where optimized at the DFT/B3LYP [163, 164] level in a 6311+g(3df,2p) basis set (6-31+g(d) in the case of tryptophan) using Gaussian09 [165], from the optimized geometries reported in [167, 168, 169].

Figs. 5.8, 5.9 and 5.10 show the occupied Kohn-Sham orbitals of the ground state of glycine, phenylalanine and tryptophan, respectively, which were used to evaluate the corresponding wave functions according to equations 2.12 and

2.13. Glycine has planar symmetry and therefore belongs to the C_s point group and its orbitals have either a' or a'' symmetry. As can be seen in fig. 5.5, a' orbitals are symmetric with respect to reflection thought the mirror plane and a'' orbitals are antisymmetric and thus contain a nodal plane. Phenylalanine and tryptophan belong to the C_1 point group because they are not invariant under any symmetry transformation except for the identity operation E and therefore all their orbitals have A symmetry.

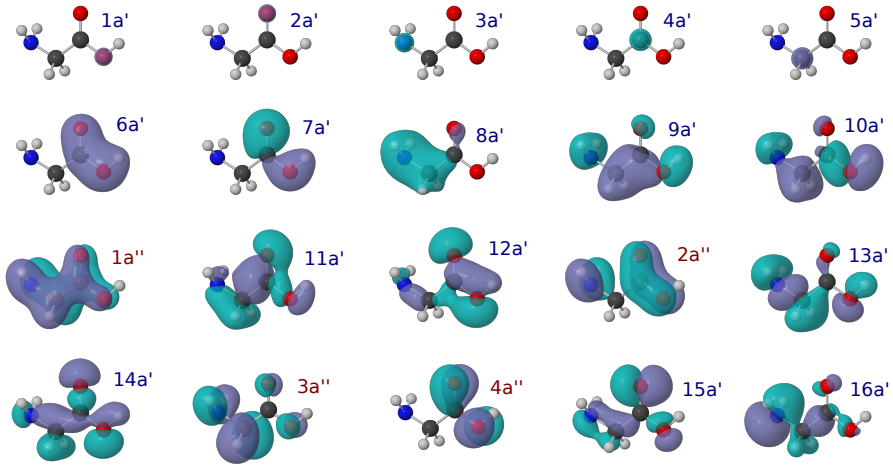

Figure 5.5: Occupied Kohn-Sham orbitals of the glycine molecule. They have been calculated using the LB94 [120] functional in a basis set of B-spline functions as explained in the text.

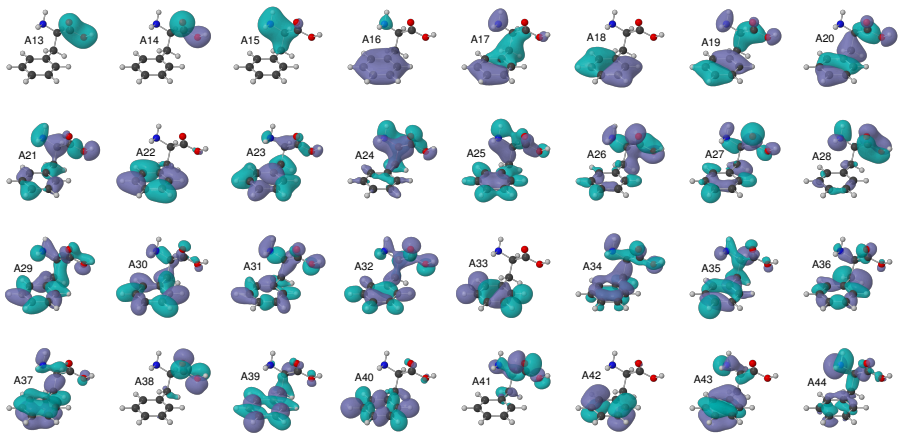

Figure 5.6: Same as fig. 5.5 for the phenylalanine molecule.

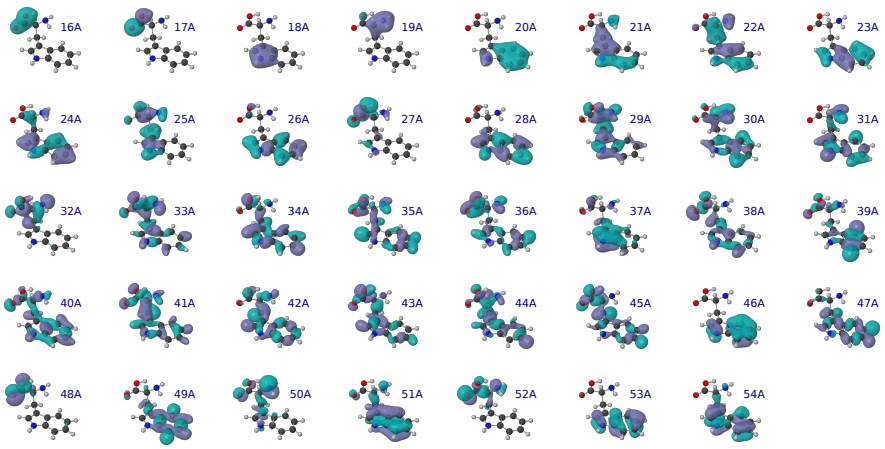

Figure 5.7: Same as fig. 5.5 for the tryptophan molecule.

Neutral glycine, phenylalanine and tryptophan have 40, 88 and 108 electrons, respectively. Therefore, the corresponding electronic ground states are closed-shell systems that can be accurately described using 20, 44 and 54 molecular orbitals in each case. Core orbitals are those constituted by the 1s orbitals of the "heavy" atoms (C, N and O). The energy required to remove an electron from a core orbital in these molecules ranges from around 290 eV in the case of C 1s, to 400 eV for N 1s and 535 eV for O 1s. They are thus not accessible with usual attosecond pulses generated via HHG.On the contrary, valence orbitals, with ionization potentials ranging from around 10 eV to 20 eV, are the easiest to ionize and usually highly delocalized. Whereas a core-hole is very localized hole around a given atom, valence-holes shells are highly delocalized. Inner-valence orbitals present an intermediate situation.

5.2 Photoionization cross sections

We have evaluated photoionization cross sections of glycine, phenylalanine and tryptophan from all valence and inner-valence shells in the framework of the fixed nuclei approximation (FNA), as explained in 1.3. The results are shown if figs. 5.8, 5.9 and 5.10 in the energy range accessible by the attosecond XUV pulse used in the experiment that produced the results shown in fig. 5.1. The energy spectrum of the pulse is represented in the figures by a thick orange curve lying over a shaded area. As expected, we can see a general decay of the cross sections with the photon energy. In some ionic channels we can see sharp structures near the threshold that can be understood in terms of shape resonances [150, 151, 152] due to the existence of small barriers in the complex molecular potentials. Unfortunately, the use of a single excitation approach prevents us from observing any possible signature coming from multiple (doubly, triply) excited electronic states of the molecule embedded in the ionization continuum.

From the figures, it is clear that the three molecules will be efficiently ionized from all valence and inner-valence shells upon interaction with the attosecond pulse. Only core electrons will remain unaffected. Since the contribution from most open channels is comparable, the hole created in the electronic structure of the amino acids upon ionization will be completely delocalized. In this scenario, one would expect that the interferences arising between the coherently populated states induce charge dynamics along the molecular skeleton, similar to that found in previous theoretical work [27, 58, 26, 59, 62, 98]. This is analyzed in detail in section 5.3.

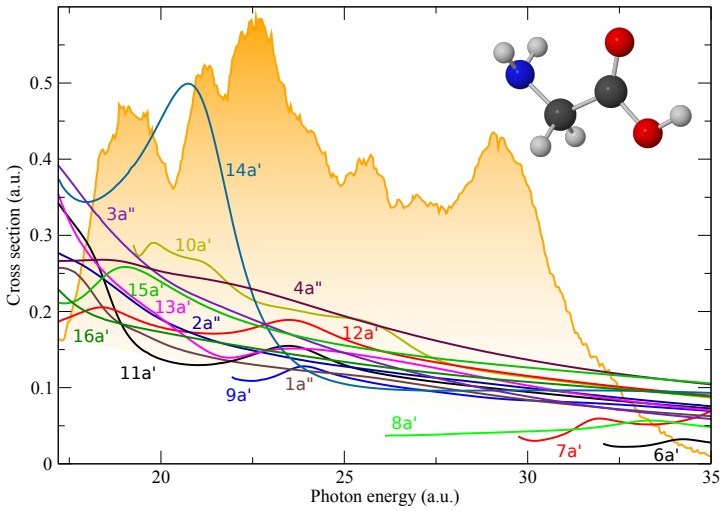

Figure 5.8: Photoionization cross sections of glycine from different molecular orbitals calculated using the static-exchange DFT method. Numbers and colors denote the molecular orbitals from where the electron is emitted in each case (see 5.5). The energy spectrum of the attosecond pulse used as a pump in the experimental results shown in 5.1 is represented by a thick orange curve lying over a shaded area.

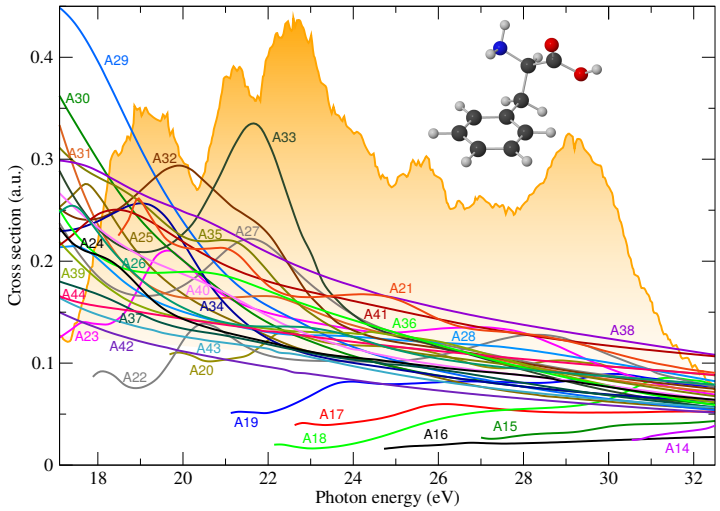

Figure 5.9: Same as fig. 5.8 for the phenylalanine molecule (the corresponding molecular orbitals are shown in 5.6).

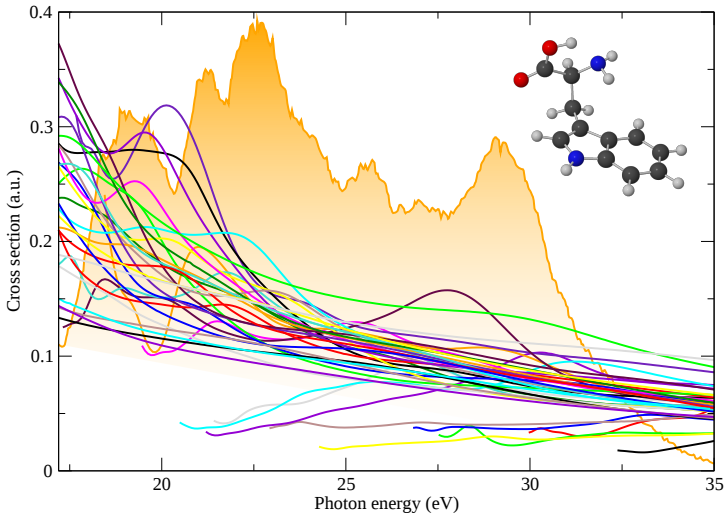

Figure 5.10: Same as fig. 5.8 for the tryptophan molecule (the corresponding molecular orbitals are shown in 5.7).

Comparison with experimental photoelectron spectra

In order to test the validity of our description of the ionization process, we have calculated the photoelectron spectra of phenylalanine for photon energies of 21.2 and 45 eV using the cross section values at those energies (shown in fig.

5.9) and the corresponding ionization potentials. Then, we have compared our results with synchrotron [172] and He(I) [173, 174] radiation spectra available in the literature. For the comparison with the experiments, we have convoluted our infinitely resolved lines with a Lorentzian function of 0.3−eV width at half maximum to account for the vibrational broadening and experimental energy resolution, which is rather limited in these and earlier experiments (the experiments cannot resolve the individual peaks). The comparison between theory and experiment is shown in fig. 5.11. As can be seen, the agreement is reasonably good. We notice however that the experiment of Plekan *et al.* [172] was performed at a photon energy of 100 eV, which is substantially higher than ours. The other two earlier experiments [173, 174] were performed at a photon energy of 21.2 eV. Our results are in better agreement with the most recent experiment, especially for binding energies below 15 eV. This energy range includes the most relevant states in the ultrafast charge dynamics that is initiated in the molecule by an attosecond pulse similar to that represented in fig. 5.9, as we show in section 5.3. The photoelectron spectra are expected to be more sensitive to the choice of photon energy as we approach the threshold. The reason is that the ionization amplitudes can strongly vary with photon energy for values below $25 - 30$ eV, while the variation becomes smother for larger values, as can be seen in fig. 5.9. This is most likely the reason to find a better agreement between the high-energy spectra.

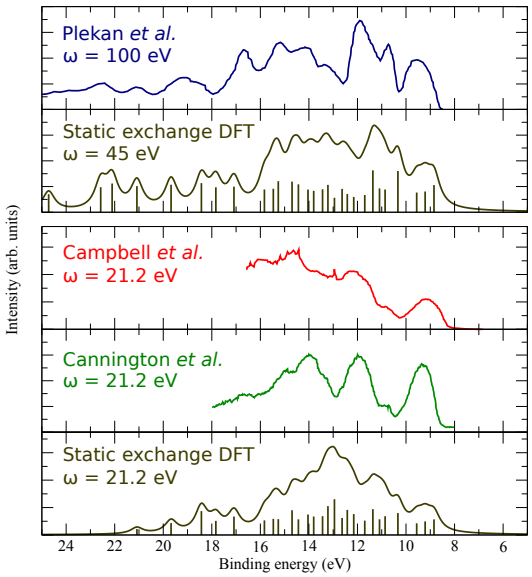

Figure 5.11: Comparison between calculated and experimental [172, 173, 174] photoelectron spectra of phenylalanine.

5.3 Ultrafast electron dynamics initiated by attosecond pulses

The first theoretical predictions of the possibility of observing ultrafast charge migration upon prompt ionization of an organic molecule can be attributed to L. Cederbaum and collaborators [27]. In that work, an electronic wave packet is generated by sudden electron removal from a Hartree Fock (HF) molecular orbital of the difluoropropadienone molecule. Then, the hole generated in the electronic structure moves though the molecular skeleton because the prepared state is not a stationary state of the ionic Hamiltonian but a linear combination of several. Over the last years, they have been able to investigate charge migration in a large number of biological molecules (refs). Here we consider a different scenario: (i) we are using an ultrashort pulse with a broad energy bandwidth to create an electronic wave packet in the parent ion, and (ii) we compute the scattering states to obtain the actual photoionization amplitudes. In order to verify the validity of our time-propagation method, we have performed calculations in order to compare our results with those obtained by Kuleff, Breidbach and Cederbaum [58] for the case of glycine. To perform a meaningful comparison, we have started from the same initial wave function as in [58]. The corresponding HF orbitals have been evaluated using Gaussian09 [165] with a DZP basis set. Then, to study the time evolution of the hole density, we have projected the initial state onto the Slater determinants built from the KS orbitals (shown in fig. 5.5) that we use to represent the ionic stationary states. The projection leads to a coherent superposition of ionic states that is let evolve freely as dictated by the relative phases resulting from the energy differences between the states. The evolution of the hole dynamics is shown in figs. 5.12 and 5.12 for the cases of sudden ionization from the $11a'$ and the $14a'$ HF orbitals, respectively. As can be seen, the agreement between our results and those previously reported [58] is quite satisfactory. In the latter reference, 2h1p configurations were explicitly included in the time propagation, so a direct comparison with their results provides an answer about the role played by those configurations, which are not included in our time propagation scheme.

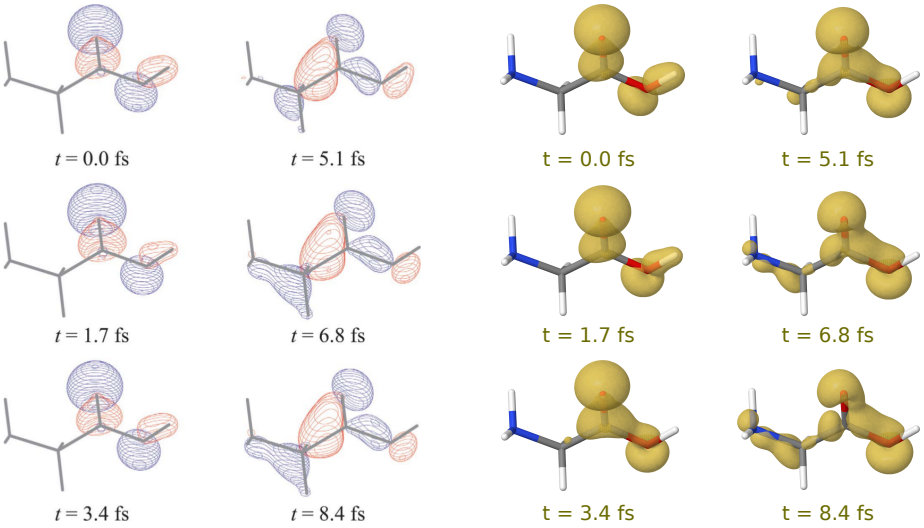

Figure 5.12: Time evolution of the hole generated in the glycine molecule upon sudden ionization from the $11a'$ HF orbital (at $t = 0$ the hole is completely localized in the $11a'$ HF orbital). Left figure: natural charge orbitals, as a function of time (the square of the natural orbitals provides the hole density). Reprinted with permission from [58]. Copyright 2005, AIP Publishing LLC. Right figure: hole density, evaluated using the present approach.

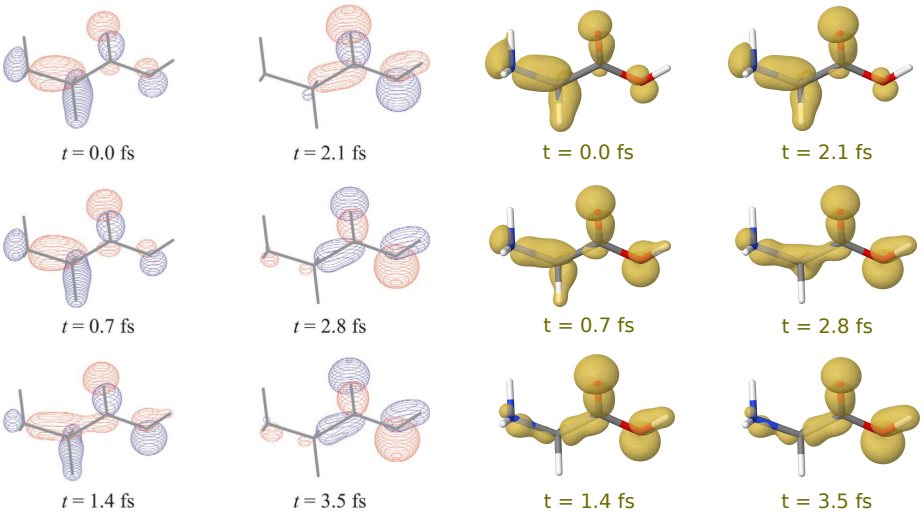

Figure 5.13: Same as fig. 5.12 for the case of sudden ionization from the $14a'$ HF orbital of glycine. Left figure reprinted with permission from [58]. Copyright 2005, AIP Publishing LLC.

If we considered sudden ionization from inner-shell HF orbitals of glycine instead, as in [59], the agreement would not be so spectacular, because in that case 2h1p configurations are expected to play an a role. However, as we show in this chapter, these are not expected to be important in the dynamics studied here. The main reason is that a transition from the ground to a shake-up state is a 2-electron process and therefore less likely to occur via 1 photon absorption than a direct transition to a 1h state.

We have calculated the evolution of the hole generated in the electronic structure of the amino acids glycine, phenylalanine and tryptophan upon interaction with an attosecond XUV pulse similar to that used in for experiment illustrated in fig. 5.1. Because of the high central frequency and large spectral width of the pulse (see figs. 5.8, 5.9 and 5.10), a manifold of ionization channels is open in the three amino acids, thus leading to coherent superpositions of many one-hole (1h) states, i.e., to electronic wave packets. Ionization amplitudes have been evaluated for all open channels (15 for glycine, 32 for phenylalanine and 39 for tryptophan) using the static-exchange density functional theory method [104, 105, 106, 107, 108] (see section 2.2.2), which has been thoroughly tested in systems of similar complexity, and time-dependent first-order perturbation theory (see section 1.2). From the ionization amplitudes, we have evaluated the reduced density matrix of the ionic subsystem using eq. 3.5. Then, the hole density was calculated as the difference between the electronic density of the neutral molecule, which does not depend on time, and the electronic density of the cation (eq. 3.8). Because in the experiments the molecules are not aligned, we performed calculations considering three orthogonal orientations with respect to the polarization vector of the attosecond pulse. The results were then averaged assuming randomly oriented molecules.

Figs. 5.14, 5.15 and 5.16 display snapshots of the relative variation of the hole density with respect to the time-averaged values for glycine, phenylalanine and tryptophan, respectively. In spite of the very delocalized nature of the hole density resulting from the broadband XUV excitation, a substantial redistribution of this density observed on a sub-femtosecond scale. This charge dynamics cannot be associated with a simple migration from one side of the molecule to the other, as found in most previous theoretical work [27, 58, 26, 59, 98]. However, despite the complexity of the charge configuration calculated in a realistic (i.e., experimentally accessible) situation, the concept of charge migration is still valid. We note that this dynamics occurs in a time scale which is faster than the nuclear vibrations (the fastest vibrational period phenylalanine is 9 fs, see table 5.3).

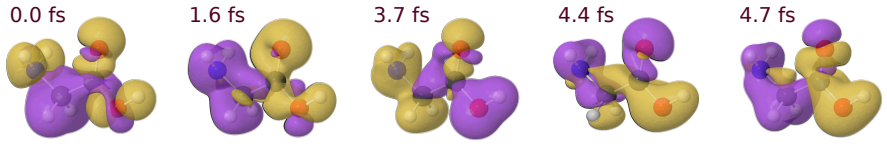

Figure 5.14: Relative variation of the hole on glycine density with respect to its time-averaged value as a function of time. Isosurfaces of the relative hole density are shown for cutoff values of 10^{-4} a. u. (yellow) and -10^{-4} (purple). Time is with reference to the end of the XUV pulse (first snapshot).

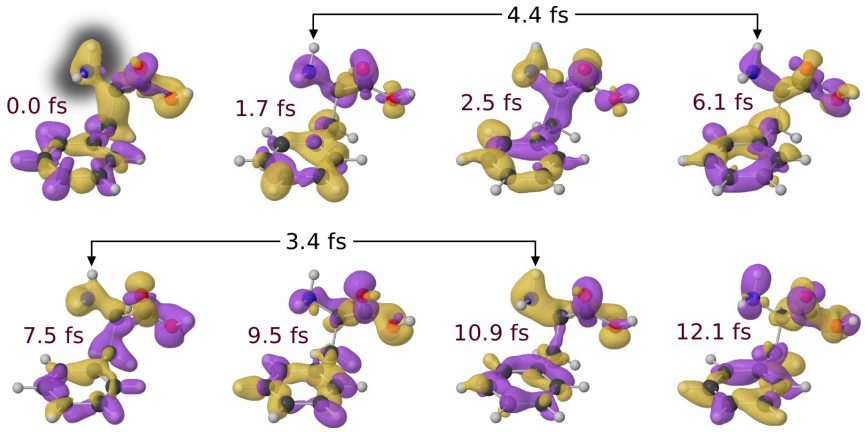

Figure 5.15: Same as fig 5.14 for phenylalanine. To guide the eye, time intervals between snapshots showing a similar accumulated density over the amino group are indicated. These time intervals are close to the dominant periods associated with the electronic wave-packet motion shown in figure 5.1. The location of the amino group is highlighted in the first snapshot with a shaded contour.

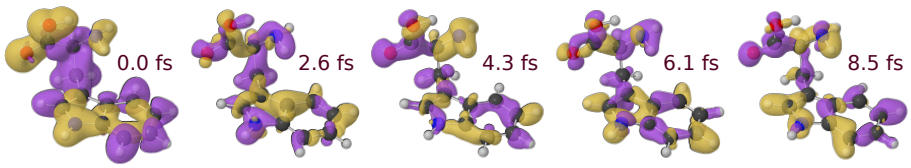

Figure 5.16: Same as fig 5.14 for tryptophan.

5.3.1 Fourier analysis on the amino group

In order to perform a more quantitative analysis of the charge dynamics, we have integrated the hole density around different portions of the molecule. In particular, we have focused on the amino group since in the pump-probe experiment on phenylalanine presented in figure 5.1, absorption of the VIS/NIR pulse is expected to be more likely to occur from that part of the molecule since the HOMO orbital is significantly localized there. Consequently, the fragmentation yield of doubly charge immonium is expected to be sensitive to charge localization on the amino group. A full analysis including different atomic centers is shown in the section 5.3.2. Figs. 5.17, 5.18 and 5.19 show the Fourier power spectra of the hole density on the amino group of glycine, phenylalanine and tryptophan, respectively, for three orthogonal orientations of the molecules with respect to the polarization vector of the field (indicated in the figures) and for the case of randomly oriented molecules. The peaks appearing in the Fourier spectra provide information about the frequency and the intensity of the charge fluctuations observed in figs. 5.14, 5.15 and 5.16. As expected, the complexity of the spectra increases with the number electrons in the molecule as so does the number of 1h states are accessible by the pulse.

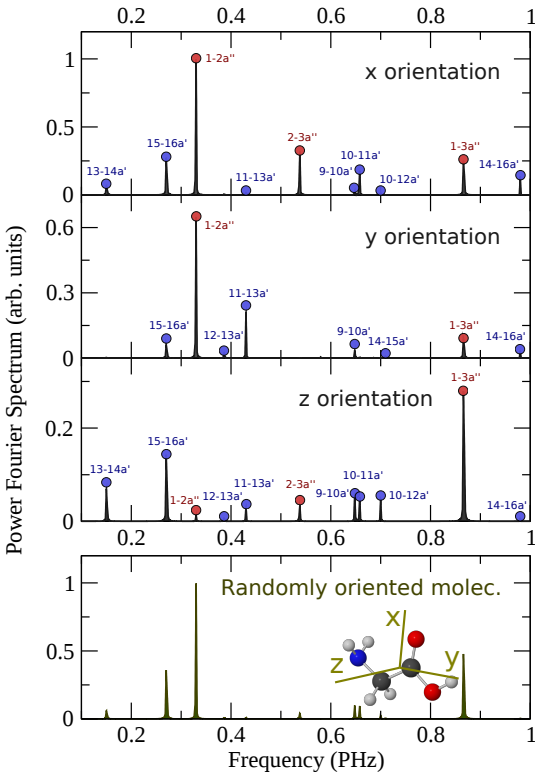

Figure 5.17: Fourier power spectra of the hole density integrated over the amino group of glycine. Results are shown for three orthogonal orientations of the molecule with respect to the polarization vector of the electric field associated to the attosecond XUV pulse and for the case of randomly oriented molecules. In order to obtain well resolved peaks in frequency, the hole density has been evaluated up to 500 fs. The states that give rise to the dominant peaks are indicated in the spectra by labels that denote the molecular orbitals where the holes have been created (see molecular orbitals in fig. 5.5).

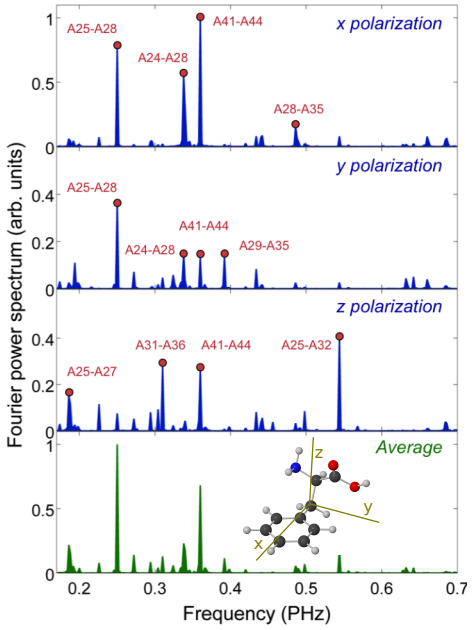

Figure 5.18: Same as fig. 5.17 for phenylalanine (molecular orbitals are shown in fig. 5.6).

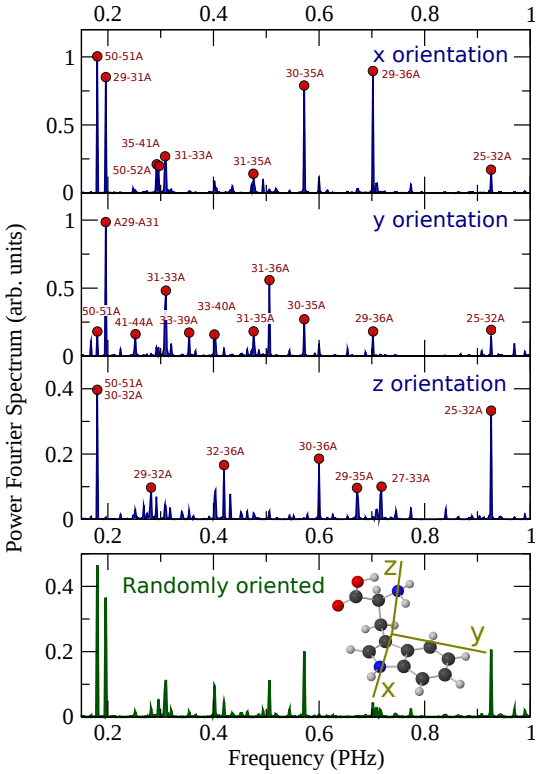

Figure 5.19: Same as fig. 5.17 for tryptophan (molecular orbitals are shown in fig. 5.7).

To better understand the observed dynamics, we have identified the 1h states that are responsible for the most important beatings (they are indicated in figs. 5.17, 5.18 and 5.19). The frequency at which each peak appears is dictated by the energy difference between the ionic states that give rise to it. As can be seen, the dominant beatings always involve two states that have holes in orbitals with significant density around the amino group and another common part of the molecule, which allows charge migration between the two sites.

The analysis of figs. 5.17, 5.18 and 5.19 also reveals that the dominant beatings involve states which are close in energy. In fact, the greater the energy spacing between two ionic states, the lower the intensity of the interference is expected to be. This can be easily understood in terms of the coherence between the ionic substates (states of the ionic subsystem) populated by the attosecond pulse, which is given by the off-diagonal terms of reduced density matrix (see eq. 3.5). If the energy spacing $\Delta E_{\alpha\alpha'} = |E_\alpha - E_{\alpha'}|$ between two ionic states α and α' is large, then the kinetic energy ranges in which the photoelectron is emitted when the two states are populated are very different and therefore the corresponding element in the reduced density matrix $\gamma_{\alpha\alpha'}$ is small. If $\Delta E_{\alpha\alpha'}$ were greater than the energy bandwidth of the pulse, the

two ionic states would be populated incoherently because the photoelectron kinetic energy ranges would not overlap at all and therefore $\gamma_{\alpha\alpha'}$ would be zero. Because of the large energy bandwidth of the attosecond pulse considered here, all 1h states are populated coherently, but coherences between states with similar energy are, in general, higher.

We can only see interferences between states having the same symmetry in the spectrum of glycine (fig. 5.17) because states with different symmetry are populated incoherently. The reason is that, for a given orientation of the field, electrons emitted from orbitals with different symmetry have, in general, different symmetry and therefore the coherence term $\gamma_{\alpha\alpha'}$ is zero (see eq. 3.5). In the case of phenylalanine and tryptophan (figs. 5.18 and 5.19), although no electron selection rules strictly apply due the lack of global symmetry elements, of course approximate local symmetries will apply. For instance, one of the most intense beatings in the amino group of phenylalanine occurs between the states with holes in the A41 and the A44 orbitals, both having nodal planes that contain the C−N and the C=N bonds with very similar orientations.

It is clear from the Fourier analysis presented here that the hole density not only provides information about energy spacings between different quantum states responsible of the electronic beatings, but also probes the specific dynamics generated by the attosecond pulse. This is further illustrated in fig. 5.20 for the case of phenylalanine, in which the calculated Fourier spectrum is compared with a similar one containing all possible energy spacings with an equal weight. The dynamics of the electronic wavepacket generation by the attosecond pulse is responsible for the fact that only a few beatings are observed. These depend on the dipole matrix elements (i.e., the ionizing transition induced by the XUV attosecond pulse) and the interference between the different amplitudes, which are imprinted in the time evolution of the hole density.

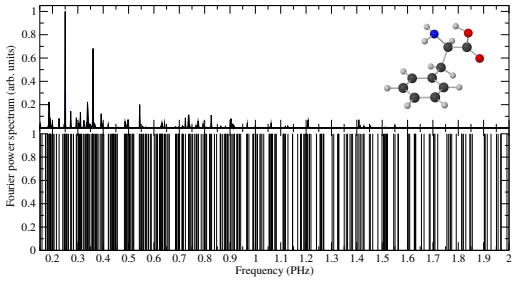

Figure 5.20: Fourier power spectra of the calculated hole density integrated over the amino group of phenylalanine. Upper panel: results from the actual calculation (as in the lower panel of fig. 5.18). Lower panel: results obtained by using an equal weight for all ionic states accessible by the XUV pulse.

To illustrate that the observed dynamics in the amino group can almost be entirely explained in terms of some of the ionic states that are populated by the attosecond XUV pulse, we have carried out calculations for phenylalanine

in which only ionic states resulting from removing an electron from the A24, A25, A28, A29, A31, A32, A35, A36, A41, and A44 orbitals are included in the free propagation of the electronic wave packet. Conversely, we have also performed calculations in which all 1h states but the above mentioned ones are included. The results of these two calculations are shown and compared with the full calculations in fig. 5.21. As can be seen, the full spectrum is almost entirely reproduced by only including the above ten states. In contrast, the dynamics resulting from excluding these states is almost inexistent.

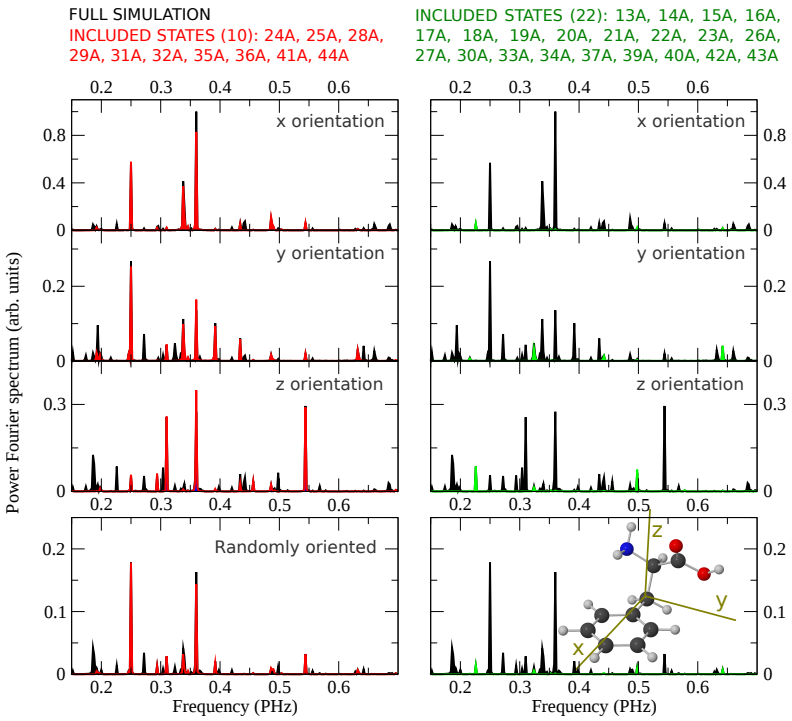

Figure 5.21: Fourier power spectra of the hole density integrated over the amino group of phenylalanine: results from the full calculation (black curves in all panels), from a calculation in which only the ionic states resulting from removing an electron from the 24A, 25A, 28A, 29A, 31A, 32A, 35A, 36A, 41A, and 44A orbitals are included (red curves, left panels), and from a calculation in which all ionic states but the above mentioned ones are included (green curves, right panels).

5.3.2 Fourier analysis on different atoms

Charge fluctuations on the amino group are most likely to be responsible for the observed beatings in the experimental results shown in 5.1. In order to perform a complete analysis of the charge fluctiations on different sites of the molecule,

we have performed a Fourier analysis also on different atoms of the three amino acids. Figs. 5.22, 5.23 and 5.24 show the Fourier power spectra of the hole density integrated over various atoms of the three molecules. As expected, charge fluctuations occur with different frequencies on different atoms because they are due to interferences between different pairs of 1h states. Indeed, it is a requirement for a beating to be observed on a specific site (atom) of the molecule that two states involved contain a significant part of their hole localized on that particular site.

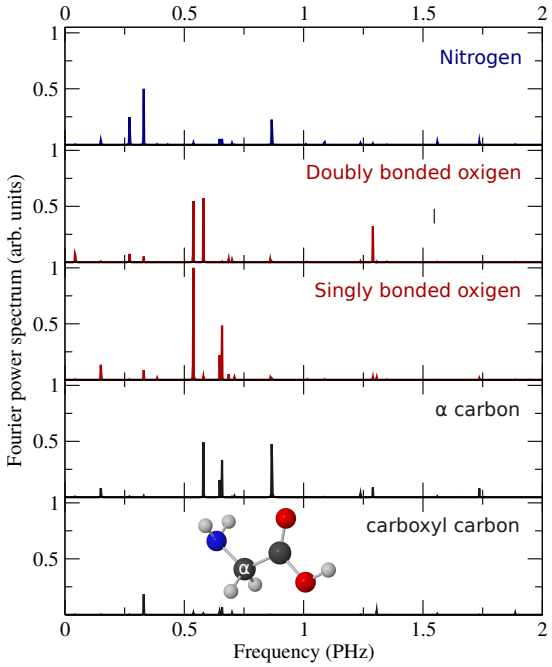

Figure 5.22: Fourier power spectra of the calculated hole density integrated over various atoms of glycine for the case of randomly oriented molecules. In order to obtain well resolved peaks in frequency, the hole density has been evaluated up to 500 fs.

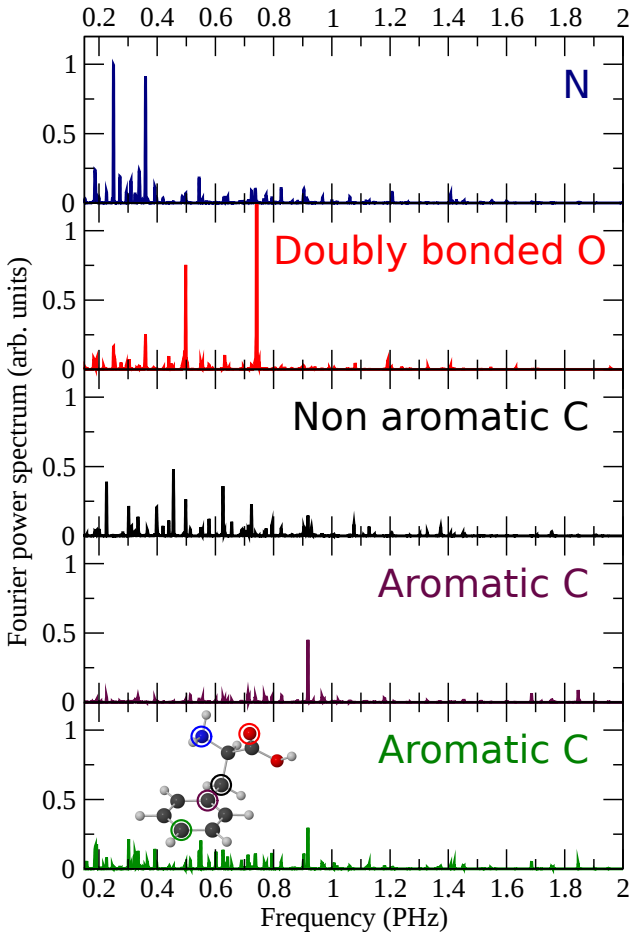

Figure 5.23: Same as 5.22 for phenylalanine.

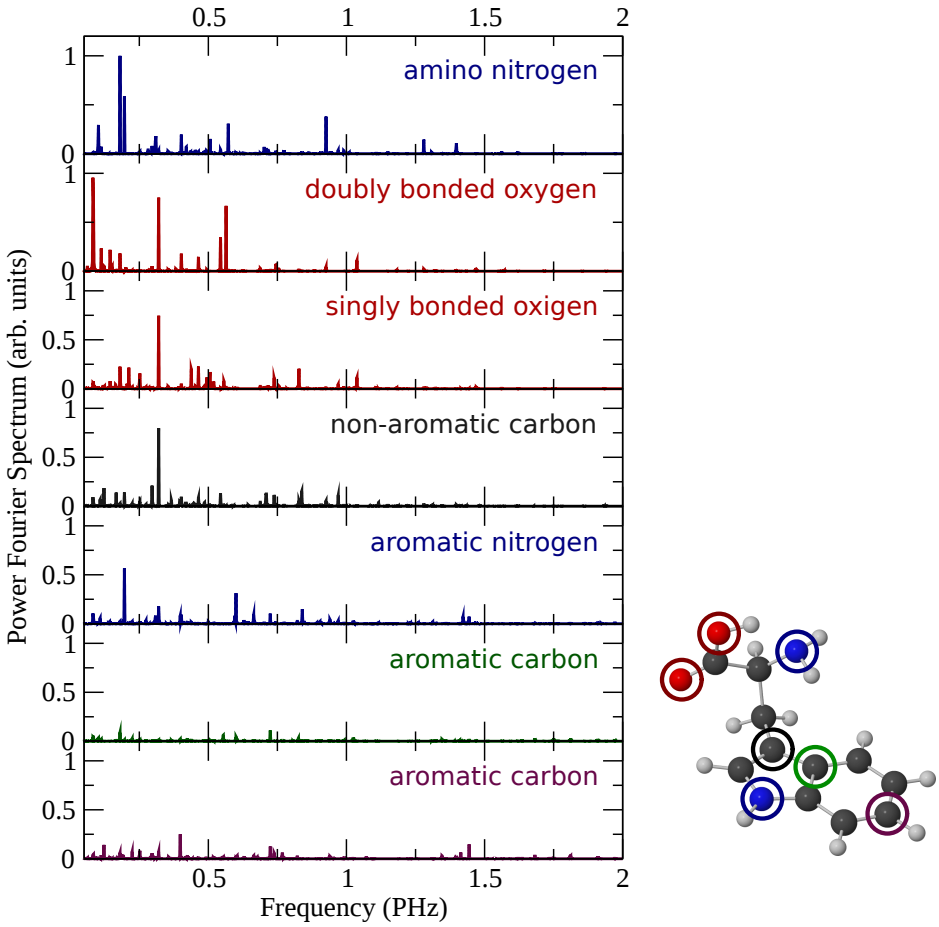

Figure 5.24: Same as 5.22 for tryptophan.

In the case of phenylalanine, beating frequencies in agreement with the experimental observations were observed when the charge density was integrated around the nitrogen atom in the N atom (amino group). The hole densities at different positions do not show clear and clean frequency components, with the exception of the doubly bonded O atom in the carboxyl group. We note that the VIS/NIR probe pulse is not locally absorbed only by the amino group, but also by other sites of the molecule. However, the simulations indicate that the periodic modulations observed in the experiment are mainly related to the absorption of the probe pulse by the amino group.

5.3.3 Comparison with the experiment: Gabor profiles

The hole density on the amino group has been also analyzed by using a sliding-window Fourier transform, which, at the expense of frequency resolution, shows

frequency and time information on the same plot. The same sliding-window Fourier transform procedure has been applied to the experimental fragmentation yield of doubly-charged immonium measured as a function of the pump-probe time delay, shown in figure 5.1. Figure 5.25 shows the resulting spectrograms in a temporal window up to 45 fs. A dominant peak around 0.25 PHz is visible, which forms in about 15 fs and vanishes after about 35 fs, in close agreement with the results of the Fourier analysis of the experimental data. A higher frequency component is visible around 0.36 PHz in the delay intervals below $\simeq$ 15 fs and above $\simeq$ 30 fs. At short delays, this component favorably compares with the experimental observation of the frequency peak around 0.30 PHz in the same window of pump-probe delays. The temporal evolution of the main Fourier components is a consequence of the complex interplay among several beating processes initiated by the broadband excitation pulse. Despite the agreement with the experimental results, we cannot exclude that the nuclear dynamics, which are not included in the simulations, also play a role in the temporal evolution of the measured oscillation frequencies.

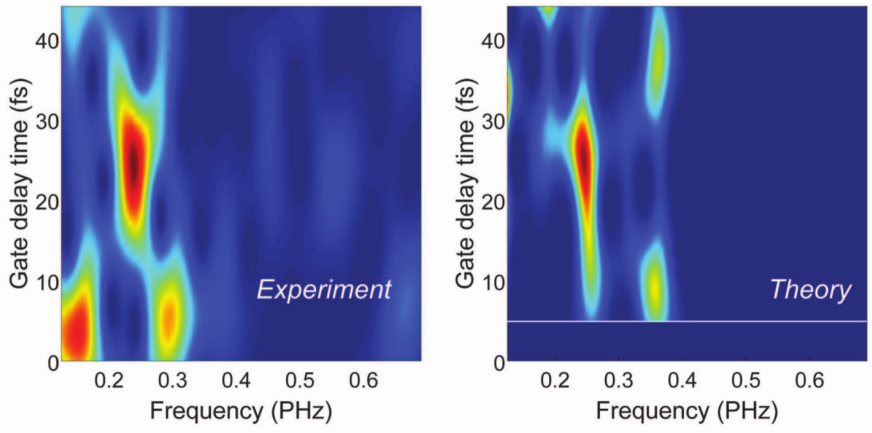

Figure 5.25: Fourier analysis of charge dynamics. Spectrograms calculated for the measured data of 5.1 (A) and for the calculated hole density integrated over the amino group of phenylalanine (B), shown in fig 5.15. The sliding window Fourier transforms have been calculated by using a Gaussian window function $g(t - t_d) = e^{-(t-t_d)^2/t_0^2}$, with $t_0 = 10$ fs and peak at t_d (gate delay time). The spectrogram (B) was calculated considering an experimental temporal resolution of about 3 fs.

The good agreement between simulations and experimental results is rather remarkable in light of the fact that simulations do not take into account the interaction of the VIS/NIR probe pulse. The fact that the effects of the probe pulse are not included in the simulations can explain why the calculated intensities of the different beatings differ from the experimental ones. We note that the beating frequencies have been observed experimentally even though the ini-

tial hole density is highly delocalized. An important result of the simulations is that the measured beating frequencies originate from charge dynamics around the amino group. This leads to the conclusion that the periodic modulations measured in the experiment are mainly related to the absorption of the probe pulse by the amino group. The mechanism that makes the probe pulse sensitive specifically to the charge density on this group is still not well understood. Moreover, we observe that, in spite of the large number of potential frequency beatings associated to the wave packet motion induced by the attosecond pulse, only a few ones manifest in the experiment, thus reducing the impact of the modulations introduced by the probe pulse in the analysis of the wave packet motion. The good agreement between our simulations of the temporal evolution of the electronic wave packet created by the attosecond pulse strongly supports the interpretation of the measured data in terms of charge migration, thus constituting the first experimental measurement of purely electron dynamics in a biomolecule.

5.3.4 What about molecular conformation?

It is well known that amino acids exist in many conformations as a result of their structural flexibility. Typically, the energy barrier to interconversion between different conformers is small, of the order of a few kcal/mol, so that, even at room temperature, thermal energy is sufficient to induce conformational changes. Theoretical investigations have shown that such changes can affect the charge migration process [59]. In the case of phenylalanine, 37 conformers have been found by ab initio calculations [168], with a conformational distribution that depends on temperature. However, in the experiment illustrated in fig. 5.1, performed at an average temperature of about 430 K, only the six conformers are substantially present [168]. Figures 5.26, 5.27 and 5.28 show the most stable conformations of glycine, phenylalanine and tryptophan at 430K. The relative populations of the phenylalanine conformers have been calculated using statistical mechanics methods based on DFT/B3LYP quantum chemistry calculations of the geometries, energies, vibrational frequencies and rotational constants of the 37 lowest conformers of phenylalanine [168]. In the case of glycine [167, 175] and tryptophan [169], the relative populations were estimated assuming Boltzman distributions.

The ultrafast temporal evolution of the wave packet generated by the attosecond pump pulse has also been calculated for the most stable conformers of the tree amino acids. The corresponding Fourier spectra are shown in figures 5.26, 5.27 and 5.28, together with the results for the thermal average obtained by taking into account the estimated populations (given in figures 5.26, 5.27 and 5.28). We have found that although the precise frequencies of the relevant peaks in the calculated Fourier spectra depend on the particular conformer, in general, there are no substantial differences and the spectrum of the most abundant conformer is very similar to that of the thermal average. In the case of the most populated conformers of phenylalanine (and therefore for the averaged results), the frequencies at which the dominant peaks appear are in good agreement with

those observed experimentally.

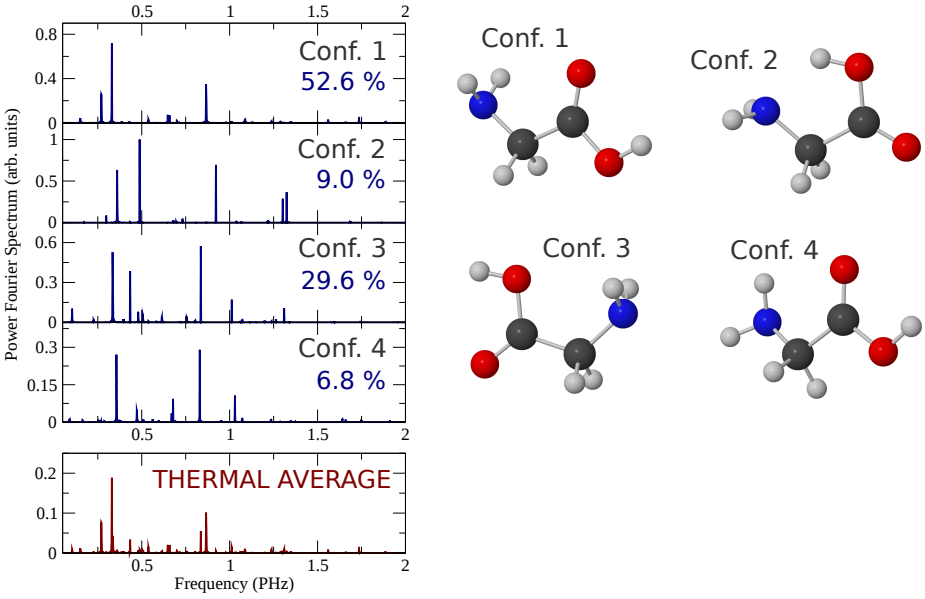

Figure 5.26: Fourier power spectra of the hole density on the amino group of the most abundant conformers of glycine at 430 K. The relative populations have been calculated assuming a Boltzman distribution. The lower panel shows the averaged results and the corresponding geometries are shown in the right.

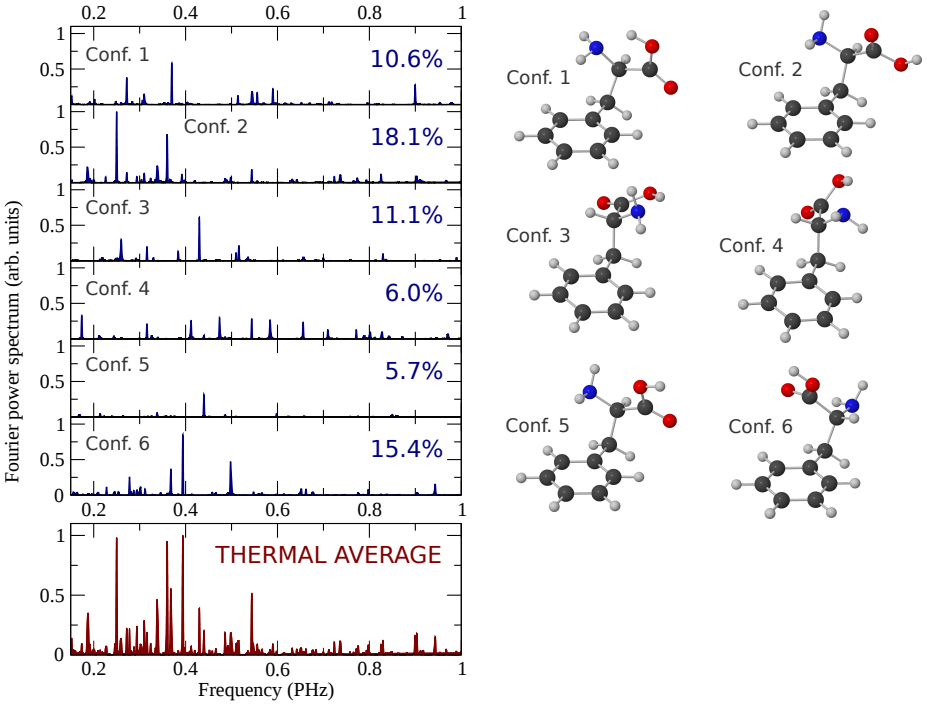

Figure 5.27: Same as fig. 5.26 for the most stable conformers of phenylalanine, rescaled with their relative weights for a better illustration. Their relative populations according to Huang *et al.* [168] are indicated.

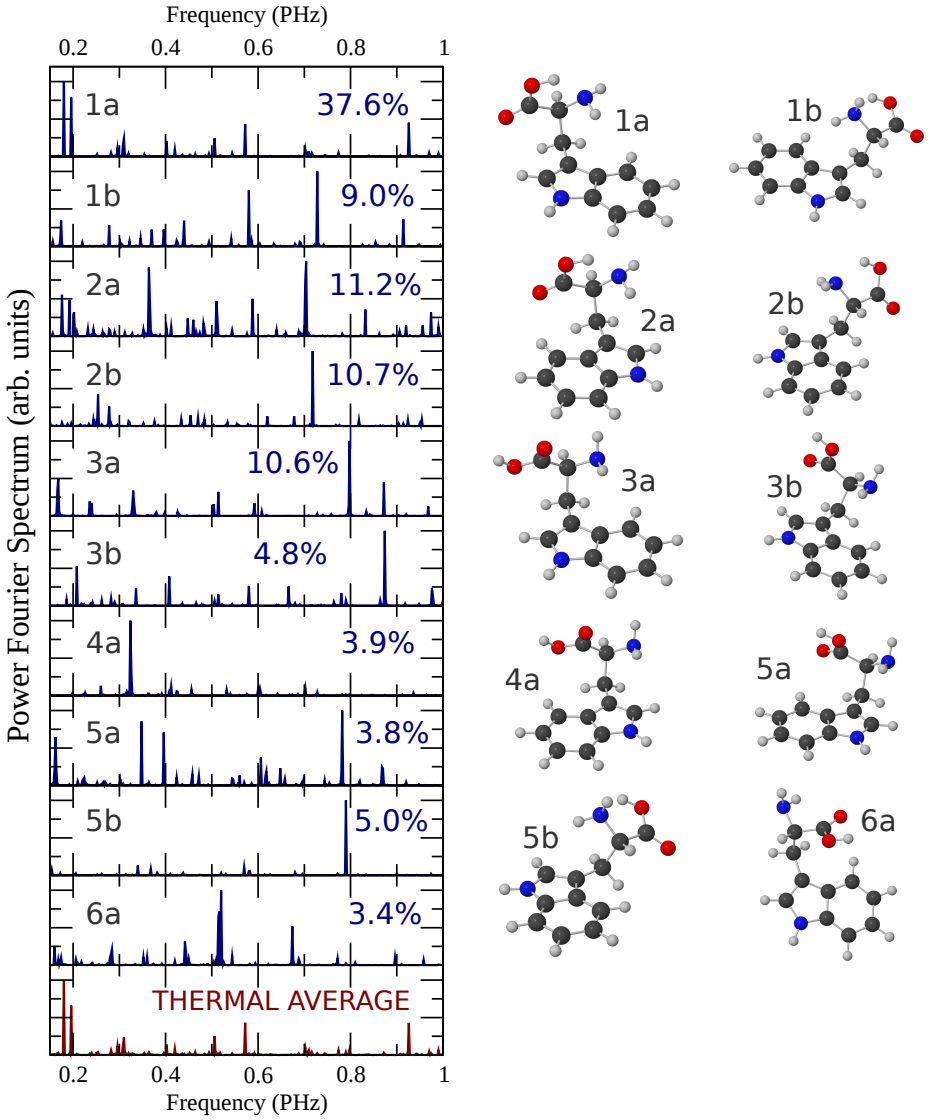

Figure 5.28: Same as fig. 5.26 for the most stable conformers of tryptophan. The relative populations have been calculated assuming a Boltzman distribution.

5.4 Time-evolution of the full electron system

The evaluation of the hole density generated upon ionization in terms of the reduced density matrix of the ionic subsystem has allowed to describe the ultrafast response of the parent ion. In order to visualize the time-evolution of the electron emitted to the continuum, we have evaluated the electron density

of the full system, including all the electrons. Figure 5.29 (upper panels) shows snapshots of the relative variation of the electron density of the full system. For the seek of comparison, snapshots of the relative variation of the electron density of the ionic subsystem is also represented in figure 5.29 (lower panels). Propagating the full electronic system in time allows to see the photoionization dynamics, which is superimposed to the ultrafast beatings in the parent ion. By comparing the results obtained with the two approaches, we can clearly see that the photoelectron cloud vanishes gradually as time goes by and, at around 0.7 fs, ionization is complete.

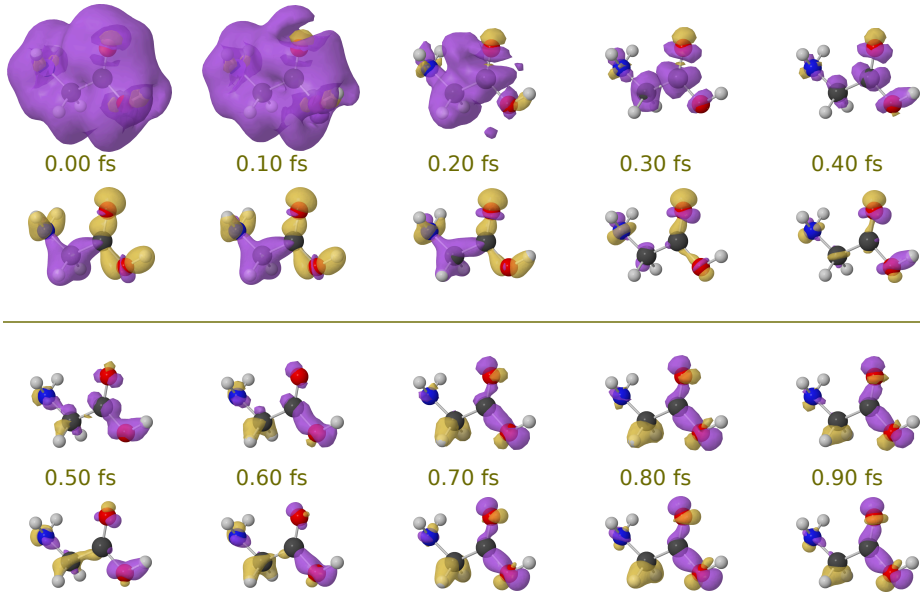

Figure 5.29: Relative variation of the hole on glycine density with respect to its time-averaged value as a function of time. Upper rows: dynamics of the full-system, containing all electrons. Lower rows: dynamics of the residual ion. Isosurfaces of the relative hole density are shown for cutoff values of 10^{-3} a. u. (yellow) and -10^{-3} (purple). Time is with reference to the end of the XUV pulse (first snapshots).

Conclusions

The advent of ultrabright light sources based on synchrotron radiation and ultrafast pulses based on high-harmonics generation (HHG) opened the door to image molecular structures and to monitor and even control electron and nuclear dynamics in their intrinsic time scales. In this quest, theoretical modeling and numerical simulations have been probed to be fundamental in the design of new experimental schemes and to understand the complex outcomes of those. Methods based on the Density Functional Theory (DFT) provide an excellent compromise between accuracy and computational effort. In this work, we have employed the static-exchange DFT method to compute the electronic structure of molecules (from CO or F_2 up to large amino acids) in order to predict and to understand recent experiments performed in two well-defined contexts: using third-generation light sources and using attosecond pulses generated via HHG. High-resolution third-generation synchrotron facilities have enabled the investigation of vibrationally-resolved inner-shell photoionization in small molecules made of first-row atoms. In chapter 4 and in appendices $1-5$ we have presented C 1s and B 1s vibrationally resolved photoionization cross sections of CO, CF_4 and BF_3, which have been evaluated using the static-exchange and the time-dependent DFT methods including the nuclear motion at the Born-Oppenheimer levels. By comparing our results with photoelectron spectra measured at SOLEIL and Spring-8 synchrotron light sources, we have found theoretical and experimental evidence non-Franck-Condon effects arising in inner-shell photoionization. When the de Broglie wave length of the photoelectron is comparable to the dimensions of the molecular target, i.e., for photon energies of the order of a few hundreds of eVs, the undulatory nature of the electron manifests as diffraction interferences by the surrounding atomic centers. These interferences are imprinted in the ratios between vibrationally resolved cross sections ($\nu-$ratios) as clear oscillations as a function of the photoelectron momentum. As a proof-of-principle, we have used the C 1s photoelectron spectra of CO to determine the internuclear distance of the neutral molecule and the bond contraction accompanying C 1s ionization. This is a surplus of photoelectron spectroscopy with respect to more conventional spectroscopic techniques, which usually can only provide structural information of neutral molecular species. Near the photoionization threshold, where the continuum waves are sensitive to the details of the molecular potentials, the cross sections show sharp features due to the presence of shape resonances. From the theoretical calculations,

and the angular momentum decompositions, we have also confirmed the existence of confinement effects as those previously found in more simple molecules. In the future, molecules such as BF_3, CF_4 or CO could provide an interesting workbench to study the photoelectron scattering phenomenon in a time-resolved (pump-probe) scheme using novel ultrahigh intensity photon sources like seeded FELs, which now become available.

We have also investigated photoionization of molecular fluorine, by considering electron ejection from different molecular orbitals using the static-exchange DFT method. For the outermost shells, we have included the nuclear degrees of freedom, which has allowed to describe dissociative and non-dissociative ionization channels. The photoionization cross sections show an oscillatory behavior as a function of the photoelectron momentum, which is the result of the coherent emission from two equivalent centers. The observed interference patterns are similar to those already explained by Cohen and Fano [154] in the early sixties. These interferences can be described by using very simple expressions that account for both the ratio between total photoionization cross sections associated to different orbitals and to the branching ratios between vibrationally resolved cross sections associated to the same electronic ionic state. Both effects were demonstrated in previous works [78] for other diatomic molecules, so the present work reinforces the general validity of those findings. The fact that there is a non-negligible probability of dissociation accompanying valence-ionization could be exploited experimentally to obtain molecular frame photoelectron angular distributions by using multi coincidence techniques, since detection of the charged atomic fragments provides information about the orientation of the molecule at the instant of ionization.

Since the generation of the first isolated attosecond pulses at the very beginning of the present century, tracing ultrafast phenomena using attosecond pump-probe techniques became a reality. The observation of charge migration in complex molecular structures and, in particular, in biologically relevant molecules, is one of the main targets of attosecond science. Although charge migration was predicted in the late nineties in the theoretical works of L. S. Cederbaum and coworkers, experimental evidence or reliable simulations on the initial electronic wave packet that could be created were inexistent. We have investigated the electronic response of molecules of biological relevance, the amino acids glycine, phenylalanine and tryptophan, to attosecond ionization. We have found that attosecond pulses induce ultrafast charge fluctuations over large regions of these complex molecules on a temporal scale much shorter than the vibrational response of the system. The work presented here differs to most previous theoretical work on charge migration, where charge dynamics is initiated by removing an electron from a given molecular orbital. Here, the use of the static-exchange DFT method in the framework of time-dependent first-order perturbation theory has allowed to evaluate the actual wave packet generated upon attosecond ionization. Because of the broad bandwidth of experimental attosecond pulses, in a realistic experiment electrons are coherently emitted from various (many) molecular orbitals and thus the initial hole is highly delocalized along the molecular skeleton. Our analysis of the wave packet dynamics reveals

ultrafast beatings on the electron density occurring on a sub-femtosecond temporal scale, which is shorter than the vibrational response of the molecule. The application of isolated attosecond pulses to prompt ionization of the amino acid phenylalanine has allowed the subsequent detection of ultrafast dynamics on a sub4.5-femtosecond temporal scale, which is shorter than the vibrational response of the molecule. The good agreement with our numerical simulations of the temporal evolution of the electronic wave packet created by the attosecond pulse strongly support the interpretation of the experimental data in terms of charge migration resulting from ultrafast electron dynamics preceding nuclear rearrangement.

Conclusiones

El advenimiento de fuentes de luz ultrabrillantes basadas en radiación sincrotrón y pulsos láser ultracortos basados en la generación de altos armónicos (HHG, del inglés "high-harmonics generation"), ha abierto la puerta para la visualización de estructuras moleculares y el seguimiento e incluso el control de dinámica electrónica y nuclear en sus escalas de tiempo intrínsecas. En esta misión, el modelado teórico y las simulaciones teóricas han demostrado jugar un papel fundamental en el diseo de nuevos experimentos así como en la comprensión de los complejos resultados obtenidos en los mismos. Los métodos basados en la Teoría del Funcional de la Densidad (DFT) proporcionan un compromiso excelente entre precisión y esfuerzo computacional. En este trabajo, hemos empleado el método "static-exchange DFT" para evaluar la estructura electrónica de moléculas (desde CO o F_2 hasta grandes amino ácidos) con el objetivo de predecir y comprender experimentos recientes realizados bajo condiciones bien distintas: utilizando fuentes de luz de tercera generación y pulsos generados mediante HHG. Las instalaciones sincrotrón de última generación han permitido la investigación de procesos de fotoionización en moléculas pequeas constituidas por átomos del primer periodo con resolución vibracional. En el capítulo 4 y en los apéndices $1-5$ hemos presentado secciones eficaces de fotoionización de capa interna en las moléculas CO, CF_4 and BF_3, que han sido calculadas utilizando el método "static-exchange DFT" y su versión dependiente del tiempo, incluyendo el movimiento nuclear a nivel de Born-Oppenheimer. Comparando nuestros resultados con espectros fotoelectrónicos medidos en los sincrotrones SOLEIL y Spring-8, hemos encontrado evidencias teóricas y experimentales de desviaciones de Franck-Condon en procesos de ionización de capa interna. Cuando la longitud de onda de de Broglie del fotoelectrón es comparable a las dimensiones de la molécula, es decir, para energías del fotoelectrón del orden de unos cientos de eVs, la naturaleza ondulatoria del fotoelectrón se manifiesta como interferencias de difracción por los átomos circundantes. Estas interferencias se hacen visibles en los ratios entre secciones eficaces resueltas vibracionalmente ($\nu-$ratios), ocasionando claras oscilaciones en función del momento del fotoelectrón. Como prueba de concepto, hemos utilizado espectros fotoelectrónicos de la molécula de CO para determinar la distancia internuclear de la especie neutra y la contracción del enlace tras arrancar un electrón del orbital 1s del átomo de carbono. Cerca del umbral de ionización, donde las funciones del continuo son mas sensibles a los detalles de los potenciales moleculares, las sec-

ciones eficaces se manifiestan como estructuras agudas que tienen su origen en resonancias de forma. Además, la descomposición en momento angular permite confirmar la existencia de efectos de confinamiento, similares a los que se han encontrado previamente en moléculas más simples. En el futuro, moléculas como BF_3, CF_4 or CO prodrían propocionar un punto de referencia en el estudio del fenómeno de difracción fotoelectrónica utilizando métodos bombeo-sonda con pulsos ultraintensos de láseres de electrones libres.

También hemos investigado la fotoionización de la molécula de fluor, considerando emisión fotoelectrónica desde distintos orbitales mediante el método "static-exchange DFT". Para las capas más externas, hemos incluido los grados de libertad nucleares, lo cual ha nos ha permitido describir canales disociativos y no disociativos. Las secciones eficaces de fotoionización muestran oscilaciones en funcion del momento del fotoelectron, lo cual es resultado de un proceso de emisión multicéntrica desde dos centros equivalentes. Estos patrones de interferencia son similares a los que Cohen y Fano [154] dieron explicación en los aos 60. Efectos similares han sido observados en trabajos previos [78] en otras moléculas diatómicas, así que este trabajo refuerza la validez general de esos hallazgos. El echo de que existe una probabilidad no despreciable de que la molécula de flúor disocie tras ser ionizada desde sus capas de valencia, podría ser utilizada experimentalmente para obtener distribuciones angulares del fotoelectrón utilizando técnicas de coincidencia, ya que la detección de fragmentos atómicos cargados proporciona información sobre la orientación de la molécula en el instante de la ionización.

Desde la generación del primer pulso de atosegundos al comienzo de este siglo, la observación de dinámica electrónica mediante el uso de pulsos de atosegundos es posible. La observación de migración de carga en estructuras moleculares complejas y, en particular, en moléculas con relevancia biológica, es uno de los objetivos fundamentales de la ciencia de atosegundos. Los procesos de migración de carga fueron predichos a finales de la década de los noventa en los trabajos teóricos de L. S. Cederbaum y sus colaboradores. En este trabajo hemos investigado procesos de respuesta electrónica a ionización ultrarrápida en moléculas de relevancia biológica: los amino ácidos glicina, fenilalanina y triptófano. Hemos descubierto que los pulsos de atosegundos induce fluctuaciones de carga ultrarrápida en estas moléculas complejas que preceden al movimiento vibracional. El trabajo presentado aquí es distinto de otros trabajos previos sobre migración de carga, donde la dinámica es iniciada arrancando un electrón de un orbital molecular determinado. El uso del método static-exchange DFT y de teoría de perturbaciones a primer orden ha permitido la evaluación del paquete de onda electrónico que se genera mediante un pulso de atosegundos. Debido a los anchos espectros energéticos de los pulsos experimentales de atosegundos, en estos experimentos se emiten electrones desde muchos orbitales moleculares de forma coherente y, por lo tanto, se genera un hueco que está completamente deslocalizado en el esqueleto molecular. Nuestro análisis del paquete de ondas electrónico revela fluctuaciones ultrarrápidas de la densidad electrónica que ocurren en una escala de tiempo en el orden de los sub-femtosegundos, mucho más rápida que el movimiento nuclear. La aplicación

de pulso de atosegundos aislados a la ionización del aminoácido fenilalanina ha permitido la detección experimental de dinámica electrónica ultrarrápida. El buen acuerdo con nuestros resultados teóricos apoya la interpretación de los datos experimentales en términos de migración de carga.

Appendices

Bibliography

[1] Ahmed H. Zewail. Femtochemistry: atomic-scale dynamics of the chemical bond. *The Journal of Physical Chemistry A*, 104(24):5660–5694, 2000.

[2] Zewail Ahmed H. *Pure and Applied Chemistry*, volume 72, chapter Femtochemistry. Past, present, and future, page 2219. 2015 2000. 12.

[3] Nobelprize.org. Press release: The 1999 nobel prize in chemistry. 1999.

[4] M. Hentschel, R. Kienberger, Ch Spielmann, G. A. Reider, N. Milosevic, T. Brabec, P. Corkum, U. Heinzmann, M. Drescher, and F. Krausz. Attosecond metrology. *Nature*, 414(6863):509–513, Nov 2001.

[5] P. M. Paul, E. S. Toma, P. Breger, G. Mullot, F. Aug, Ph. Balcou, H. G. Muller, and P. Agostini. Observation of a train of attosecond pulses from high harmonic generation. *Science*, 292(5522):1689–1692, 2001.

[6] A. McPherson, G. Gibson, H. Jara, U. Johann, T. S. Luk, I. A. McIntyre, K. Boyer, and C. K. Rhodes. Studies of multiphoton production of vacuum-ultraviolet radiation in the rare gases. *J. Opt. Soc. Am. B*, 4(4):595–601, Apr 1987.

[7] M Ferray, A L'Huillier, X F Li, L A Lompre, G Mainfray, and C Manus. Multiple-harmonic conversion of 1064 nm radiation in rare gases. *Journal of Physics B: Atomic, Molecular and Optical Physics*, 21(3):L31, 1988.

[8] P. B. Corkum. Plasma perspective on strong field multiphoton ionization. *Phys. Rev. Lett.*, 71:1994–1997, Sep 1993.

[9] Pierre Agostini and Louis F DiMauro. The physics of attosecond light pulses. *Reports on Progress in Physics*, 67(6):813, 2004.

[10] Ferenc Krausz and Misha Ivanov. Attosecond physics. *Rev. Mod. Phys.*, 81:163–234, Feb 2009.

[11] J. Itatani, F. Quéré, G. L. Yudin, M. Yu. Ivanov, F. Krausz, and P. B. Corkum. Attosecond streak camera. *Phys. Rev. Lett.*, 88:173903, Apr 2002.

[12] G. Sansone, E. Benedetti, F. Calegari, C. Vozzi, L. Avaldi, R. Flammini, L. Poletto, P. Villoresi, C. Altucci, R. Velotta, S. Stagira, S. De Silvestri, and M. Nisoli. Isolated single-cycle attosecond pulses. *Science*, 314(5798):443–446, 2006.

[13] E. Goulielmakis, M. Schultze, M. Hofstetter, V. S. Yakovlev, J. Gagnon, M. Uiberacker, A. L. Aquila, E. M. Gullikson, D. T. Attwood, R. Kienberger, F. Krausz, and U. Kleineberg. Single-cycle nonlinear optics. *Science*, 320(5883):1614–1617, 2008.

[14] Kun Zhao, Qi Zhang, Michael Chini, Yi Wu, Xiaowei Wang, and Zenghu Chang. Tailoring a 67 attosecond pulse through advantageous phase-mismatch. *Opt. Lett.*, 37(18):3891–3893, Sep 2012.

[15] P. B. Corkum and Ferenc Krausz. Attosecond science. *Nat Phys*, 3(6):381–387, Jun 2007.

[16] Alicia Palacios, Jos Luis Sanz-Vicario, and Fernando Martn. Theoretical methods for attosecond electron and nuclear dynamics: applications to the h 2 molecule. *Journal of Physics B: Atomic, Molecular and Optical Physics*, 48(24):242001, 2015.

[17] M. Drescher, M. Hentschel, R. Kienberger, M. Uiberacker, V. Yakovlev, A. Scrinzi, Th Westerwalbesloh, U. Kleineberg, U. Heinzmann, and F. Krausz. Time-resolved atomic inner-shell spectroscopy. *Nature*, 419(6909):803–807, Oct 2002.

[18] M. Uiberacker, Th Uphues, A. J. Schultze, M.and Verhoef, V. Yakovlev, M. F. Kling, J. Rauschenberger, N. M. Kabachnik, H. Schroder, M. Lezius, K. L. Kompa, H.-G. Muller, M. J. J. Vrakking, S. Hendel, U. Kleineberg, U. Heinzmann, M. Drescher, and F. Krausz. Attosecond real-time observation of electron tunnelling in atoms. *Nature*, 446(7136):627–632, Apr 2007.

[19] M. Schultze, M. Fie, N. Karpowicz, J. Gagnon, M. Korbman, M. Hofstetter, S. Neppl, A. L. Cavalieri, Y. Komninos, Th. Mercouris, C. A. Nicolaides, R. Pazourek, S. Nagele, J. Feist, J. Burgdrfer, A. M. Azzeer, R. Ernstorfer, R. Kienberger, U. Kleineberg, E. Goulielmakis, F. Krausz, and V. S. Yakovlev. Delay in photoemission. *Science*, 328(5986):1658–1662, 2010.

[20] K. Klünder, J. M. Dahlström, M. Gisselbrecht, T. Fordell, M. Swoboda, D. Guénot, P. Johnsson, J. Caillat, J. Mauritsson, A. Maquet, R. Taïeb, and A. L'Huillier. Probing single-photon ionization on the attosecond time scale. *Phys. Rev. Lett.*, 106:143002, Apr 2011.

[21] Eleftherios Goulielmakis, Zhi-Heng Loh, Adrian Wirth, Robin Santra, Nina Rohringer, Vladislav S. Yakovlev, Sergey Zherebtsov, Thomas Pfeifer, Abdallah M. Azzeer, Matthias F. Kling, Stephen R. Leone, and

Ferenc Krausz. Real-time observation of valence electron motion. *Nature*, 466(7307):739–743, Aug 2010.

[22] A. L. Cavalieri, N. Muller, Th Uphues, V. S. Yakovlev, A. Baltuska, B. Horvath, B. Schmidt, L. Blumel, R. Holzwarth, S. Hendel, M. Drescher, U. Kleineberg, P. M. Echenique, R. Kienberger, F. Krausz, and U. Heinzmann. Attosecond spectroscopy in condensed matter. *Nature*, 449(7165):1029–1032, Oct 2007.

[23] Agustin Schiffrin, Tim Paasch-Colberg, Nicholas Karpowicz, Vadym Apalkov, Daniel Gerster, Sascha Muhlbrandt, Michael Korbman, Joachim Reichert, Martin Schultze, Simon Holzner, Johannes V. Barth, Reinhard Kienberger, Ralph Ernstorfer, Vladislav S. Yakovlev, Mark I. Stockman, and Ferenc Krausz. Optical-field-induced current in dielectrics. *Nature*, 493(7430):70–74, Jan 2013.

[24] Franck Lepine, Misha Y. Ivanov, and Marc J. J. Vrakking. Attosecond molecular dynamics: fact or fiction? *Nat Photon*, 8(3):195–204, Mar 2014. Review.

[25] Louise Belshaw, Francesca Calegari, Martin J. Duffy, Andrea Trabattoni, Luca Poletto, Mauro Nisoli, and Jason B. Greenwood. Observation of ultrafast charge migration in an amino acid. *The Journal of Physical Chemistry Letters*, 3(24):3751–3754, 2012. PMID: 26291106.

[26] F. Remacle and R. D. Levine. An electronic time scale in chemistry. *Proceedings of the National Academy of Sciences*, 103(18):6793–6798, May 2006.

[27] Lorenz S. Cederbaum and J. Zobeley. Ultrafast charge migration by electron correlation. *Chemical Physics Letters*, 307(3-4):205–210, 1999.

[28] J. Breidbach and L. S. Cederbaum. Migration of holes: Formalism, mechanisms, and illustrative applications. *The Journal of Chemical Physics*, 118(9), 2003.

[29] J. Breidbach and L. S. Cederbaum. Universal attosecond response to the removal of an electron. *Phys. Rev. Lett.*, 94:033901, Jan 2005.

[30] Holger Hennig, Jrg Breidbach, , and Lorenz S. Cederbaum. Electron correlation as the driving force for charge transfer: charge migration following ionization in n-methyl acetamide. *The Journal of Physical Chemistry A*, 109(3):409–414, 2005. PMID: 16833360.

[31] R. Weinkauf, P. Schanen, D. Yang, S. Soukara, and E. W. Schlag. Elementary processes in peptides: Electron mobility and dissociation in peptide cations in the gas phase. *The Journal of Physical Chemistry*, 99(28):11255–11265, 1995.

[32] R. Weinkauf, P. Schanen, A. Metsala, , E. W. Schlag, M. Brgle, , and H. Kessler. Highly efficient charge transfer in peptide cations in the gas phase: threshold effects and mechanism. *The Journal of Physical Chemistry*, 100(47):18567–18585, 1996.

[33] J. Wals, H. H. Fielding, J. F. Christian, L. C. Snoek, W. J. van der Zande, and H. B. van Linden van den Heuvell. Observation of rydberg wave packet dynamics in a coulombic and magnetic field. *Phys. Rev. Lett.*, 72:3783–3786, Jun 1994.

[34] J. D. Jackson. *Classical electrodynamics*. Wiley, 1975.

[35] F. R. Elder, A. M. Gurewitsch, R. V. Langmuir, and H. C. Pollock. Radiation from electrons in a synchrotron. *Phys. Rev.*, 71:829–830, Jun 1947.

[36] Donald H Bilderback, Pascal Elleaume, and Edgar Weckert. Review of third and next generation synchrotron light sources. *Journal of Physics B: Atomic, Molecular and Optical Physics*, 38(9):S773, 2005.

[37] Gerard K. O'Neill. Storage-ring synchrotron: Device for high-energy physics research. *Phys. Rev.*, 102:1418–1419, Jun 1956.

[38] Ros Herman. Structure experiment ring is light on cash. *New Scientist*, 84(1171):357, November.

[39] Ros Herman. Daresbury: tunable radiation for research. *New Scientist*, 87(1211):310, July.

[40] D J Holder, P D Quinn, and N G Wyles. The SRS at Daresbury Laboratory: a Eulogy to the World's First Dedicated High-energy Synchrotron Radiation Source. *11th European Particle Accelerator Conference*, 2008.

[41] H. Baumgaertel. Bessy - the berlin electron storage ring. 29(7):440–444, 1981.

[42] R. Stumm von Bordwehr. A history of x-ray absorption fine structure. *Ann. Phys. Fr.*, 14(4):377–465, 1989.

[43] Edward A. Stern. Musings about the development of XAFS. *Journal of Synchrotron Radiation*, 8(2):49–54, Mar 2001.

[44] Herman Winick, George Brown, Klaus Halbach, and John Harris. Wiggler and undulator magnets. *Physics Today*, 34:50–63, 1981.

[45] ke Kvick. Special issue synchroton radiation and inorganic crystallography the european synchrotron radiation facilityan overview of planned diffraction capability. *Journal of Physics and Chemistry of Solids*, 52(10):1307 – 1312, 1991.

[46] Freddy Adams. Opening ceremony of the european synchrotron radiation facility (esrf). *J. Anal. At. Spectrom.*, 10:12N–13N, 1995.

[47] H. Wabnitz, L. Bittner, A. R. B. de Castro, R. Dohrmann, P. Gurtler, T. Laarmann, W. Laasch, J. Schulz, A. Swiderski, K. von Haeften, T. Moller, B. Faatz, A. Fateev, J. Feldhaus, C. Gerth, U. Hahn, E. Saldin, E. Schneidmiller, K. Sytchev, K. Tiedtke, R. Treusch, and M. Yurkov. Multiple ionization of atom clusters by intense soft x-rays from a free-electron laser. *Nature*, 420(6915):482–485, Dec 2002.

[48] Ackermann W., Asova G., Ayvazyan V., Azima A., Baboi N., Bahr J., Balandin V., Beutner B., Brandt A., Bolzmann A., Brinkmann R., Brovko O. I., Castellano M., Castro P., Catani L., Chiadroni E., Choroba S., Cianchi A., Costello J. T., Cubaynes D., Dardis J., Decking W., Delsim-Hashemi H., Delserieys A., Di PirroG., Dohlus M., Dusterer S., Eckhardt A., Edwards H. T., Faatz B., Feldhaus J., Flottmann K., Frisch J., Frohlich L., Garvey T., Gensch U., Gerth Ch., Gorler M., Golubeva N., Grabosch H.-J., Grecki M., Grimm O., Hacker K., Hahn U., Han H. J., Honkavaara K., Hott T., Huning M., Ivanisenko Y., Jaeschke E., Jalmuzna W., Jezynski T., Kammering R., Katalev V., Kavanagh K., Kennedy E. T., Khodyachykh S., Klose K., Kocharyan V., Korfer M., Kollewe M., Koprek W., Korepanov S., Kostin D., Krassilnikov M., Kube G., Kuhlmann M., Lewis C. L. S., Lilje L., Limberg T., Lipka D., Lohl F., Luna H., Luong M., Martins M., Meyer M., Michelato P., Miltchev V., Moller W. D., Monaco L., Muller W. F. O., Napieralski O., Napoly O., Nicolosi P., Nolle D., Nunez T., Oppelt A., Pagani C., Paparella R., Pchalek N., Pedregosa-Gutierrez J., Petersen B., Petrosyan B., Petrosyan G., Petrosyan L., Pfluger J., Plonjes E., Poletto L., Pozniak K., Prat E., Proch D., Pucyk P., Radcliffe P., Redlin H., Rehlich K., Richter M., Roehrs M., Roensch J., Romaniuk R., Ross M., Rossbach J., Rybnikov V., Sachwitz M., Saldin E. L., Sandner W., Schlarb H., Schmidt B., Schmitz M., Schmuser P., Schneider J. R., Schneidmiller E. A., Schnepp S., Schreiber S., Seidel M., Sertore D., Shabunov A. V., Simon C., Simrock S., Sombrowski E., Sorokin A. A., Spanknebel P., Spesyvtsev R., Staykov L., Steffen B., Stephan F., Stulle F., Thom H., Tiedtke K., Tischer M., Toleikis S., Treusch R., Trines D., Tsakov I., Vogel E., Weiland T., Weise H., Wellhofer M., Wendt M., Will I., Winter A., Wittenburg K., Wurth W., Yeates P., Yurkov M. V., Zagorodnov I., and Zapfe K. Operation of a free-electron laser from the extreme ultraviolet to the water window. *Nat Photon*, 1(6):336–342, Jun 2007.

[49] Henry N. Chapman, Anton Barty, Michael J. Bogan, Sebastien Boutet, Matthias Frank, Stefan P. Hau-Riege, Stefano Marchesini, Bruce W. Woods, Sasa Bajt, W. Henry Benner, Richard A. London, Elke Plonjes, Marion Kuhlmann, Rolf Treusch, Stefan Dusterer, Thomas Tschentscher, Jochen R. Schneider, Eberhard Spiller, Thomas Moller, Christoph Bostedt, Matthias Hoener, David A. Shapiro, Keith O. Hodgson, David van der Spoel, Florian Burmeister, Magnus Bergh, Carl Caleman, Gosta Huldt, M. Marvin Seibert, Filipe R. N. C. Maia, Richard W. Lee, Abraham Szoke,

Nicusor Timneanu, and Janos Hajdu. Femtosecond diffractive imaging with a soft-x-ray free-electron laser. *Nat Phys*, 2(12):839–843, Dec 2006.

[50] Henry N. Chapman, Stefan P. Hau-Riege, Michael J. Bogan, Sasa Bajt, Anton Barty, Sebastien Boutet, Stefano Marchesini, Matthias Frank, Bruce W. Woods, W. Henry Benner, Richard A. London, Urs Rohner, Abraham Szoke, Eberhard Spiller, Thomas Moller, Christoph Bostedt, David A. Shapiro, Marion Kuhlmann, Rolf Treusch, Elke Plonjes, Florian Burmeister, Magnus Bergh, Carl Caleman, Gosta Huldt, M. Marvin Seibert, and Janos Hajdu. Femtosecond time-delay x-ray holography. *Nature*, 448(7154):676–679, Aug 2007.

[51] Stefano Marchesini, Sebastien Boutet, Anne E. Sakdinawat, Michael J. Bogan, Sasa Bajt, Anton Barty, Henry N. Chapman, Matthias Frank, Stefan P. Hau-Riege, Abraham Szoke, Congwu Cui, David A. Shapiro, Malcolm R. Howells, John C. H. Spence, Joshua W. Shaevitz, Joanna Y. Lee, Janos Hajdu, and Marvin M. Seibert. Massively parallel x-ray holography. *Nat Photon*, 2(9):560–563, Sep 2008.

[52] Allison Doerr. Diffraction before destruction. *Nat Meth*, 8(4):283–283, Apr 2011.

[53] Henry N. Chapman, Petra Fromme, Anton Barty, Thomas A. White, Richard A. Kirian, Andrew Aquila, Mark S. Hunter, Joachim Schulz, Daniel P. DePonte, Uwe Weierstall, R. Bruce Doak, Filipe R. N. C. Maia, Andrew V. Martin, Ilme Schlichting, Lukas Lomb, Nicola Coppola, Robert L. Shoeman, Sascha W. Epp, Robert Hartmann, Daniel Rolles, Artem Rudenko, Lutz Foucar, Nils Kimmel, Georg Weidenspointner, Peter Holl, Mengning Liang, Miriam Barthelmess, Carl Caleman, Sebastien Boutet, Michael J. Bogan, Jacek Krzywinski, Christoph Bostedt, Sasa Bajt, Lars Gumprecht, Benedikt Rudek, Benjamin Erk, Carlo Schmidt, Andre Homke, Christian Reich, Daniel Pietschner, Lothar Struder, Gunter Hauser, Hubert Gorke, Joachim Ullrich, Sven Herrmann, Gerhard Schaller, Florian Schopper, Heike Soltau, Kai-Uwe Kuhnel, Marc Messerschmidt, John D. Bozek, Stefan P. Hau-Riege, Matthias Frank, Christina Y. Hampton, Raymond G. Sierra, Dmitri Starodub, Garth J. Williams, Janos Hajdu, Nicusor Timneanu, M. Marvin Seibert, Jakob Andreasson, Andrea Rocker, Olof Jonsson, Martin Svenda, Stephan Stern, Karol Nass, Robert Andritschke, Claus-Dieter Schroter, Faton Krasniqi, Mario Bott, Kevin E. Schmidt, Xiaoyu Wang, Ingo Grotjohann, James M. Holton, Thomas R. M. Barends, Richard Neutze, Stefano Marchesini, Raimund Fromme, Sebastian Schorb, Daniela Rupp, Marcus Adolph, Tais Gorkhover, Inger Andersson, Helmut Hirsemann, Guillaume Potdevin, Heinz Graafsma, Bjorn Nilsson, and John C. H. Spence. Femtosecond x-ray protein nanocrystallography. *Nature*, 470(7332):73–77, Feb 2011.

[54] Lars Redecke, Karol Nass, Daniel P. DePonte, Thomas A. White, Dirk Rehders, Anton Barty, Francesco Stellato, Mengning Liang, Thomas R.M.

Barends, Sbastien Boutet, Garth J. Williams, Marc Messerschmidt, M. Marvin Seibert, Andrew Aquila, David Arnlund, Sasa Bajt, Torsten Barth, Michael J. Bogan, Carl Caleman, Tzu-Chiao Chao, R. Bruce Doak, Holger Fleckenstein, Matthias Frank, Raimund Fromme, Lorenzo Galli, Ingo Grotjohann, Mark S. Hunter, Linda C. Johansson, Stephan Kassemeyer, Gergely Katona, Richard A. Kirian, Rudolf Koopmann, Chris Kupitz, Lukas Lomb, Andrew V. Martin, Stefan Mogk, Richard Neutze, Robert L. Shoeman, Jan Steinbrener, Nicusor Timneanu, Dingjie Wang, Uwe Weierstall, Nadia A. Zatsepin, John C. H. Spence, Petra Fromme, Ilme Schlichting, Michael Duszenko, Christian Betzel, and Henry N. Chapman. Natively inhibited trypanosoma brucei cathepsin b structure determined by using an x-ray laser. *Science*, 339(6116):227–230, 2013.

[55] AllariaE., AppioR., BadanoL., BarlettaW.A., BassaneseS., BiedronS.G., BorgaA., BusettoE., CastronovoD., CinquegranaP., ClevaS., CoccoD., CornacchiaM., CraievichP., CudinI., D'AuriaG., M. Dal Forno, DanailovM.B., R. De Monte, G. De Ninno, DelgiustoP., DemidovichA., S. Di Mitri, DiviaccoB., FabrisA., FabrisR., FawleyW., FerianisM., FerrariE., FerryS., FroehlichL., FurlanP., GaioG., GelmettiF., GiannessiL., GianniniM., GobessiR., IvanovR., KarantzoulisE., LonzaM., LutmanA., MahieuB., MillochM., MiltonS.V., MusardoM., NikolovI., NoeS., ParmigianiF., PencoG., PetronioM., PivettaL., PredonzaniM., RossiF., RumizL., SalomA., ScafuriC., SerpicoC., SigalottiP., SpampinatiS., SpezzaniC., SvandrlikM., SvetinaC., TazzariS., TrovoM., UmerR., VascottoA., VeroneseM., VisintiniR., ZaccariaM., ZangrandoD., and ZangrandoM. Highly coherent and stable pulses from the fermi seeded free-electron laser in the extreme ultraviolet. *Nat Photon*, 6(10):699–704, Oct 2012.

[56] David Pile. X-rays: First light from sacla. *Nat Photon*, 5(8):456–457, Aug 2011.

[57] F. Calegari, D. Ayuso, A. Trabattoni, L. Belshaw, S. De Camillis, S. Anumula, F. Frassetto, L. Poletto, A. Palacios, P. Decleva, J. B. Greenwood, F. Martn, and M. Nisoli. Ultrafast electron dynamics in phenylalanine initiated by attosecond pulses. *Science*, 346(6207):336–339, 2014.

[58] Alexander I. Kuleff, Jrg Breidbach, and Lorenz S. Cederbaum. Multielectron wave-packet propagation: General theory and application. *The Journal of Chemical Physics*, 123(4):–, 2005.

[59] Alexander I. Kuleff and Lorenz S. Cederbaum. Charge migration in different conformers of glycine: The role of nuclear geometry. *Chemical Physics*, 338(23):320 – 328, 2007. Molecular Wave Packet Dynamics(in honour of Jrn Manz).

[60] F. Calegari, D. Ayuso, A. Trabattoni, L. Belshaw, S. De Camillis, F. Frassetto, L. Poletto, A. Palacios, P. Decleva, J.B. Greenwood, F. Martin, and M. Nisoli. Ultrafast charge dynamics in an amino acid induced by

attosecond pulses. *Selected Topics in Quantum Electronics, IEEE Journal of*, 21(5):1–12, Sept 2015.

[61] Bridgette Cooper, Premysl Kolorenc, Leszek J. Frasinski, Vitali Averbukh, and Jon P. Marangos. Analysis of a measurement scheme for ultrafast hole dynamics by few femtosecond resolution x-ray pump-probe auger spectroscopy. *Faraday Discuss.*, 171:93–111, 2014.

[62] B. Mignolet, R. D. Levine, and F. Remacle. Charge migration in the bifunctional PENNA cation induced and probed by ultrafast ionization: a dynamical study. *J. Phys. B*, 47(12):124011, June 2014.

[63] Nikolay V. Golubev and Alexander I. Kuleff. Control of charge migration in molecules by ultrashort laser pulses. *Phys. Rev. A*, 91:051401, May 2015.

[64] A. Marciniak, V. Despre, T. Barillot, A. Rouzee, M. C. E. Galbraith, J. Klei, C.-H. Yang, C. T. L. Smeenk, V. Loriot, S. Nagaprasad Reddy, A. G. G. M. Tielens, S. Mahapatra, A. I. Kuleff, M. J. J. Vrakking, and F. Lepine. Xuv excitation followed by ultrafast non-adiabatic relaxation in pah molecules as a femto-astrochemistry experiment. *Nat Commun*, 6, Aug 2015. Article.

[65] David Mendive-Tapia, Morgane Vacher, Michael J. Bearpark, and Michael A. Robb. Coupled electron-nuclear dynamics: Charge migration and charge transfer initiated near a conical intersection. *The Journal of Chemical Physics*, 139(4):–, 2013.

[66] Morgane Vacher, Michael J. Bearpark, and Michael A. Robb. Communication: Oscillating charge migration between lone pairs persists without significant interaction with nuclear motion in the glycine and gly-gly-nhch3 radical cations. *The Journal of Chemical Physics*, 140(20):–, 2014.

[67] V. Despré, a. Marciniak, V. Loriot, M. C. E. Galbraith, a. Rouzée, M. J. J. Vrakking, F. Lépine, and Alexander I. Kuleff. Attosecond Hole Migration in Benzene Molecules Surviving Nuclear Motion. *The Journal of Physical Chemistry Letters*, 6(3):426–431, February 2015.

[68] Christoph Meier and Volker Engel. Interference structure in the photoelectron spectra obtained from multiphoton ionization of na_2 with a strong femtosecond laser pulse. *Phys. Rev. Lett.*, 73:3207–3210, Dec 1994.

[69] Zhigang Sun and Nanquan Lou. Autler-townes splitting in the multiphoton resonance ionization spectrum of molecules produced by ultrashort laser pulses. *Phys. Rev. Lett.*, 91:023002, Jul 2003.

[70] J. Caillat, J. Zanghellini, M. Kitzler, O. Koch, W. Kreuzer, and A. Scrinzi. Correlated multielectron systems in strong laser fields: A multiconfiguration time-dependent hartree-fock approach. *Phys. Rev. A*, 71:012712, Jan 2005.

[71] Tsuyoshi Kato and Hirohiko Kono. Time-dependent multiconfiguration theory for electronic dynamics of molecules in intense laser fields: A description in terms of numerical orbital functions. *The Journal of Chemical Physics*, 128(18):–, 2008.

[72] Tsuyoshi Kato and Kaoru Yamanouchi. Time-dependent multiconfiguration theory for describing molecular dynamics in diatomic-like molecules. *The Journal of Chemical Physics*, 131(16), 2009.

[73] Ofir E. Alon, Alexej I. Streltsov, and Lorenz S. Cederbaum. Many-body theory for systems with particle conversion: Extending the multiconfigurational time-dependent hartree method. *Phys. Rev. A*, 79:022503, Feb 2009.

[74] M. Nest. The multi-configuration electronnuclear dynamics method. *Chemical Physics Letters*, 472(46):171 – 174, 2009.

[75] D. J. Haxton, K. V. Lawler, and C. W. McCurdy. Multiconfiguration time-dependent hartree-fock treatment of electronic and nuclear dynamics in diatomic molecules. *Phys. Rev. A*, 83:063416, Jun 2011.

[76] D. J. Haxton and C. W. McCurdy. Ultrafast population transfer to excited valence levels of a molecule driven by x-ray pulses. *Phys. Rev. A*, 90:053426, Nov 2014.

[77] Daniel J. Haxton and C. William McCurdy. Two methods for restricted configuration spaces within the multiconfiguration time-dependent hartree-fock method. *Phys. Rev. A*, 91:012509, Jan 2015.

[78] S. E. Canton, E. Plésiat, J. D. Bozek, B. S. Rude, P. Decleva, and F. Martín. Direct observation of cohen-fano interferences in vibrationally resolved valence-shell photoionization spectra of h¡sub¿2¡/sub¿, n¡sub¿2¡/sub¿ and co. *Proceedings of the National Academy of Sciences*, 108:7302–7306, 2011.

[79] E. Plésiat, L. Argenti, E. Kukk, C. Miron, K. Ueda, P. Decleva, and F. Martín. Intramolecular electron diffraction in vibrationally resolved k-shell photoionization of methane. *Phys. Rev. A*, 85:023409–1 – 023409–7, 2012.

[80] E. Plésiat, P. Decleva, and F. Martín. Vibrational branching ratios in the photoelectron spectra of n¡sub¿2¡/sub¿ and co: interference and diffraction effects. *Physical Chemistry Chemical Physics*, 14:10853–10871, 2012.

[81] E. Plésiat, P. Decleva, and F. Martín. Vibrationally-resolved photoelectron angular distributions from randomly-oriented and fixed-in-space n¡sub¿2¡/sub¿ and co molecules. *Journal of Physics B*, 45:194008–1 – 194008–10, 2012.

[82] E. Kukk, D. Ayuso, T. D. Thomas, P. Decleva, M. Patanen, L. Argenti, E. Plèsiat, A. Palacios, K. Kooser, O. Travnikova, S. Mondal, M. Kimura, K. Sakai, C. Miron, F. Martín, and K. Ueda. Effects of molecular potential and geometry on atomic core-level photoemission over an extended energy range: The case study of the co molecule. *Physical Review A*, 88:033412, 2013.

[83] L. Argenti, T. D. Thomas, E. Plésiat, X. J. Liu, C. Miron, T. Lischke, G Prmper, K. Sakai, T. Ouchi, R. Pttner, V. Sekushin, T. Tanaka, M. Hoshino, H. Tanaka, P. Decleva, K. Ueda, and F. Martín. Double-slit experiment with a polyatomic molecule: vibrationally-resolved c 1s photoelectron spectra of acetylene. *New Journal of Physics*, 14:033012–1 – 033012–18, 2012.

[84] K. Ueda, C. Miron, E. Plésiat, L. Argenti, M. Patanen, K. Kooser, D. Ayuso, S. Mondal, M. Kimura, K. Sakai, O. Travnikova, A. Palacios, P. Decleva, E. Kukk, and F. Martín. Intramolecular photoelectron diffraction in the gas phase. *Journal of Chemical Physics*, 139:124306, 2013.

[85] E. Plésiat, P. Decleva, and F. Martín. Vibrationally resolved k-shell photoionization cross sections of methane. *Central European Journal of Physics*, 11:1157, 2013.

[86] M. Patanen, K. Kooser, L. Argenti, D. Ayuso, M. Kimura, S. Mondal, E. Plésiat, A. Palacios, K. Sakai, O. Travnikova, P. Decleva, E. Kukk, C. Miron, K. Ueda, and F. Martín. Vibrationally resolved c 1s photoionization cross section of cf¡sub¿4¡/sub¿. *Journal of Physics B*, 47:124032, 2014.

[87] D. Ayuso, A. Palacios, P. Decleva, and F. Martín. Dissociative and non-dissociative photoionization of molecular fluorine from inner and valence shells. *Journal of Electron Spectroscopy and Related Phenomena*, 195:320 – 326, 2014.

[88] D. Ayuso, M. Kimura, K. Kooser, M. Patanen, E. Plsiat, L. Argenti, S. Mondal, O. Travnikova, K. Sakai, A. Palacios, E. Kukk, P. Decleva, K. Ueda, F. Martn, and C. Miron. Vibrationally resolved b 1s photoionization cross section of bf3. *The Journal of Physical Chemistry A*, 119(23):5971–5978, 2015. PMID: 25761399.

[89] B. Diu C. Cohen-Tannoudji and F. Laloë. *Quantum mechanics*. Quantum Mechanics. Wiley, 1977.

[90] R. M. Potvliege C. J. Joachain, N. J. Kylstra. *Atoms in Intense Laser Fields*. Cambridge University Press, 2012.

[91] ANDR D. BANDRAUK and HUIZHONG LU. Exponential propagators (integrators) for the time-dependent schrdinger equation. *Journal of Theoretical and Computational Chemistry*, 12(06):1340001, 2013.

[92] John Robert Taylor. *Scattering theory: the quantum theory on nonrelativistic collisions*. Wiley, 1972.

[93] A. Szabó and N. S. Ostlund. *Modern Quantum Chemistry: Introduction to Advanced Electronic Structure Theory*. Dover Books on Chemistry Series. Dover Publications, Incorporated, 1996.

[94] M. Born and R. Oppenheimer. Zur quantentheorie der molekeln. *Annalen der Physik*, 389(20):457–484, 1927.

[95] Robert R. Lucchese and Vincent McKoy. Studies of differential and total photoionization cross sections of carbon dioxide. *Phys. Rev. A*, 26:1406–1418, Sep 1982.

[96] Theoretical study of the excited and continuum states in the nexafs region of cl_2. *Phys. Chem. Chem. Phys.*, 1:1405, 1999.

[97] M. Stener and P. Decleva. Time-dependent density functional calculations of molecular photoionization cross sections: N_2 and ph_3. *The Journal of Chemical Physics*, 112(24):10871–10879, 2000.

[98] Alexander I. Kuleff and Lorenz S. Cederbaum. Ultrafast correlation-driven electron dynamics. *Journal of Physics B: Atomic, Molecular and Optical Physics*, 47(12):124002, June 2014.

[99] I. N. Levine. *Quantum Chemistry*. Pearson Education, Limited, 2013.

[100] Reiner M. Dreizler and Eberhard K. U. Gross. *Density Functional Theory. An Approach to the Quantum Many-Body Problem*. Springer-Verlag, 1990.

[101] C. J. Cramer. *Essentials of Computational Chemistry: Theories and Models*. Wiley, 2002.

[102] P. Hohenberg and W. Kohn. Inhomogeneous electron gas. *Phys. Rev.*, 136:B864–B871, Nov 1964.

[103] W. Kohn and L. J. Sham. Self-consistent equations including exchange and correlation effects. *Phys. Rev.*, 140:A1133–A1138, Nov 1965.

[104] M. Stener, A. Lisini, and P. Decleva. Accurate local density photoionization cross sections by lcao stieltjes imaging approach. *International Journal of Quantum Chemistry*, 53(2):229–244, 1995.

[105] M. Stener, G. De Alti, and P. Decleva. Convergence of the density functional one-centre expansion for the molecular continuum: N 2 and $(ch_3)_3n$. *Theor. Chem. Acc.*, 101:247–256, 1999.

[106] M Stener, S Furlan, and P Decleva. Density functional calculations of photoionization with an exchange-correlation potential with the correct asymptotic behaviour. *Journal of Physics B: Atomic, Molecular and Optical Physics*, 33(5):1081, 2000.

[107] P. Decleva J. E. Hansen H. Bachau, E. Cormier and F Martín. Applications of b-splines in atomic and molecular physics. *Reports on Progress in Physics*, 64(12):1815, 2001.

[108] G. Fronzoni D. Toffoli, M. Stener and P. Decleva. Convergence of the multicenter b-spline {DFT} approach for the continuum. *Chemical Physics*, 276(1):25 – 43, 2002.

[109] G. Fronzoni M. Stener, D. Toffoli and P. Decleva. Time dependent density functional study of the photoionization dynamics of sf_6]. *The Journal of Chemical Physics*, 124(11):114306, 2006.

[110] D. Toffoli, M. Stener, G. Fronzoni, and P. Decleva. Photoionization cross section and angular distribution calculations of carbon tetrafluoride. *The Journal of Chemical Physics*, 124(21):–, 2006.

[111] S. Korica, A. Reinkster, M. Braune, J. Viefhaus, D. Rolles, B. Langer, G. Fronzoni, D. Toffoli, M. Stener, P. Decleva, O.M. Al-Dossary, and U. Becker. Partial photoionization cross sections of {C60} and c70: A gas versus adsorbed phase comparison. *Surface Science*, 604(2122):1940 – 1944, 2010.

[112] Thomas X. Carroll, Maria G. Zahl, Knut J. Brve, Leif J. Sthre, Piero Decleva, Aurora Ponzi, Joshua J. Kas, Fernando D. Vila, John J. Rehr, and T. Darrah Thomas. Intensity oscillations in the carbon 1s ionization cross sections of 2-butyne. *The Journal of Chemical Physics*, 138(23):–, 2013.

[113] Rajesh Kumar Kushawaha, Minna Patanen, Renaud Guillemin, Loic Journel, Catalin Miron, Marc Simon, Maria Novella Piancastelli, C. Skates, and Piero Decleva. From double-slit interference to structural information in simple hydrocarbons. *Proceedings of the National Academy of Sciences*, 110(38):15201–15206, 2013.

[114] P G Burke, N Chandra, and F A Gianturco. Electron-molecule interactions. iv. scattering by polyatomic molecules. *Journal of Physics B: Atomic and Molecular Physics*, 5(12):2212, 1972.

[115] Tosio Kato. On the eigenfunctions of many-particle systems in quantum mechanics. *Communications on Pure and Applied Mathematics*, 10(2):151–177, 1957.

[116] C. Fonseca Guerra, J. G. Snijders, G. te Velde, and E. J. Baerends. Towards an order-n dft method. *Theoretical Chemistry Accounts*, 99(6):391–403, 1998.

[117] G. te Velde, F. M. Bickelhaupt, E. J. Baerends, C. Fonseca Guerra, S. J. A. van Gisbergen, J. G. Snijders, and T. Ziegler. Chemistry with adf. *Journal of Computational Chemistry*, 22(9):931–967, 2001.

[118] Theoretical Chemistry. Vrije Universiteit. Amsterdam. The Netherlands. Adf2013 scm.

[119] S. H. Vosko, L. Wilk, and M. Nusair. Accurate spin-dependent electron liquid correlation energies for local spin density calculations: a critical analysis. *Canadian Journal of Physics*, 58(8):1200–1211, 1980.

[120] R. van Leeuwen and E. J. Baerends. Exchange-correlation potential with correct asymptotic behavior. *Phys. Rev. A*, 49:2421–2431, Apr 1994.

[121] A. Zangwill and P. Soven. Density-functional approach to local-field effects in finite systems: Photoabsorption in the rare gases. *Phys. Rev. A*, 21:1561–1572, May 1980.

[122] G. D. Mahan. Modified sternheimer equation for polarizability. *Phys. Rev. A*, 22:1780–1785, Nov 1980.

[123] Anonymous. Minutes of the stanford meeting, march 6, 1926. *Phys. Rev.*, 27:637–644, May 1926.

[124] J. Franck and E. G. Dymond. Elementary processes of photochemical reactions. *Trans. Faraday Soc.*, 21:536–542, 1926.

[125] Edward Condon. A theory of intensity distribution in band systems. *Phys. Rev.*, 28:1182–1201, Dec 1926.

[126] Edward U. Condon. Nuclear motions associated with electron transitions in diatomic molecules. *Phys. Rev.*, 32:858–872, Dec 1928.

[127] H. Fukuzawa G. Prumper K. Ueda E. Kukk R. Sankari J. Harries Y. Tamenori T. Tanaka M. Hoshino T. Darrah Thomas, R. Puttner and H. Tanaka. Boron 1s photoelectron spectrum of $^{11}bf_3$: Vibrational structure and linewidth. *The Journal of Chemical Physics*, 127(24):244309, 2007.

[128] R. Sankari H. Fukuzawa G. Prumper K. Ueda R. Puttner J. Harries Y. Tamenori T. Tanaka M. Hoshino T. D. Thomas, E. Kukk and H. Tanaka. Recoil excitation of vibrational structure in the carbon 1s photoelectron spectrum of cf[sub 4]. *The Journal of Chemical Physics*, 128(14):144311, 2008.

[129] Philip M. Morse. Diatomic molecules according to the wave mechanics. ii. vibrational levels. *Phys. Rev.*, 34:57–64, Jul 1929.

[130] Dale E. Sayers, Edward A. Stern, and Farrel W. Lytle. New technique for investigating noncrystalline structures: Fourier analysis of the extended x-ray¯absorption fine structure. *Phys. Rev. Lett.*, 27:1204–1207, Nov 1971.

[131] S. Pascarelli M. D. Cooke F. R. Pettifer, O. Mathon and M. R. M. Gibbs. Measurement of femtometre-scale atomic displacements by x-ray absorption spectroscopy. *Nature*, 435:78–81, 2005.

[132] Scott A. Chambers. Epitaxial film crystallography by high-energy auger and x-ray photoelectron diffraction. *Advances in Physics*, 40(4):357–415, 1991.

[133] Ph Hofmann, K.-M. Schindler, S. Bao, A. M. Bradshaw, and D. P. Woodruff. Direct identification of atomic and molecular adsorption sites using photoelectron diffraction. *Nature*, 368(6467):131–132, Mar 1994.

[134] Christian Bressler, , and Majed Chergui*. Ultrafast x-ray absorption spectroscopy. *Chemical Reviews*, 104(4):1781–1812, 2004. PMID: 15080712.

[135] Pieter Glatzel and Uwe Bergmann. High resolution 1s core hole x-ray spectroscopy in 3d transition metal complexeselectronic and structural information. *Coordination Chemistry Reviews*, 249(12):65 – 95, 2005. Synchrotron Radiation in Inorganic and Bioinorganic Chemistry.

[136] D.P. Woodruff. Adsorbate structure determination using photoelectron diffraction: Methods and applications. *Surface Science Reports*, 62(1):1 – 38, 2007.

[137] Alessandro Arcovito, Maurizio Benfatto, Michele Cianci, S. Samar Hasnain, Karin Nienhaus, G. Ulrich Nienhaus, Carmelinda Savino, Richard W. Strange, Beatrice Vallone, and Stefano Della Longa. X-ray structure analysis of a metalloprotein with enhanced active-site resolution using in situ x-ray absorption near edge structure spectroscopy. *Proceedings of the National Academy of Sciences*, 104(15):6211–6216, 2007.

[138] Michael Haumann, Alexander Grundmeier, Ivelina Zaharieva, and Holger Dau. Photosynthetic water oxidation at elevated dioxygen partial pressure monitored by time-resolved x-ray absorption measurements. *Proceedings of the National Academy of Sciences*, 105(45):17384–17389, 2008.

[139] N. Pangher, H. M. Köppe, J. Feldhaus, and J. Haase. Determination of intramolecular bond lengths of low- Z molecules in the gas phase, condensed, and chemisorbed states using extended x-ray absorption fine structure. *Phys. Rev. Lett.*, 71:4365–4368, Dec 1993.

[140] Rok Prešeren, Alojz Kodre, Iztok Arčon, and Michael Borowski. Atomic background and exafs of gaseous hydrides of ge, as, se and br. *Journal of Synchrotron Radiation*, 8(2):279–281, Mar 2001.

[141] J. Söderström, N. Mårtensson, O. Travnikova, M. Patanen, C. Miron, L. J. Sæthre, K. J. Børve, J. J. Rehr, J. J. Kas, F. D. Vila, T. D. Thomas, and S. Svensson. Nonstoichiometric intensities in core photoelectron spectroscopy. *Phys. Rev. Lett.*, 108:193005, May 2012.

[142] F. Krasniqi, B. Najjari, L. Strüder, D. Rolles, A. Voitkiv, and J. Ullrich. Imaging molecules from within: Ultrafast angström-scale structure determination of molecules via photoelectron holography using free-electron lasers. *Phys. Rev. A*, 81:033411, Mar 2010.

[143] H. Fukuzawa, X.-J. Liu, T. Teranishi, K. Sakai, G. Prmper, K. Ueda, Y. Morishita, N. Saito, M. Stener, and P. Decleva. Fluorine k-shell photoelectron angular distribution from {CF4} molecules in the molecular frame. *Chemical Physics Letters*, 451(46):182 – 185, 2008.

[144] Jun ichi Adachi, Misato Kazama, Takahiro Teramoto, Naoya Miyauchi, Tomoya Mizuno, Masakazu Yamazaki, Takashi Fujikawa, and Akira Yagishita. C 1s photoelectron angular distributions from fixed-in-space co molecules in the high-energy continuum 50ev. *Journal of Physics B: Atomic, Molecular and Optical Physics*, 45(19):194007, 2012.

[145] J. B. Williams, C. S. Trevisan, M. S. Schöffler, T. Jahnke, I. Bocharova, H. Kim, B. Ulrich, R. Wallauer, F. Sturm, T. N. Rescigno, A. Belkacem, R. Dörner, Th. Weber, C. W. McCurdy, and A. L. Landers. Imaging polyatomic molecules in three dimensions using molecular frame photoelectron angular distributions. *Phys. Rev. Lett.*, 108:233002, Jun 2012.

[146] J B Williams, C S Trevisan, M S Schffler, T Jahnke, I Bocharova, H Kim, B Ulrich, R Wallauer, F Sturm, T N Rescigno, A Belkacem, R Drner, Th Weber, C W McCurdy, and A L Landers. Probing the dynamics of dissociation of methane following core ionization using three-dimensional molecular-frame photoelectron angular distributions. *Journal of Physics B: Atomic, Molecular and Optical Physics*, 45(19):194003, 2012.

[147] X-J Liu, N A Cherepkov, S K Semenov, V Kimberg, F Gel'mukhanov, G Prmper, T Lischke, T Tanaka, M Hoshino, H Tanaka, and K Ueda. Young's double-slit experiment using core-level photoemission from n 2 : revisiting cohenfano's two-centre interference phenomenon. *Journal of Physics B: Atomic, Molecular and Optical Physics*, 39(23):4801, 2006.

[148] C. Miron. Soleil pléiades beamline. .

[149] B Kempgens, K Maier, A Kivim?ki, H M K?ppe, M Neeb, M N Piancastelli, U Hergenhahn, and A M Bradshaw. Vibrational excitation in c 1s and o 1s photoionization of co. *Journal of Physics B: Atomic, Molecular and Optical Physics*, 30(21):L741, 1997.

[150] J. L. Dehmer and D. Dill. Shape resonances in k-shell photoionization of diatomic molecules. *Phys. Rev. Lett.*, 35:213–215, Jul 1975.

[151] M.N Piancastelli. The neverending story of shape resonances. *Journal of Electron Spectroscopy and Related Phenomena*, 100(13):167 – 190, 1999.

[152] Y. Shimizu, K. Ueda, H. Chiba, K. Ohmori, M. Okunishi, Y. Sato, and T. Hayaishi. Angle-resolved photoelectron and photoion study on the shape resonance in the b 1s ionization region of bf3. *J. Chem. Phys.*, 107(7):2415–2418, 1997.

[153] Edward A. Stern. Theory of the extended x-ray-absorption fine structure. *Phys. Rev. B*, 10:3027–3037, Oct 1974.

[154] H. D. Cohen and U. Fano. Interference in the photo-ionization of molecules. *Phys. Rev.*, 150:30–33, Oct 1966.

[155] S K Semenov, N A Cherepkov, M Matsumoto, K Fujiwara, K Ueda, E Kukk, F Tahara, T Sunami, H Yoshida, T Tanaka, K Nakagawa, M Kitajima, H Tanaka, and A De Fanis. Vibrationally resolved photoionization of the 1? g and 1? u shells of n 2 molecule. *Journal of Physics B: Atomic, Molecular and Optical Physics*, 39(2):375, 2006.

[156] M. Ehara, K. Kuramoto, H. Nakatsuji, M. Hoshino, T. Tanaka, M. Kitajima, H. Tanaka, A. De Fanis, Y. Tamenori, and K. Ueda. C1s and o1s photoelectron satellite spectra of co with symmetry-dependent vibrational excitations. *The Journal of Chemical Physics*, 125(11):–, 2006.

[157] J. Fernández, O. Fojón, A. Palacios, and F. Martín. Interferences from fast electron emission in molecular photoionization. *Phys. Rev. Lett.*, 98:043005, Jan 2007.

[158] Stephan Eberhard, Giovanni Finazzi, and Francis-Andr Wollman. The dynamics of photosynthesis. *Annual Review of Genetics*, 42(1):463–515, 2008. PMID: 18983262.

[159] Meike Cordes and Bernd Giese. Electron transfer in peptides and proteins. *Chem. Soc. Rev.*, 38:892–901, 2009.

[160] David Becker, Amitava Adhikary, and MichaelD. Sevilla. The role of charge and spin migration in dna radiation damage. In Tapash Chakraborty, editor, *Charge Migration in DNA*, NanoScience and Technology, pages 139–175. Springer Berlin Heidelberg, 2007.

[161] R. Weinkauf, P. Aicher, G. Wesley, J. Grotemeyer, and E. W. Schlag. Femtosecond versus nanosecond multiphoton ionization and dissociation of large molecules. *The Journal of Physical Chemistry*, 98(34):8381–8391, 1994.

[162] L. Lehr, T. Horneff, R. Weinkauf, , and E. W. Schlag. Femtosecond dynamics after ionization: 2-phenylethyl-n,n-dimethylamine as a model system for nonresonant downhill charge transfer in peptides. *The Journal of Physical Chemistry A*, 109(36):8074–8080, 2005. PMID: 16834192.

[163] Chengteh Lee, Weitao Yang, and Robert G. Parr. Development of the colle-salvetti correlation-energy formula into a functional of the electron density. *Phys. Rev. B*, 37:785–789, Jan 1988.

[164] Axel D. Becke. Densityfunctional thermochemistry. iii. the role of exact exchange. *The Journal of Chemical Physics*, 98(7), 1993.

[165] M. J. Frisch, G. W. Trucks, H. B. Schlegel, G. E. Scuseria, M. A. Robb, J. R. Cheeseman, G. Scalmani, V. Barone, B. Mennucci, G. A. Petersson, H. Nakatsuji, M. Caricato, X. Li, H. P. Hratchian, A. F. Izmaylov,

J. Bloino, G. Zheng, J. L. Sonnenberg, M. Hada, M. Ehara, K. Toyota, R. Fukuda, J. Hasegawa, M. Ishida, T. Nakajima, Y. Honda, O. Kitao, H. Nakai, T. Vreven, J. A. Montgomery, Jr., J. E. Peralta, F. Ogliaro, M. Bearpark, J. J. Heyd, E. Brothers, K. N. Kudin, V. N. Staroverov, R. Kobayashi, J. Normand, K. Raghavachari, A. Rendell, J. C. Burant, S. S. Iyengar, J. Tomasi, M. Cossi, N. Rega, J. M. Millam, M. Klene, J. E. Knox, J. B. Cross, V. Bakken, C. Adamo, J. Jaramillo, R. Gomperts, R. E. Stratmann, O. Yazyev, A. J. Austin, R. Cammi, C. Pomelli, J. W. Ochterski, R. L. Martin, K. Morokuma, V. G. Zakrzewski, G. A. Voth, P. Salvador, J. J. Dannenberg, S. Dapprich, A. D. Daniels, . Farkas, J. B. Foresman, J. V. Ortiz, J. Cioslowski, and D. J. Fox. Gaussian09 Revision D.01. Gaussian Inc. Wallingford CT 2009.

[166] Siegfried Lnnemann, Alexander I. Kuleff, and Lorenz S. Cederbaum. Ultrafast charge migration in 2-phenylethyl-n,n-dimethylamine. *Chemical Physics Letters*, 450(46):232 – 235, 2008.

[167] Attila G. Csaszar. Conformers of gaseous glycine. *Journal of the American Chemical Society*, 114(24):9568–9575, 1992.

[168] Zhijian Huang, Wenbo Yu, and Zijing Lin. Exploration of the full conformational landscapes of gaseous aromatic amino acid phenylalanine: An ab initio study. *Journal of Molecular Structure: {THEOCHEM}*, 758(23):195 – 202, 2006.

[169] L. C. Snoek, R. T. Kroemer, M. R. Hockridge, and J. P. Simons. Conformational landscapes of aromatic amino acids in the gas phase: Infrared and ultraviolet ion dip spectroscopy of tryptophan. *Phys. Chem. Chem. Phys.*, 3:1819–1826, 2001.

[170] W. von Niessen, J. Schirmer, and L.S. Cederbaum. Computational methods for the one-particle green's function. *Computer Physics Reports*, 1(2):57 – 125, 1984.

[171] John C. Slater. Statistical exchange-correlation in the self-consistent field. volume 6 of *Advances in Quantum Chemistry*, pages 1 – 92. Academic Press, 1972.

[172] Oksana Plekan, Vitaliy Feyer, Robert Richter, Marcello Coreno, and Kevin C. Prince. Valence photoionization and photofragmentation of aromatic amino acids. *Molecular Physics*, 106(9-10):1143–1153, 2008.

[173] Sherrie Campbell, Elaine M. Marzluff, M. T. Rodgers, J. L. Beauchamp, Margaret E. Rempe, Kimberly F. Schwinck, and D. L. Lichtenberger. Proton affinities and photoelectron spectra of phenylalanine and n-methyl- and n,n-dimethylphenylalanine. correlation of lone pair ionization energies with proton affinities and implications for n-methylation as a method to effect site specific protonation of peptides. *Journal of the American Chemical Society*, 116(12):5257–5264, 1994.

[174] P.H. Cannington and Norman S. Ham. He(i) and he(ii) photoelectron spectra of glycine and related molecules. *Journal of Electron Spectroscopy and Related Phenomena*, 32(2):139 – 151, 1983.

[175] John J. Neville, Y. Zheng, , and C. E. Brion*. Glycine valence orbital electron densities: comparison of electron momentum spectroscopy experiments with hartreefock and density functional theories. *Journal of the American Chemical Society*, 118(43):10533–10544, 1996.